UNIVERSITÉ DE NANTES

FACULTÉ DES SCIENCES ET DES TECHNIQUES

ECOLE DOCTORALE 3MPL

MOLÉCULES, MATIÊRES ET MATÉRIAUX EN PAYS DE LOIRE

Année2013

Open Charm in heavy ion and p+p collisions with STAR at RHIC

THÈSE DE DOCTORAT
Discipline : Physique
Spécialité : Physique Subatomique

Présentée
et soutenue publiquement par

Witold BOROWSKI

Le 11 octobre 2013, devant le jury ci-dessous

Président	Pol-Bernard GOSSIAUX, A, SUBATECH (Nantes)
Rapporteurs	Christian KUHN, A, IRES (Strasbourg)
	Spyridon MARGETIS, A, Kent State University (Ohio)
Examinateurs	Jaroslav BIELČÍK, B, ČVUT (Prague)
	Magali ESTIENNE, B, SUBATECH (Nantes)

Directeur de thèse : Sonia KABANA, Universite de Nantes

Abstract: Heavy quarks, namely c and b, at the RHIC energy scale are produced mainly in the early stages of the collision. Thus they are expected to be a good probe to study the first moments of the system formation. However the analysis of the spectra of non-photonic electrons, that comes form c and b semi-leptonic decays, shows suppression of the nuclear modification factor for the large transverse momenta (p_T) similar to the one measured for the light flavor hadrons, which contradicts the theoretical prediction. To understand this phenomenon a separate measurement of the c and b contribution to those spectra had to be carried out. This has already been done for the proton-proton collisions at 200 GeV. For this study in the STAR experiment a special technique, the electron–D^0 azimuthal angular correlations has been developed.

This thesis shows that the capabilities of the current setup of the STAR detector do not allow to perform this kind of measurement in the Gold Gold collisions at 200 GeV. Furthermore it shows that the application of this method in proton-proton collision at 500 GeV results in a dominant production of the b in comparison with c quark for the energy of non-photonic electron from the heavy flavor decay greater than 4.3 GeV.

The inclusive spectra of the charm particles (D^0 and D*) has been measured by STAR in proton-proton minimum bias collisions in the range of pT up to 7 GeV/c. This thesis presents a new pioneering study on the D* measurement in High Tower dataset which allows to extend the spectra in pT up to 18 GeV/c in the proton-proton system at 500 GeV. That range of the pT for D* meson has never been reached before on any system measured in STAR.

Keywords: heavy flavor, charm and beauty separation, quark gluon plasma, heavy ion collisiosns

Résumé: Aux énergies du RHIC, les quarks lourds c et b sont produits principalement dans les premiers stades de la collision. Ainsi, ils sont censés être une bonne sonde pour étudier les premiers instants de la formation du système. L'analyse des spectres d'électrons non-photoniques, qui résultent de la désintégration semi-leptonique des quarks c et b, montre, dans le cas de collisions noyau-noyau une suppression par rapport au cas proton-proton aux grandes valeurs de l'impulsion transverse (p_T), similairement aux hadrons légers. Un tel comportement du facteur de modification nucléaire contredit la prédiction théorique. Pour comprendre ce phénomène une mesure séparée de la contribution des quarks c et b à ces spectres a dû être effectuée. Cela a déjà été fait pour les collisions proton-proton à 200 GeV. Pour cette étude dans l'expérience STAR une technique spéciale, les corrélations angulaires azimutales électron-D^0, a été développée.

Cette thèse montre que les capacités du détecteur STAR ne permettent pas d'effectuer ce type de mesure dans les collisions Or-Or à 200 GeV. En outre, il montre que l'application de cette méthode dans une collision proton-proton à 500 GeV se traduit par une production dominante du quark b par rapport au quark c, pour une énergie des électrons non-photoniques supérieure à 4,3 GeV.

Les spectres inclusifs des particules charmées (D^0 et D*) ont été mesurés par STAR dans les collisions proton-proton « minimum bias » pour pT allant jusqu'à 7 GeV/c. Cette thèse présente une étude pionnière sur la mesure D* dans le données « high tower » qui permet d'étendre le spectre en pT jusqu'à 18 GeV/c dans le système proton-proton à 500 GeV. Un tel pT dans le mesure de mésons D* n'a jamais été atteint auparavant, et ce quel que soit le système mesuré par STAR.
Mots-clés : quarks lourds, séparation de charme et de la beauté, plasma de quark et gluon, collisions de ion lourds

Contents

1 Introduction **1**
- 1.1 Preface . . . 1
- 1.2 Standard Model . . . 2
- 1.3 Quark-Gluon Plasma . . . 4
  - 1.3.1 Phase diagram of the strongly interacting matter . . . 4
  - 1.3.2 Evolution of the universe . . . 5
- 1.4 Heavy Ion Collisions . . . 6
  - 1.4.1 Evolution of heavy ion collision . . . 7

2 Heavy Flavor Quarks **9**
- 2.1 Parton Energy Loss and Heavy Flavor . . . 9
- 2.2 Beauty and Charm separation via e-h and e-D^0 angular correlations 11
- 2.3 Motivation of the Thesis . . . 16

3 Experiment **17**
- 3.1 Detector . . . 18
  - 3.1.1 Time Projection Chamber . . . 19
  - 3.1.2 Time of Flight . . . 19
  - 3.1.3 Electromagnetic Calorimeter . . . 19
- 3.2 Data reconstruction . . . 20

4 Data Analysis **21**
- 4.1 Data Preselection . . . 22
- 4.2 D meson reconstruction . . . 25
  - 4.2.1 Invariant Mass . . . 28
  - 4.2.2 Decay Geometry Study . . . 28
- 4.3 Electron identification . . . 35
  - 4.3.1 Matching to BEMC . . . 35
  - 4.3.2 Identification cuts . . . 36
  - 4.3.3 Electron purity . . . 39
  - 4.3.4 Non-photonic electron selection . . . 40
- 4.4 Angular correlations . . . 42

5 Results **45**
- 5.1 Gold-gold collisions at 200 GeV . . . 45
- 5.2 Proton-proton collisions at 500 GeV . . . 48
  - 5.2.1 Overall charm production in the high tower dataset . . . 48
  - 5.2.2 Measurement of high-p_T D* in the hadron-triggered events . . . 55
  - 5.2.3 Charm production in electron-triggered events . . . 68
  - 5.2.4 Electron-D azimuthal angular correlations . . . 70

6 Summary 73

Bibliography 75

Chapter 1

Introduction

Contents

1.1 **Preface** 1
1.2 **Standard Model** 2
1.3 **Quark-Gluon Plasma** 4
1.3.1 Phase diagram of the strongly interacting matter 4
1.3.2 Evolution of the universe 5
1.4 **Heavy Ion Collisions** 6
1.4.1 Evolution of heavy ion collision 7

1.1 Preface

Since the dawn of time people were trying to describe the surrounding world with the finite number of properties that can be called fundamental. In the ancient Greece it was believed that fundamental were four elements: Earth, Fire, Water and Air, which had emerged form the primordial Chaos. During the epoch of great discoveries it was already known that everything is build of objects called atoms, from Greek indivisible. In the middle of XIX century Russian chemist, Dmitri Mendeleev, systematized them in the periodic table based on their properties. Soon, thanks to the work of Marie Skłodowska-Curie and Henri Becquerel, it became obvious that atoms are not fundamental and the properties used by Mendeleev depends on the number of electrons in each of them. Then, in 1911, Ernest Rutherford has performed his famous experiment and discovered a dense, positively charged object in the center of atom - nucleus. Next, in 1919, he managed to prove that this positive charge is held by protons. Finally, in 1932, James Chadwick has completed the picture of atom by discovering neutron, the neutral component of nucleus. Reference for the general public would be [Clo83].

At that time it seemed that protons and neutrons (nucleons) doesn't have any inner structure. However soon the progress in analysis techniques allowed the discovery of many new particles with the properties similar to nucleons. This, in early 60's of the XX century, made Murray Gell-Mann and George Zweig to propose a hypothesis that all those particles are build from another type of matter, aces/quarks [Hal08]. The existence of the inner structure of proton was then confirmed in experiment at the Stanford Linear Accelerator Center in 1969 [Per00]. Nowadays quarks are considered to be elementary particles.

Along with the studies on the structure of matter people were trying to describe the forces that causes interactions between them. Today four such interactions are being considered as fundamental: gravity, electromagnetism, weak force and strong force. The first two were known to the humanity since ancient times. However they received the scientific definition much later. Gravity was described as and attraction between objects by Isaac Newton in 1687 and electromagnetism as an interaction between electric charges or magnetic poles by James Maxwell in 1873. Two other forces are short distance interactions. Thus they remained undiscovered until the studies on the properties of nucleus began. Weak force was first proposed to explain the nuclear β decay (emission of electron and neutrino form the nucleus). Electromagnetic and week interactions are nowadays parts of the electro-weak theory, which was presented in 1968 by Sheldon Glashow, Abdus Salam and Steven Weinberg. Strong interaction was postulated as a Yukawa potential in order to describe the binding force which holds together nucleons inside the nucleus. Later, the discovery of the proton's inner structure, has redefined it as an interaction between quarks. Today it's nature is still not well understood and remains a field of intensive studies, for example the origin of the spin of the proton which remains subject of intensive study [Ada13b, Ada13a].

This work treats of the strong interactions with a focus on the production mechanisms of the charm quark. The thesis is divided into four chapters, the first of them provides a brief introduction into the science of elementary particles, and its main goals. Second chapter describes the current state of knowledge concerning heavy flavor quarks and depicts the main direction of the research which is a motivation for this study. Chapter three is a description of the experiment performed to collect the scientific data. The fourth one shows the analysis techniques used on the data. Last chapter presents the obtained results along with the conclusion that arises from them as well as elaborates on future of this research.

1.2 Standard Model

The theory that summarizes current knowledge on the structure of the universe is called the Standard Model. It distinguishes three groups of particles, which are considered to be elementary: quarks, leptons and force carriers (fig. 1.1). The first two types are fermions, as they have half-odd integer spin values, the third - bosons, with the integer spin. Recently this set has been supplemented with a newly discovered Higgs boson [Ady13, Whi13].

Quarks and leptons form three generations. Each of them contains two quarks, one with positive charge (+2/3 of unitary charge) and one with negative (-1/3), and two leptons, nearly massless and neutral, neutrino, and a heavier particle with a negative unitary charge. In addition to electric charge, quarks are described by another quantum number - the color, which takes one of the three possible value, usually referred to as red, green, and blue. In the current state of the universe only the members of the first generation and the neutrinos can exist in the stable form, all

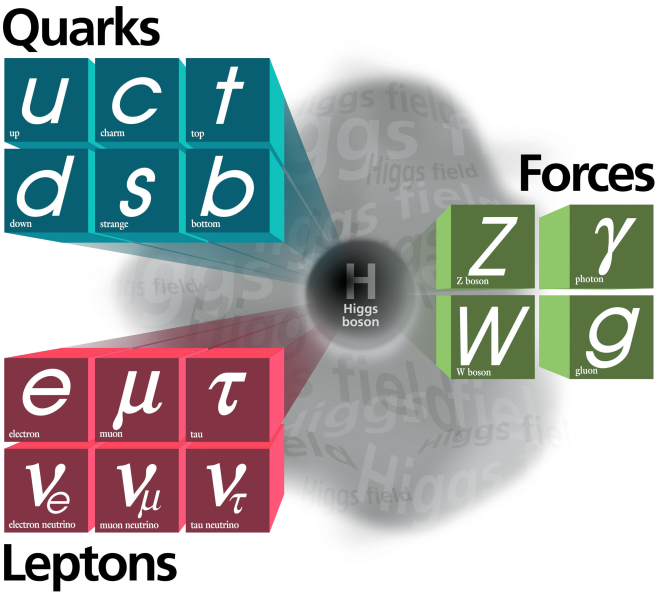

Figure 1.1: Elementary particles classification according to the Standard Model. Figure taken from [fer].

other decays into them. Every particle of this list contains an anti-matter equivalent, a particle with charge and all the quantum numbers opposite to its matter sibling. Together they form a set of 24 particles.

Standard Model considers three types of fundamental forces through which those particles can interact: electromagnetic, weak and strong interactions. Each of them is defined by the quantum field theory with at least one of the gauge bosons that acts as an interaction carrier. Electromagnetism is described by the Quantum Electrodynamics (QED). It is the longest known and best described of all the interactions on the microscopic level. It defines massless and charge-less photon (γ) as it's force carrier and affects all the bodies that caries the electric charge.

Weak interactions affects all the elementary particles. That force manifests itself in the reactions where the elementary particles change their types, with an exchange of one of the massive $W\pm$ or Z bosons. As mentioned earlier, it is described by the electro-week theory, which unifies it with the electromagnetism into one type of interaction which range and strength dependent on the carrier mass.

The last one, strong force, is the interaction that occurs only between quarks. It is defined by the Quantum Chromodynamics (QCD), an SU(3) gauge theory based on the color charge exchange, that happens through gluons, the force carriers. Unlike photon and W/Z bosons, gluons not only participates in the color charge exchange, but contains such themselves. That causes them to interact with the strong field which makes the properties of the strong force unique among the other interactions.

The attraction force between the color caring particles increases with distance and causes the quarks and gluons to stay inside the hadrons, which is reported as quark confinement (one could say they are trapped inside the particles). For that reason free quarks have never been observed directly.

Standard Model is not a complete picture of nature. It still misses the quantum description of the gravity which hasn't been fully developed yet. Apart from that, attempts are made to unify all the forces into one interaction. Those approaches are usually referred to as the Grand Unified Theories [Per00].

1.3 Quark-Gluon Plasma

The nature of the strong interactions causes also, that on the very small distances this force nearly vanishes. That effect, called an asymptotic freedom, was used in 1975 by John Collins and Malcolm Perry to propose the existence of new state of matter, a form of quark-gluon "soup" within which the particles can float freely [Col75]. They suggested that this state can be achieved in the high energetic collision of heavy nuclei, when the matter is being compressed to the level where the boundaries between the nucleons becomes blurry. This state was later called the Quark-Gluon Plasma (QGP) [Sat12]. The name was proposed by Prof. Edward Shuryak (SUNY at Stonybrook University, USA) as a similarity to the gas plasma, where the atoms are stripped down form electrons.

1.3.1 Phase diagram of the strongly interacting matter

The phase diagram of the strongly interacting matter depicts the relation between the net baryon density (μ_B) and the temperature (T), which is proportional to the mean kinetic energy of the particles (fig. 1.2). It is usually presented in the way where the nuclear matter, the one which occurs inside the nuclei, resides in the point of $\mu_B = 1$ and $T = 0$. For the higher temperature values, where the remnant strong force can no longer hold the nucleons together and the hadrons behaves as a separate entities, system becomes a hadron gas, represented by the white region on the fig 1.2.Finally, when the energy density is sufficiently high, the state of Quark Gluon Plasma occurs (the orange part of the plot).

Apart from that, strongly interacting matter is predicted to exist in the other, more exotic phases, like for example the color superconductors. This is expected to be a state similar to the electric superconductivity, however based on transporting the color charge by pairs of quarks ([Alf08] and references there in).

The phase diagram is still not well understood. Up to the current state of knowledge the type of the phase transition between the QGP and the hadron gas varies as a function of baryon density. At the $\mu_B = 0$ calculations performed by Lattice QCD technique allowed to predict that this transition is a cross-over, a type where the boundary between the two phases cannot be defined unequivocally. This is probably the area where the early universe has changed it's state from QGP into the hadron gas. For the higher baryon densities a critical point, with a second order

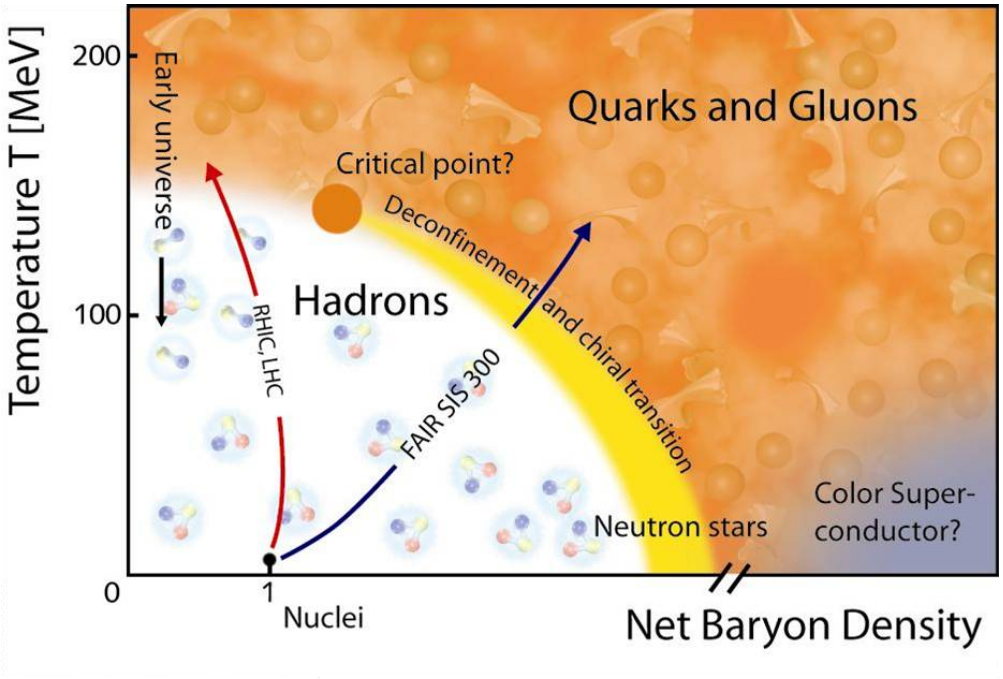

Figure 1.2: Phase diagram of the strongly interacting matter. Figure taken from [gsi].

phase transition, is expected to occur. It's exact location is nowadays a subject of intensive research [Luo12]. Beyond critical point it is presently believed that the matter exhibits a first order phase transition.

1.3.2 Evolution of the universe

QGP was most probably one of the states that the early universe went through during the first moments of its existence. The current knowledge on the development of early universe is summarized by the so called Big Bang model. It assumes the the universe began about 14 billion years ago as an effect of an explosion (Big Bang) of the point singularity with an infinite density of energy. The latter evolution is divided into stages called eras or epochs (fig. 1.3).

First of them was the Planck Era which began with the big bang and last till 10^{-43} s. It was a period in which the quantum gravity effects played most probably the dominant role. Since the theory of quantum gravity is still not complete currently there is no possibility to describe the processes that happened at that time.

The next epoch (before 10^{-35} s) is called the Grand Unification Era. It is believed that at that time all four fundamental interactions were unified into one universal force.

The beginning of the next period marks the moment when the strong force has decoupled from the universal interaction. This most probably led to the rapid expansion called inflation, which finished at 10^{-33} s.

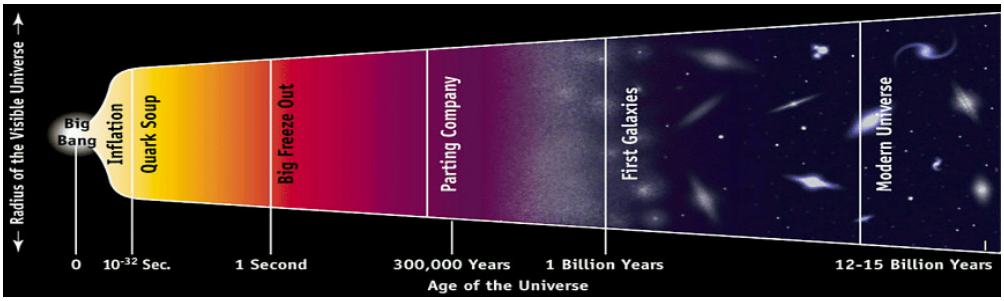

Figure 1.3: Evolution of the Universe. Figure taken from [na4].

The energy released during the expansion turned the strongly interacting matter in the early universe into the state of Quark-Gluon Plasma [All02]. It existed during the two consecutive epochs, the electro-weak era, which lasted till the energy has fallen below the level at which weak interactions decouples form the electromagnetism (10^{-12} s), and quarks era (10^{-6} s). The energy densities expected to happened in these eras are the highest which currently can be reproduced in the laboratory.

Later, the quarks started to form hadrons, which then built first nuclei, atoms and finally starts [Per00, Clo83].

1.4 Heavy Ion Collisions

The conditions favorable for the QGP formation are expected to occur in the high-energy collisions of the ions of heavy elements, like gold or lead. This is where the common names for this field of research comes from, heavy ion physics or high energy physics.

The typical way of accelerating heavy nuclei is with a synchrotron, a ring-shaped device where the charged particles (like electrons, protons, ions) are rotating along the vacuum pipe. The acceleration takes place in the cavities with an alternating electric field, synchronized with the the beam rotation frequency.

Synchrotrons can be divided into two particular groups, single-beam devices and colliders. In the first one particles are being accelerated to the given energy and then made to collide with the stationary block of material in which they are supposed to produce the QGP state. The measuring apparatus is located on the other side of the target. The advantages of this configuration are:

- high event rate
- Easy experimental arrangement as compared to colliders
- Easy change of target

However this setup greatly limits the effective energy of the collision, for example the Super Proton Synchrotron (SPS) delives Pb beam at the energy of 158 GeV

per nucleon which corresponds to the center-of-mass energy $\sqrt{s_{NN}} = 17.3\text{GeV}$ for a nucleon pair in the lead-lead collision.

Higher energies can be achieved in the collider, accelerator that uses two, separate, counter-rotating beams. The energies of those beams sum up, thus Relativistic Heavy Ion Collider (RHIC), which is capable of producing Au beams with maximum energy of 100 GeV, can generate a collision of $\sqrt{s_{NN}} = 200\text{GeV}$. The collisions happen in the predefined places, called the interaction points, surrounded with the particles detectors. In addition such approach has the following advantages:

- The energy available is double the beam energy
- center-of-mass system coincides with the laboratory frame
- detectors can cover almost full spherical angle around the interaction point

That comes with a price of lower event rate, as the collisions happens between two beam, with much lower density than the solid target in the case of single-beam devices.

Currently there are three accelerators used for the study on quark-gluon plasma: already mentioned SPS, located at the The European Organization for Nuclear Research (CERN) near Geneva, Switzerland, RHIC at Brookhave National Laboratory, New York, and the Large Hadron Collider (LHC) at cern. Two other devices are in the stage of developement, single-beam Facility for Antiproton and Ion Research (FAIR) at the Hlmholtzzentrum für Schwerionenforschung (GSI) at Darmstad, Germany and the Nuclotron-based Ion Collider fAcility (NICA) in Dubna, Russia.

1.4.1 Evolution of heavy ion collision

There are two possible scenarios of the heavy ion collision: a case where the energy density is too low to form the QGP and one in which the state of plasma appears (fig. 1.4). Border value of the energy density required to obtain QGP is determined on the basis of the measurements done with the lattice QCD. According to the current estimations it varies between 0.6 to 1 GeV/fm^3.

If the energy density is sufficient, shortly after the collision ($\tau_0 \sim 0.6\text{fm/c}$) system reaches the thermal equilibrium and the quark gluon plasma is formed. However, the large pressure generated by highly concentrated nuclear matter causes the system to expand rapidly. During that expansion the density of energy decreases which leads to hadronization, a process where quarks are being binded together into hadrons. The moment when composition of all hadrons becomes fixed is called the chemical freez-out. After that interactions between the particles are only possible through the momentum exchange. As the system continues its expansion those interaction vanishes as well (thermal freez-out). The only phenomenons which can happen beyond that point are decays of unstable particles created in the collision.

The short lifetime of plasma ($\sim 10^{-23}$ s) as well as small system size ($\sim 10^{-14}$ m) makes it impossible to observe the QGP directly. All conclusions about the

phenomena occurring in it comes from the analysis on final state particles registered by the detectors.

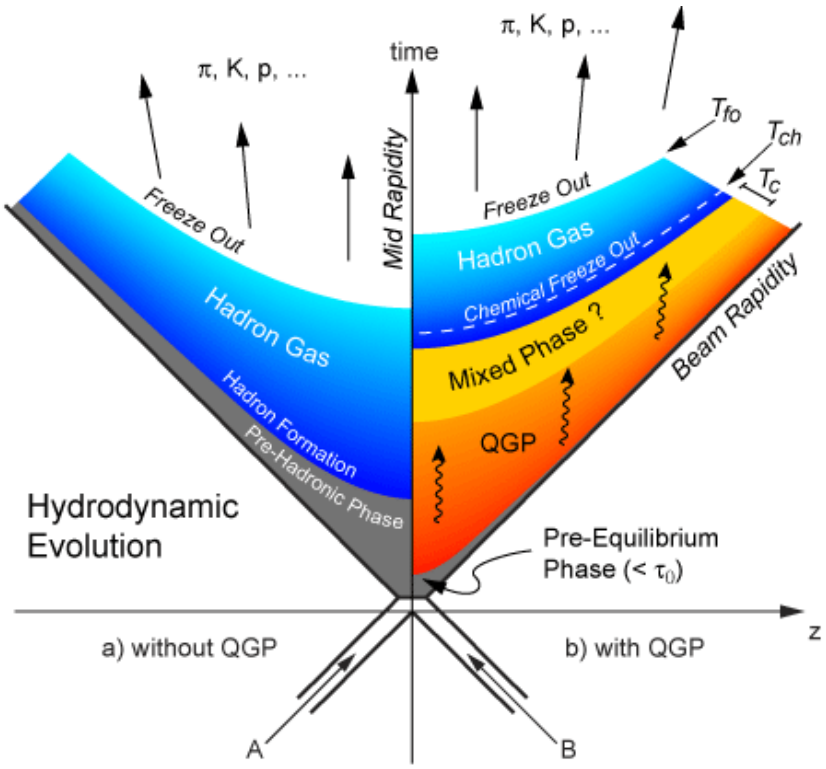

Figure 1.4: Space-time evolution of the heavy ion collision in the case of QGP formation (right side) and without it (left side). Figure taken from [lbl].

Chapter 2

Heavy Flavor Quarks

Contents

2.1 Parton Energy Loss and Heavy Flavor 9
2.2 Beauty and Charm separation via e-h and e-D^0 angular correlations 11
2.3 Motivation of the Thesis 16

2.1 Parton Energy Loss and Heavy Flavor

One of the major experimental observations for QGP that has been discovered at RHIC [Ars05, Bac05, Ada05, Adc05] is the so called "jet quenching", namely the energy loss of partons inside the hot and dense Quark Gluon Plasma, which is predicted to be a sensitive probe of the matter created in high energy nuclear collisions since its magnitude depends strongly on the color charge density of the matter traversed which can be estimated from measurements with the help of models. Fig. 2.1 shows one of the measurements of anomalous energy loss discovered in central Au+Au collisions at 200 GeV [Ada03]. The principal energy loss mechanism underlying these effects is commonly thought to be medium-induced gluon Bremsstrahlung, which is expected to dominate collisional (elastic) energy loss for very energetic partons [Wan95].

The energy loss in A+A collisions with respect to p+p can be quantified using the nuclear modification factor (R_{AA}), where the particle yield in heavy ion collisions is divided by the yield in proton-proton reactions scaled by the number of binary collisions. $R_{AA} = 1$ would indicate that nucleus-nucleus collisions can be considered as an incoherent superposition of nucleon-nucleon interactions. Initial-state effects, such as Cronin enhancement, nuclear shadowing and gluon saturation [Cro75, Hwa04] give an R_{AA} different from 1. Final state effects, such as radiative and collisionial energy loss in the QGP matter, result in an R_{AA} smaller than unity [Bai97].

Heavy flavor quarks namely charm and beauty, due to their large mass are produced at RHIC (Relativistic Heavy Ion Collider) mainly in the early stage of collision through the gluon fusion mechanism and therefore probe the complete space-time evolution of the collision process. They are sensitive to properties of the medium at the very first moments of the system formation and should be less affected by the energy loss than the lighter quarks. This is due to the so called

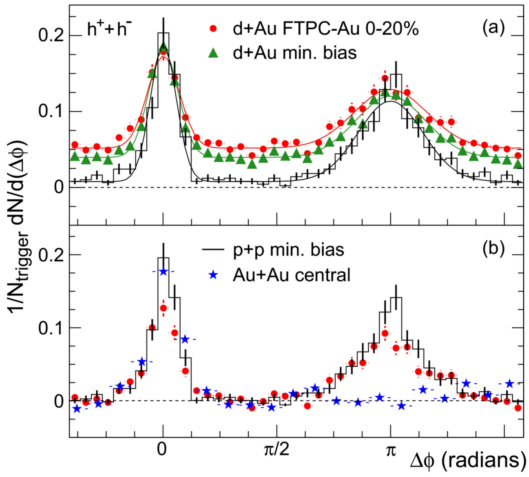

Figure 2.1: (a) Juxtaposition of two-particle azimuthal distributions for minimum bias and central d+Au collisions, and for p+p collisions. (b) Comparison of two-particle azimuthal distributions for central d+Au collisions to those seen in p+p and central Au+Au collisions. Figure taken from [Ada03]

dead cone effect, a suppression of the gluon radiation for the small angles [Dok01]. Together those mechanisms make the heavy quarks excellent probes to study the system properties at the early stage of collision.

Before the collection and analysis of RHIC data, it was generally expected that the dominant mechanism for the suppression of heavy quarks in the medium would be gluon radiation, and thus the heavy quarks would not be suppressed as much as the light quarks due to the dead-cone effect. The STAR and PHENIX collaborations have both measured a significant suppression of electrons originating from decays of charm and beauty in Au+Au collisions at 200 GeV [Abe07, Ada11]. This is illustrated in fig. 2.2 from PHENIX. Here the R_{AA} of non photonic electrons is shown as a function of pT for 0-10% central AuAu collisions. Several models are overlayed to the data. The suppression of open heavy flavor is similar to the suppression observed in light quarks, unlike the expectation that heavy quarks should show less energy loss than light quarks. Since the mass dependence arises mostly for the case of radiative energy loss it is important to access the percentage of radiative and collisional energy loss using models and data at several energies and systems to be able to constrain the models, as well as using different signatures, in particular the elliptic flow offering a major input to dissolve these questions.

Predictions from the BDMPS model and DGLV model for radiative energy loss can be seen in Fig. 2.2 [Arm06, Wic07]. The thick dashed curve is the BDMPS [Arm06] calculation for electrons from D and B decays. The bands are DGLV [Wic07] calculations for electrons from D and B decays. It is seen that the estimates from those models with mainly radiative energy loss does not fit the data. The lower band contains collisional energy loss as well as radiative energy loss. The thin dashed curves are DGLV calculations for electrons from D decays only. On the

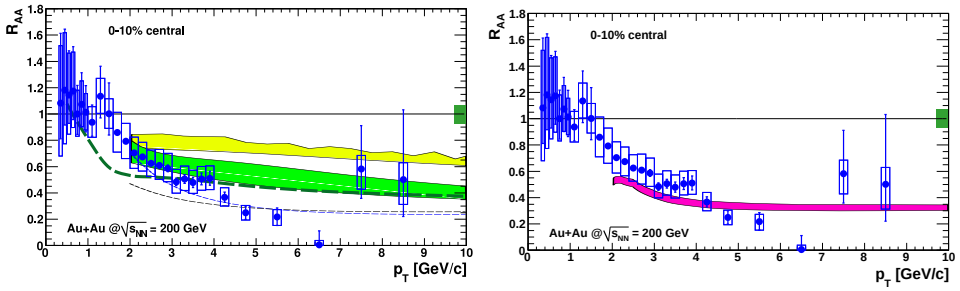

Figure 2.2: R_{AuAu} of the heavy flavor originated non-photonic electrons in comparison with the models. On the left plot the thick dashed curve is the BDMPS calculation for electrons from D and B decays. The bands are DGLV calculations for electrons from D and B decays. The lower band contains collisional energy loss as well as radiative energy loss. The thin dashed curves are DGLV calculations for electrons from D decays only. On the right plot the pink band is a collisional dissociation model. Figures taken from [Ada11]

right plot the pink band is a collisional dissociation model [Adi07].

Several other models are in process to describe the data on energy loss in heavy ion collisions understand the mechanism of energy loss and extract the QGP gluon density. For example Gossiaux and Aichelin [Gos08, Gos09b, Gos09a] calculated the R_{AA} from collisional energy loss in pQCD using a running coupling constant and replacing the Debye mass with a hard thermal loop calculation. The model finds a value close to the experimental R_{AA} for all centralities, while leaving room for a possible radiative contribution as well. Fig. 2.3 shows the R_{AA} as a function of pT and centrality from this model.

To explain the unexpected similarity of energy loss of heavy and light quarks and to constrain models in a way to disentangle the nature of energy loss the contribution of charm and beauty to the non-photonic electron spectra has to be determined separately.

2.2 Beauty and Charm separation via e-h and e-D^0 angular correlations

The STAR collaboration determined the relative contribution from B decays to non-photonic electron yields (rB) by measuring the azimuthal correlations between non-photonic electrons and charged hadrons (e-h), and between non-photonic electrons and D^0 mesons (e-D^0) in p+p collisions at 200 GeV [Agg10a]. The experimental e-h correlations has been fitted using a combination of PYTHIA calculations [Sjo01] for D and B meson decays and extract rB as a function of p_T in the region $2.5 < p_T < 9.5$ GeV/c. An independent measurement of the r_B is obtained from e-D^0 correlations, by selecting the charge combinations $e^- - D0(\rightarrow K^-)$ and $e^+ - \overline{D^0}(\rightarrow K^+)$ which provide relatively pure samples of B decays and charm pairs on near and away-side

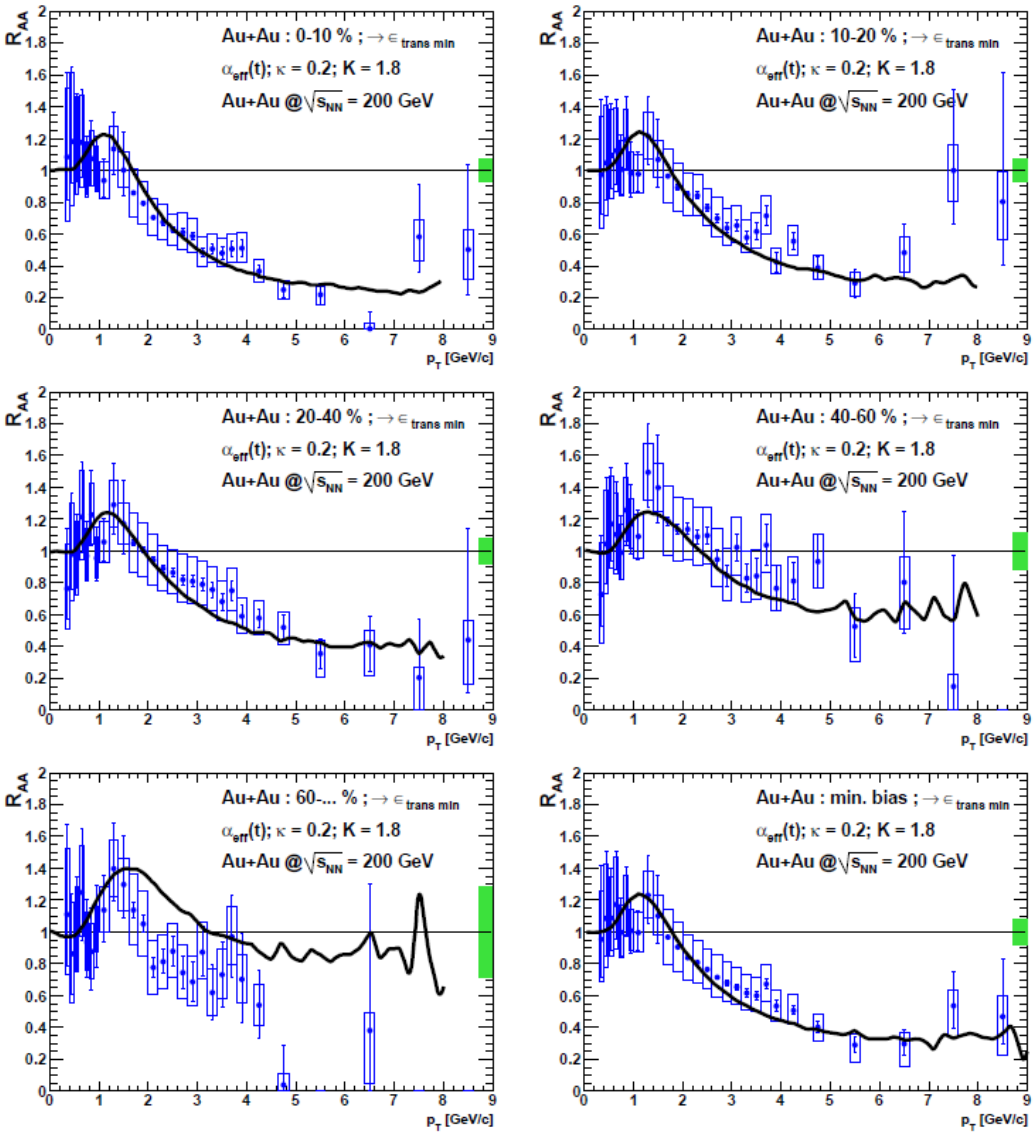

Figure 2.3: R_{AuAu} vs centrality and p_T from Gossiaux and Aichelin [Ada11]

($\Delta\phi$ π) [Mis09].

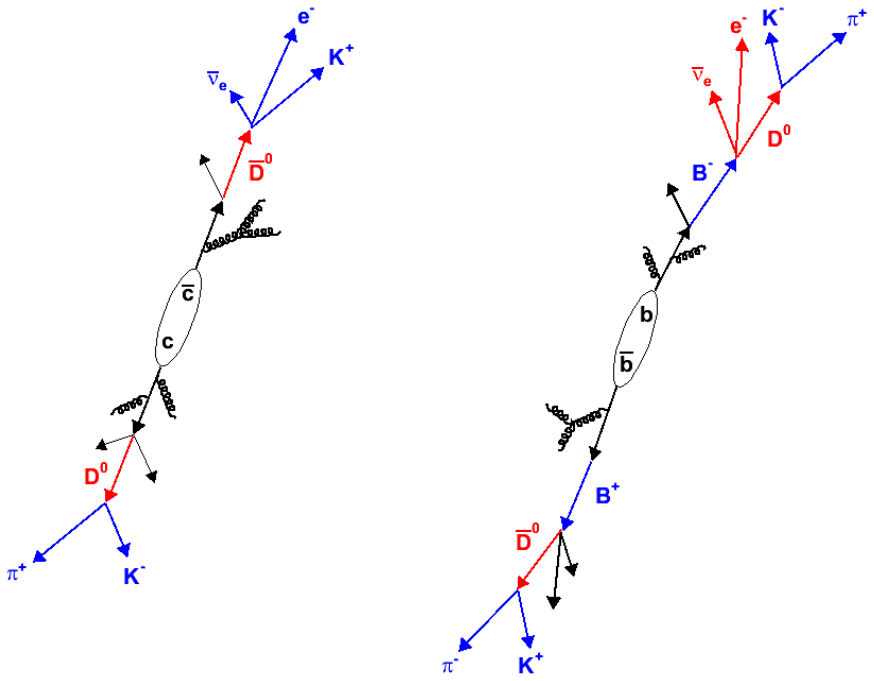

Figure 2.4: Schematic view of the fragmentation of a ccbar and a bbar pair

Flavor conservation implies that heavy quarks are produced in quark anti-quark pairs (ccbar and bbbar). A more detailed understanding of the underlying production process may be obtained from events in which both heavy-quark particles are detected. Due to momentum conservation, these heavy-quark pairs are correlated in relative azimuth (s) in the plane perpendicular to the colliding beams, leading to the characteristic back-to-back oriented sprays of particles (dijet). A dijet signal appears in the azimuthal correlation distribution as two distinct back-to-back Gaussian-like peaks around $\Delta\phi = 0$ (near-side) and $\Delta\phi = \pi$ (away-side). Fig. 2.4 illustrates a schematic view of the fragmentation of a ccbar and a bbar pair, respectively.

Assuming the trigger lepton is an electron from the fragmentation of a cbar or b quark, the partner charm quark must be a c, hence producing a K-pi+ pair. The bottom quark on the opposite side is a bbar, which yield K+pi- pairs via the main decay mode $B \to D^0 + X$ (BR = 59.6%). However, there is another channel, $B \to D^0 + X$ (BR = 9.1%) which give K-pi+ pairs. The $e^-K^-(e^+K^+)$ pairs are also expected from semileptonic B decays, e.g., $B^- \to D^0 e - \overline{\nu_e}$. Thus, electron-kaon pairs with the opposite charge sign (called unlike-sign e-K pairs) identify B decays on the away-side of the azimuthal correlation distribution of decay electrons and D0 mesons. Requiring like-sign e - K pairs select bottom on the near-side and charm and a small contribution from bottom (15%) on the away-side of the e - D0 correlation function. The above are illustrated with PYTHIA in fig. 2.5 which shows leading order PYTHIA azimuthal correlation distribution of non-photonic electrons

from charm and beauty contribution. Left it is shown for like-sign e-K pairs and right for unlike-sign e-K pairs.

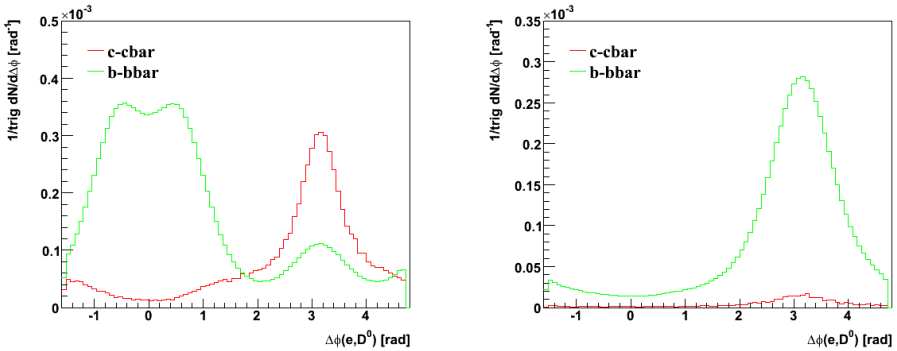

Figure 2.5: Leading order PYTHIA azimuthal correlation distribution of non-photonic electrons from charm and beauty contribution. Left it is shown for like-sign e-K pairs and right for unlike-sign e-K pairs.

For the STAR measurement of e-D0 correlations in p+p collisions at 200 GeV[Agg10a], D0 mesons were reconstructed via their hadronic decay $D^0 \to K^-\pi^+$ (B = 3.89%) and only events with a non-photonic electron trigger were used for D0 reconstruction. Furthermore, the kaon candidates were required to have the same charge sign as the non-photonic electrons. Fig. 2.6 shows the measured distribution of the azimuthal angle between non-photonic electron (positron) trigger particles and D0(antiD0). The solid (dashed) line is a fit of the correlation function from PYTHIA (MC@NLO) simulations to the data points. The bottom contribution rB is determined by fitting the measured e-D0 correlation with PYTHIA and MC@NLO and use the average of the two fits for the final value.

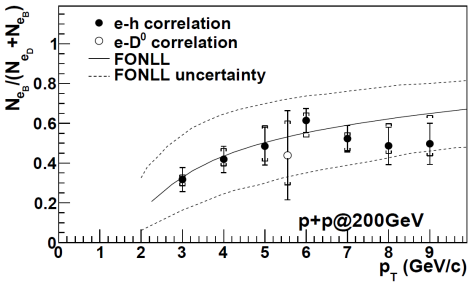

Figure 2.6: Transverse momentum dependence of the relative contribution from B mesons (rB) to the non-photonic electron yields. Error bars are statistical and brackets are systematic uncertainties. The solid curve is the FONLL calculation [14]. Theoretical uncertainties are indicated by the dashed curves.

Figure 2.7 shows the relative contribution from B mesons (rB) to the non-photonic electron yields $rB = N_{e_B}/(N_{e_B} + N_{e_D})$ extracted from e-h correlations

(filled circles) and e-D0 correlations (open circle) as a function of transverse momentum.The result indicates that the B decay contribution increases with p_T and is comparable to the contribution from D meson decay at p_T 5 GeV. The measurement is consistent with the FONLL calculation.

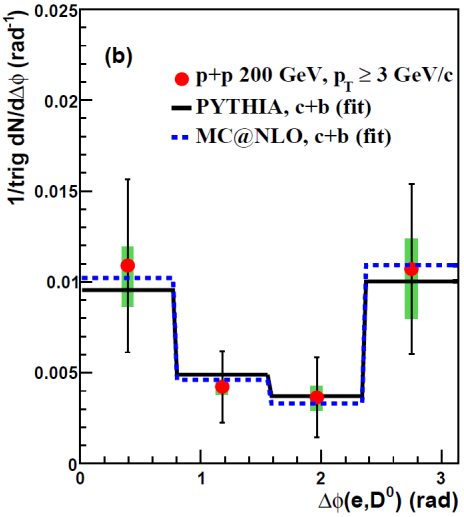

Figure 2.7: Distribution of the azimuthal angle between non-photonic electron (positron) trigger particles and D0(anti-D0). The solid (dashed) line is a fit of the correlation function from PYTHIA (MC@NLO) simulations to the data points.

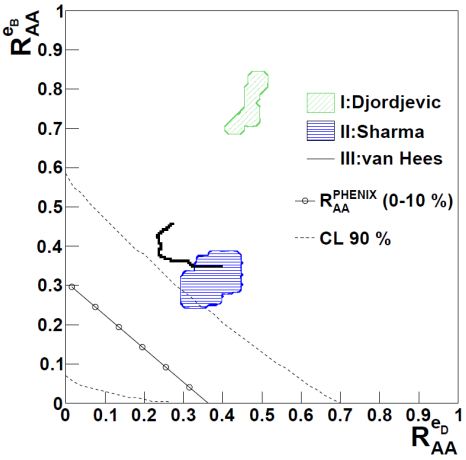

Figure 2.8: Confidence level contours for nuclear modification factor RAA for electrons from $D(R_A^{eD}A)$ and $B(R_A^{eB}A)$ meson decays in Au+Au collisions at 200 GeV determined by combining the RAA results and the rB measurement for pT $>$ 5 GeV/c and is compared to models.

The combined measurements of the B decay contribution and of the nuclear modification factor (RAA) for heavy-flavor decay electrons in Au+Au collisions

have been used to constrain the value of the RAA for electrons from B meson decay. [Agg10a]. In particular, as shown in fig. fig: 2.8 the ratio of rB combined with the large suppression of non-photonic electrons i indicates that RAA for electrons from B hadron decays in central Au+Au collisions at 200 GeV and $p_T > 5$ GeV is significantly smaller than unity. This measurement showed for the first time at RHIC that B meson production is suppressed at high pT in heavy ion collisions.

2.3 Motivation of the Thesis

In this thesis the measurement of the beauty contribution to non photonic electrons in p+p collisions at 500 GeV is investigated for the first time. This measurement is going to supplement the measurement of beauty contribution via e-h correlations which is the subject of another STAR thesis. Furthermore the production of D^* mesons in p+p collisions at 500 GeV is measured for the first time at a pT higher than 6.5 and up to 18 GeV applying a new method. The above measurements will constrain models trying to understand charm and beauty production at RHIC in p+p and A+A collisions and notably contribute to understand and interpret the suppression of heavy flavor in A+A at RHIC.

Chapter 3

Experiment

Contents

3.1 Detector 18
3.1.1 Time Projection Chamber 19
3.1.2 Time of Flight 19
3.1.3 Electromagnetic Calorimeter 19
3.2 Data reconstruction 20

STAR (Solenoidal Tracker at RHIC) is an experiment dedicated to study the matter on the scale of subatomic particles, namely to look for and analyze the Quark-Gluon Plasma. It is hosted in the Brookhaven National Laboratory (BNL), on Long Island, New York. Along with another experiment, PHENIX (Pioneering High Energy Nuclear Interaction experiment) it benefits from the ion collisions provided by the Relativistic Heavy Ion Collider (RHIC).

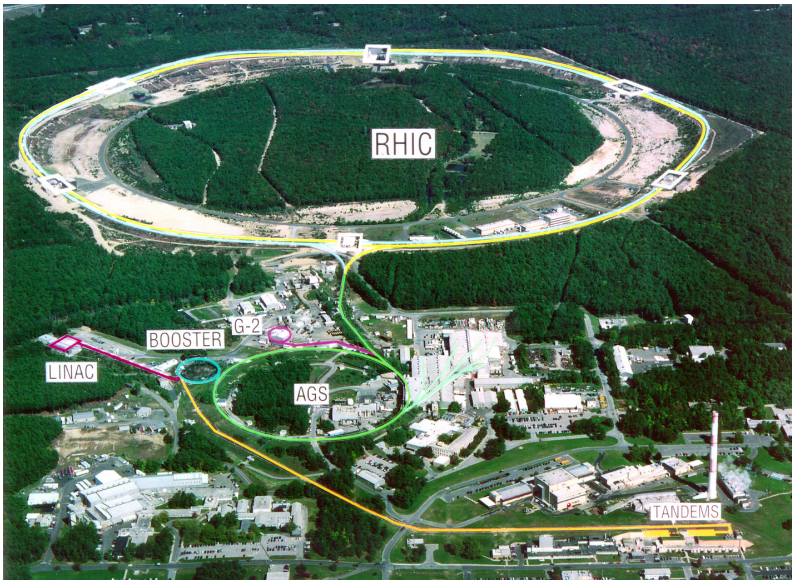

Figure 3.1: BNL accelerator complex [bnl].

RHIC is a collider, it contains two independent rings, there the ions are accelerated in the counter directions. Each ring is equipped with a set of beam focusing magnetic lenses and accelerating cavities. The so called interaction points, places

where the beams are made to collide, are located on the circumference of the device. Detectors are build around those places.

In order to provide the ion collision BNL has built a system of devices called the acceleration chain as shown on fig. 3.1. The ions are extracted form the source and preaccelerated in the Van de Graaff Tandem, a static field accelerator. Then they are being sent to Booster, a small linear accelerator which speeds them up to 37% of the speed of light. Next They are being extracted to the Alternating Gradient Synchrotron (AGS) which speeds them up to 10 GeV per nucleon. Finally the ions are being extracted to each of RHIC's rings where they are being accelerated to maximally 200 GeV/c (for the gold ions) and 500 GeV/c (for the protons).

3.1 Detector

STAR detector (fig. 3.2) is a versatile device which consists of many subsystems that allows to register different aspects of nuclear collisions. For the purpose of this analysis the following detectors were used:

- Time Projection Chamber
- Time of Flight
- Electromagnetic Calorimeter

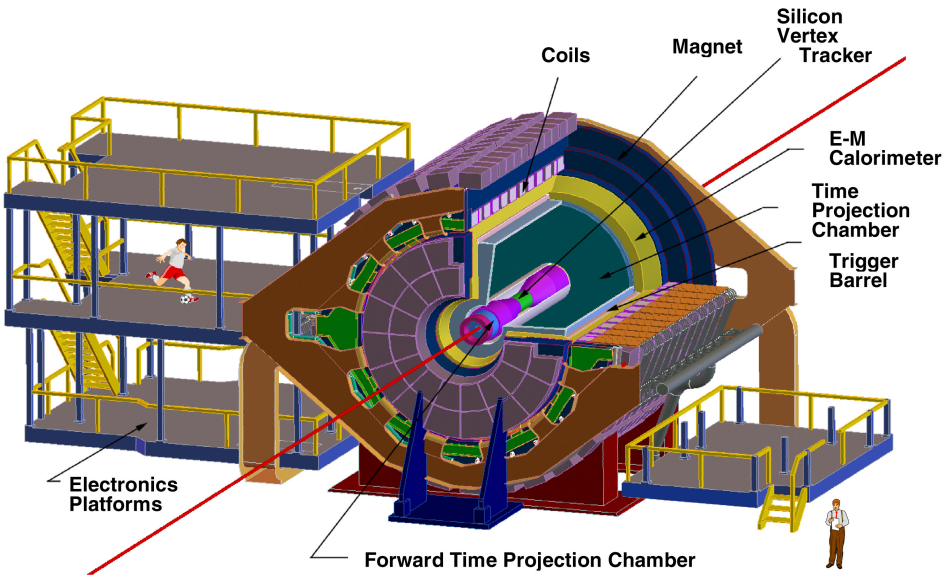

Figure 3.2: The STAR Detector. Silicon Vertex Tracker marked on the picture was removed after the run of 2007. Picture taken from [sta].

The coordinate system adopted for the data analysis uses the Cartesian coordinate system with the center located in the middle of Time Projection Chamber. The

Z axis is align along the beam pipe and the xy coordinates defines the transverse plain.

3.1.1 Time Projection Chamber

The main tracking device of STAR is a type of Time Projection Chamber (TPC). It is a barrel shaped drift detector with full azimuthal acceptance, a diameter of 4 meters and length of 4.2 m. During the operation it is filled with the P10 gas, a mixture of Ar and CH_4 in 90:10 proportions, under a pressure of 2 mbar above the atmospheric one to prevent the possible contamination. The charged particles that passes the chamber interacts with the gas through the process called ionization loss. This phenomenon based on the effect, that the charged particle which passes next to the atom can deposit some of its energy to kick out the electrons form its valence band. The amount of energy transfered into the medium that the charged particle passed through is proportional to it's type and momentum. This allows to identify the species of registered tracks.

The endcups of the detector serves as anodes, while the membrane installed in the middle of it's length is the cathode. Together they generates a linear electric field of 28 kV. This causes the electrons released form the atoms in ionization acts to drift towards the endcups, where a surface of two dimensional readout is located. It is divided into 12 sectors, where each covers the angle of $\pi/6$. Every sector contains 45 readout padrows, which measures the total deposited charge in the function of time.

TPC is located inside the magnet capable of generating constant magnetic field up to 0.5T. This is used to curve the charged particles trajectories inside the detector, which later allows to measure the momentum and charge of the track [And03].

3.1.2 Time of Flight

As the particle identification provided by TPC is not sufficient to distinguish between the species in the low momentum region, STAR has been equipped with the Time of Flight (ToF) subsystem, located on the outer border of the TPC. As the name suggests it measures the time with that takes for the particles to travel from the point of interaction to the surface of the detector with the precision of 85 ps. Then, by knowing the position of the interaction point the speed (β) of each particle can be calculated. Finally, with the momentum obtained from the TPC the mass of the particle can be provided [Bon03].

$$m = p\sqrt{\frac{1}{\beta} - 1} \tag{3.1}$$

3.1.3 Electromagnetic Calorimeter

The electromagnetic calorimeter is located above the ToF, 223 cm away from the center of the detector. It consists of 4800 towers with a base of approximately 10x10

cm each, which corresponds to the coverage of $\Delta\eta x \Delta\phi = 0.05 \times 0.05$. Every tower is build of alternating interweaving 5mm thick layers of lead and plastic scintillator. It consists of two parts, the inner with 5 layers of each material, and outer, where are 16 layers of scintillator and 15 of lead. Between those another system, the Shower Maximum detector is located. It is composed of two layers of strips oriented along the η and ϕ direction. Together they allow to improve the resolution of the subsystem as well as for electron identification, as they possesses the capability of measuring the size of the shower developed by the particles which travels through the calorimeter [Bed03].

3.2 Data reconstruction

Date registered from the collisions comes as a set of electric signals from the diffent subsystems of the detector. In order to perform any analysis they have to be first reconstructed. This process begins with a search for the points in the TPC where the particles caused ionization. For this the XY location of the signaled padrow is taken to form the position of every point in the transverse plain. Next the time on which signal has arrived to the padrow is used to calculate the position along the Z axis. With this finished the points are then used to fit the track path. For this the function of helix is used. Tracks reconstructed in this way are called the global tracks.Their are then used to find the position of the primary vertex. With this one fixed, the tracks that passes not more than 3 cm from it (Distance of Closest Approach - DCA $<$ 3 cm) are refitted with the vertex as an additional point. They are stored separately as so called primary tracks.

Chapter 4

Data Analysis

Contents

4.1 Data Preselection 22
4.2 D meson reconstruction 25
4.2.1 Invariant Mass 28
4.2.2 Decay Geometry Study 28
4.3 Electron identification 35
4.3.1 Matching to BEMC 35
4.3.2 Identification cuts 36
4.3.3 Electron purity 39
4.3.4 Non-photonic electron selection 40
4.4 Angular correlations 42

All studies described in this work were done using ROOT, software library for scientific analysis, and its dedicated version, StRoot, built for the purpose of the STAR experiment.

The analysis was performed on the three different datasets: proton-proton collisions at $\sqrt{s} = 500\text{GeV}$ collected in 2011 (called onwards as pp), Gold-Gold at $\sqrt{s_{NN}} = 200\text{GeV}$ from 2010 (AuAu10) and similar one from 2011 (AuAu11). For each of those a subset of so called High Tower events was selected. Those were the collisions for which a value above the threshold defined for the ADC value was measured in at least one tower of the barrel calorimeter (BEMC). That threshold was set to be 18, which corresponds to the energy of approximately 4.3 GeV deposited in the tower (fig. 4.1), and gave the following statistics in each of the datasets:

- pp - 160 M,
- AuAu10 - 59.5 M,
- AuAu11 - 94.3 M events.

While for the Au+Au collisions the High Tower events were separated from the minimum bias set during the data taking, for p+p it had to be done manually.

The purpose of this study was to measure open charm and beauty via the direct reconstruction of the D mesons.and their azimuthal angular correlations with the electrons. The latter allows to determine the ratio between the production of heavy

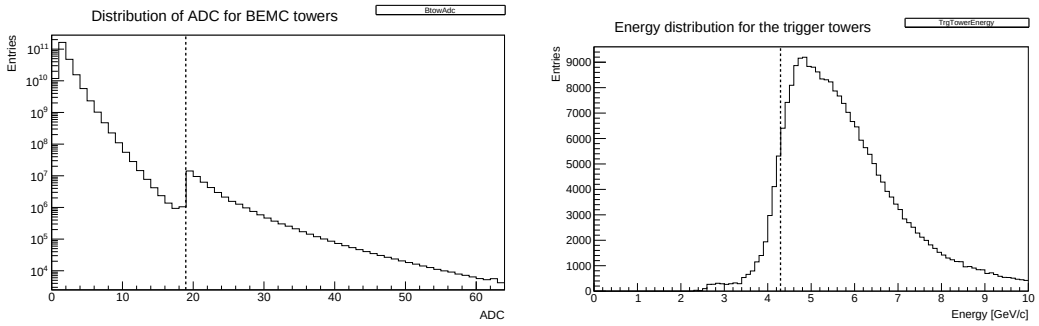

Figure 4.1: On the left: Distribution ADC values for the BEMC towers. The dotted line marks the cut position. On the right:Energy distribution for the trigger towers with an associated electron track (see sections 4.3.1 and 4.3). The dotted line marks the energy cut expected to occur with ADC threshold.

flavor quarks in the heavy ion and proton-proton collisions. For that reason a spectrum of D^0 meson has been measured as a function of the emission angle between the identified non-photonic electron and the meson itself. The analysis can be divided into following separate steps:

- Data preselection
- D^0 reconstruction
- Electron identification
- Angular correlations
- Yields analysis

4.1 Data Preselection

In order to obtain a subset of collisions useful for further analysis a set of data quality cuts was applied on the events and particle tracks.

Each accepted event had to meet the high tower criteria described above, which means it had to satisfy one of the following triggers:

- pp2011: 320501, 330501
- AuAu2010: 260504, 260514, 260524
- AuAu2011: 350503, 350513

Since the triggers are being reanalyzed during the data reconstruction process some events initially marked as high tower were dropped during this stage. Those that passed were checked for availability of every crucial detector used in this study: TPC, BEMC, SMD and ToF.

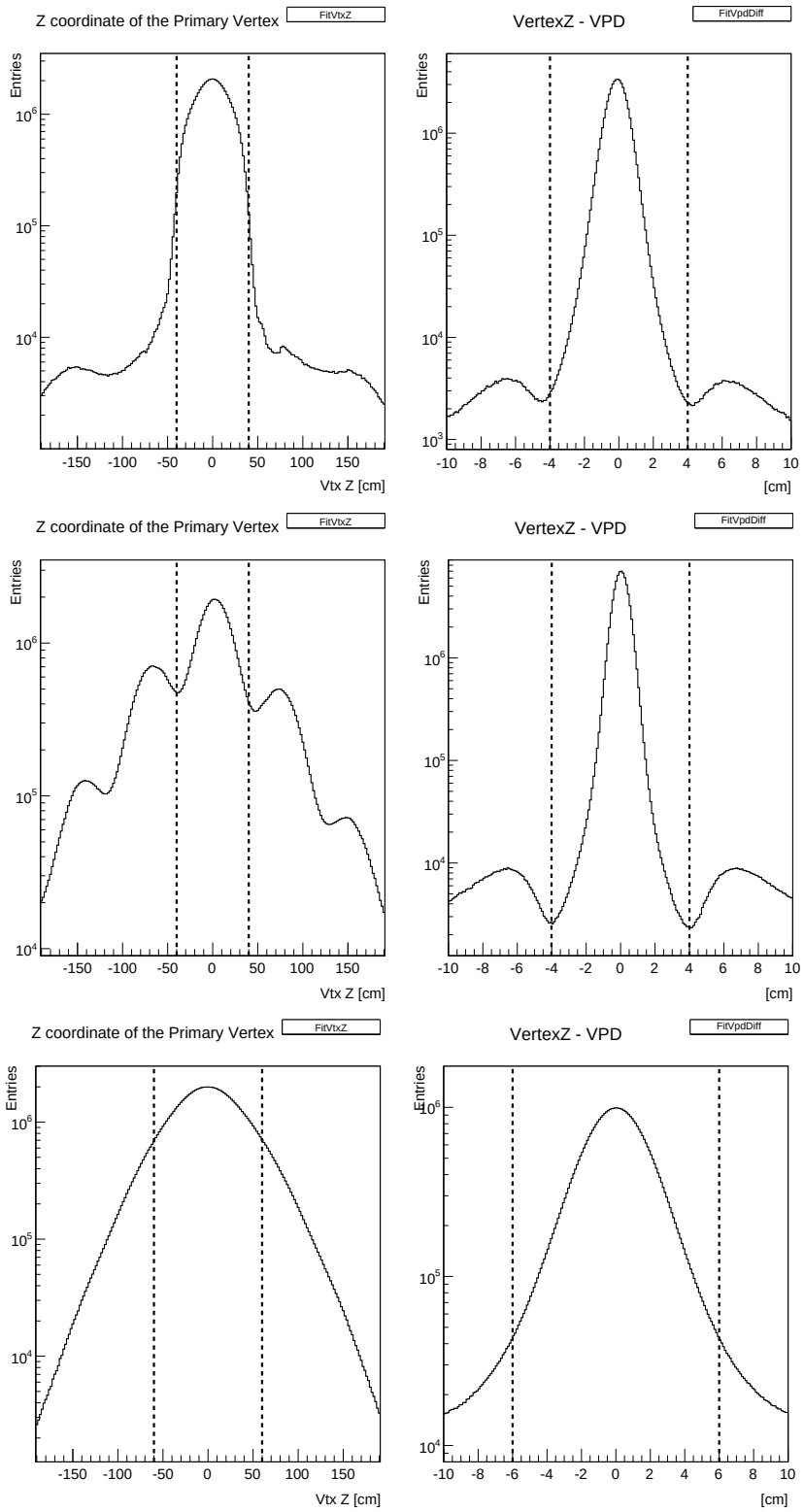

Figure 4.2: Distributions of primary vertex position along the z axis (on the left) and of the difference between the reconstructed vertex z coordinate and VPD result (on the right) for the AuAu10 (top), AuAu11 (middle) and pp (bottom) datasets. The dotted lines marks the ranges of accepted values.

Next a cut on the Z coordinate of the main vertex was performed. This cut is being defined by the experiment collaboration for each data set separately to optimize the data quality versus number of accepted events. The main goal is to eliminate the effects of the detector boundaries which can become visible for the collisions registered away from the center of the system. In the used datasets this values were set to $z \in (-40; 40)$[cm] for AuAu and $z \in (-60, 60)$[cm] for pp as shown on the figures 4.2. Finally, to avoid the situation in which the vertex used in analysis was different than the one that had triggered the event, a cut on the difference between the z coordinate of reconstructed vertex and the one calculated by the VPD (Vertex Position Detector) was used. The values were $|\ \mathrm{vtx(z)} - \mathrm{vpd}\ | < 4$cm in AuAu and $|\ \mathrm{vtx(z)} - \mathrm{vpd}\ | < 6$cm in pp. In addition the pp vertices were demanded to have a positive rank value. This parameter is calculated during the reconstruction process and is used to avoid pile-up events. It takes in account the number of the primary tracks which have a signal in one of the fast detectors, like BEMC or ToF. To get the positive rank vertex has to have at least two such particles associated with it.

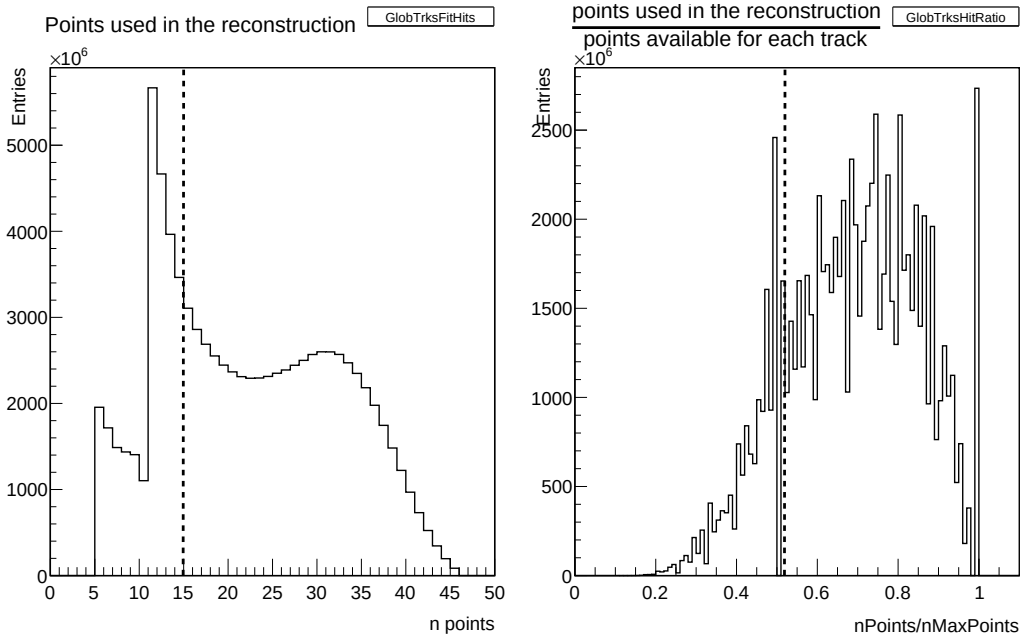

Figure 4.3: Distributions of number of hits used for the track reconstruction (on the left) and of the ratio between that value and maximal number of points available on the track path (on the right) for the AuAu10 datasets. The dotted lines marks the minimal accepted values.

Apart from the mentioned quality cuts all events were demanded to have at least one high tower electron. The details on this study were described in the section 4.3.

The output datasets consisted of:

- pp2011 - 214k,
- AuAu2010 - 253k
- AuAu2011 - 155k collisions.

For every event which have passed the quality cuts an analysis of global tracks was performed. Since this work focuses on the short-lived particle, which is expected to decay close to the main collision vertex, the number of particles was decreased by selecting only those which had a corresponding primary track. The remaining subset was then confronted with the reconstruction quality cuts (fig. 4.3):

- number of points used for the track reconstruction nPoints > 15
- ratio between the above value and the maximal number of points available on the track path $\frac{\text{nPoints}}{\text{nMaxPoints}} > 0.52$
- $|\eta| < 1.0$

Cut on the number of points used for the reconstruction assured the sufficient accuracy of the fit while the demand that more than the half of all points available on the track path had to be used for reconstruction allowed to avoid the so called split tracks, which occurs when a part of the points left in the TPC by the passing particle are being identified as a separate track. Pseudo-rapidity was limited to $|\eta| < 1.0$ as this is the acceptance of the detectors used in this study (TPC, BEMC, ToF). The tracks that passed all of this cuts where accepted for the further analysis.

4.2 D meson reconstruction

Hadrons that carries the charm quark decay in the weak processes way before they can be registered by any detector ($c\tau(D^0) \approx 123\mu m$, D^* is a resonance). Thus the only way to study those particles is to reconstruct them from their decay products. In this case the two charmed mesons were analyzed, $D^0(\bar{D}^0)$ and $D^{*\pm}$, in their hadronic channels:

$$D^0(\bar{D}^0) \to K^-\pi^+(K^+\pi^-)$$
and
$$D^{*+}(D^{*-}) \to D^0\pi^+(\bar{D}^0\pi^-) \to K^-\pi^+\pi^+(K^+\pi^-\pi^-)$$

with the branching ratio of

$$BR(D^0 \to K^\mp\pi^\pm) = (3.89 \pm 0.05)[\%]$$
and
$$BR(D^{*\pm} \to K^\mp\pi^\pm\pi^\pm) = 9.22 \pm 0.21[\%]$$

accordingly [Ber12].

The daughter particles were identified using the combined information on the dE/dx and the time of flight. In order to improve the accuracy of the identification in the pp dataset the ToF data was first analyzed to calculated the σ value for each particle species. That was done by subtracting the theoretical value of $1/\beta$ from the measured distribution for every species:

$$f(p) = 1/\beta - \sqrt{1 + m^2/p^2},$$

where m was the mass of the given particle type from [Ber12], and p was it's momentum. The outcome was then fitted with the Gaussian distribution, for which the standard deviation was used as an effective resolution of the detector $1/\beta_{\text{res}} = 0.012$. Finally the σ_{ToF} was recalculated using formula:

$$\sigma^K_{ToF}(p) = \frac{1/\beta - \sqrt{m^2/p^2 + 1}}{1/\beta_{res}}$$

.

Every particle was analyzed three times, first with an assumption that it is a kaon, second time as a pion and finally as a soft pion from D^* decay. However, to get accepted as any of those it had to pass the cuts shown in tab. 4.1.

Particle	p_T range [GeV/c]	cuts
Kaon	$p_T < 1.3$	ToF
	$p_T \in (1.3, 2.07]$	ToF $\vee \sigma_{dE/dx}(K) \in (-3.0; 3.0)$
	$p_T > 2.07$	$\sigma_{dE/dx}(K) \in (-3.0; 3.0)$
Pion	$p_T < 2.07$	$\sigma_{ToF}(\pi) \in (-3.0; 3.0) \vee \sigma_{dE/dx}(\pi) \in (-3.0; 3.0)$
	$p_T > 2.07$	$\sigma_{dE/dx}(\pi) \in (-3.0; 3.0)$
Soft Pion	$p_T \in (1.3, \infty)$	$\sigma_{ToF}(\pi) \in (-3.0; 3.0) \vee \sigma_{dE/dx}(\pi) \in (-3.0; 3.0)$

Table 4.1: Particle identification cuts applied to accepted cuts to preselect the daughter candidates.

Since the ToF information is available for about 60% of the registered tracks, demanding it for every particle would greatly reduce statistics in the further analysis. For that reason it was used only as a complementary to dE/dx in case of pions and as a main kaon identification exclusively in the region where the dE/dx bands for the different particle types overlays each other. Furthermore ToF was excluded from the analysis for the $p_T > 2.07$GeV/c which is the mean of p_T distribution for particles with momentum p = 2.4GeV/c, the point where the distinction between the pions and kaons has equal accuracy as the one available for dE/dx.

As the pions are the most abundant species of all the hadrons that can be measured directly (over 90%) the possible contamination of the sample would not have significant effect on the result. Thus the identification was done mainly with the dE/dx, and the ToF information was used supplementary when the given track

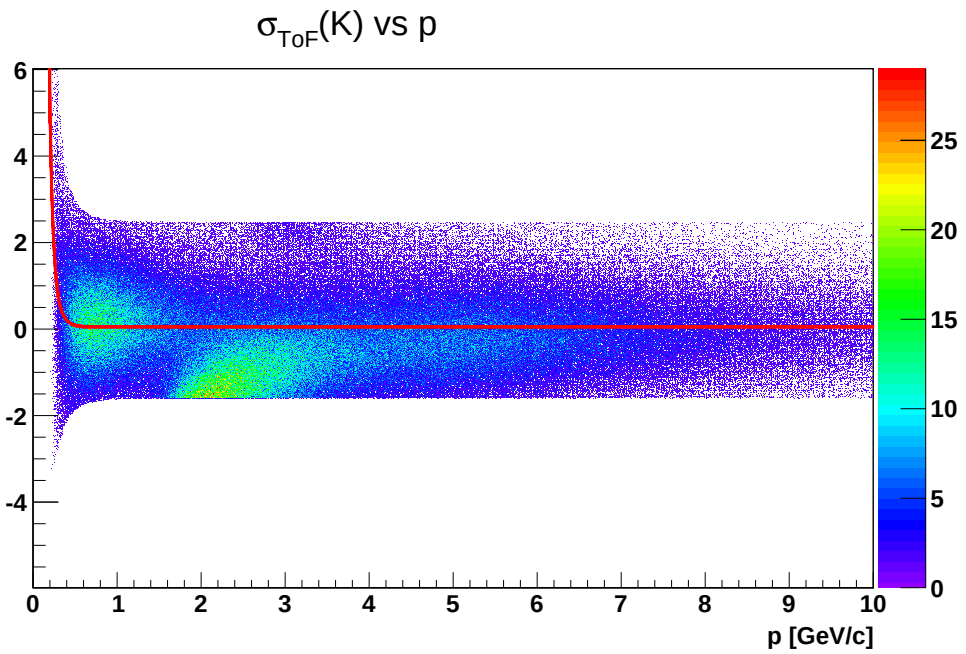

Figure 4.4: Visualisation of the $\sigma_{ToF}(K)$ cut applied for the pp data. Red line marks the M(p) function form equation 4.2

had it available. This was not the case with the kaons, where the ToF was the only detector used in PID for $p_T < 1.3$GeV/c as mentioned above. Additionally, in order to improve the statistics in the low momentum region, a function, presented in equation 4.2, was used to specify the range of accepted σ_{ToF}(K) values (fig 4.4). It was calculated from the results of the Gaussian fit performed on the σ_{ToF}(K) in the different momentum ranges. The obtained values of mean and standard deviation were then used to fit the power law function (4.2) designed to converge with the standard σ_{ToF} for the higher momentum. The final function consisted of two elements, M(p), which described the position of the mean value in the function of momentum, and W(p), that characterizes the width. The final cut was set to:

$$\sigma_{ToF}(K(p)) \in (-2.0 * W(p) + M(p); 3.0 * W(p) + M(p)).$$

This study was done on the pp dataset, but was also applied to the AuAu analysis.

$$M(p) = 3.16018e-02 + \frac{1.36866e-03}{(p + 1.01344e-01)^{6.89333}} \tag{4.1}$$

$$W(p) = \frac{8.83957e-01 + 1.74093e-02}{(p + 8.38958e-02)^{4.23066}} \tag{4.2}$$

4.2.1 Invariant Mass

Invariant Mass is the statistical technique which allows to estimate the amount of short-living particle production with the known decay channels. It is given by the difference between square sums of energies and momenta of the products of the decay of the analyzing particle. As a result a rest mass of the parent particle is provided in the coordinate system where c =1. The general form the the equation looks in the following way [Per00]:

$$M_{inv} = \sqrt{\left(\sum_i E_i\right)^2 - \left(\sum_i \overrightarrow{p}_i\right)^2}, \tag{4.3}$$

In order to measure the D^0 production the invariant mass around it's mass region was done for every $K^{\pm}\pi^{\mp}$ pair that passed the PID cuts. As the combinatorial background from the particles not associated with the charm decay is very high in this channel few approaches was taken to reduce it. For that reason an invariant mass was also calculated for the pairs which couldn't form the D^0, such as the like-sign pairs. In order to do that the results were separated into two distributions, one for the case when both particles had positive charge and the other for the case with two negative tracks. The final distribution was then obtained by performing $LS = \sqrt{PP * MM}$, for each bin of the histogram, where LS is the final distribution, and PP and MM are the distributions for positively and negatively charged pairs accordingly.

The other approach was to break the decay geometry by rotating momentum of one of the daughters by 180°. This background type was calculated for the same pairs as the initial D^0 distribution and was called rotational.

In the case of D^* the invariant mass was calculated for the trinities of $K^{\pm}\pi^{\mp}\pi^{\mp}$, where the first two particles had to form the invariant mass in the window around the D^0. The final distribution was obtained by subtracting the invariant mass value of those pairs from the invariant mass of the trinity. The final distribution was expected to show the final distribution of the D^* around 145MeV/c^2 as this is the difference between in mass between the D^0 and D^* mesons. As the peak is in the beginning of available phase space the background is very small in this region. Nevertheless, to reduce it, a two different background estimation methods were used. The side band, where the calculation described above was done with pairs that are out of the D^0 mass region, and the wrong sign, where the second pion was selected with the sign opposite from the combination that forms D^*.

4.2.2 Decay Geometry Study

As the heavy quarks are produced relatively rarely in the ion collisions, the subset of tracks selected with the identification cuts, especially for the AuAu collisions, was dominated by the particles that comes from sources other than the charm meson decay. Thus to get rid of at least some part of this combinatorial background, especially significant in the D^0 analysis, another techniques had to be applied.

When the parent particles decays in the magnetic field of the detector, the products of this process are traveling along the curved trajectories convergent to each other in the point where the decay happened (the so called secondary vertex). However, due to the limited tracking resolution of the TPC the helices that describes the paths of those tracks are usually shifted towards or away from each other. This prevents the explicit identification of the secondary vertex position. The approximate one can be obtained instead by finding the point of closest approach between the helices of the given tracks. It is done by the iterative minimization procedure placed inside the code of StRoot.

By knowing the secondary vertex position one can study the geometry of the potential decay. In this case the following parameters have been taken into account:

- distance of closest approach (DCA) between daughters - the distance between the helices at the point of closest approach
- decay length - the distance between the primary vertex of the event and the decay point
- opening angle - angle between the daughters momentum vectors at the decay point
- pointing angle - angle between the momentum of the reconstructed parent and the line which connects the primary and secondary vertices
- DCA product - a dot product between the vectors of DCA to Primary Vertex for each daughter track

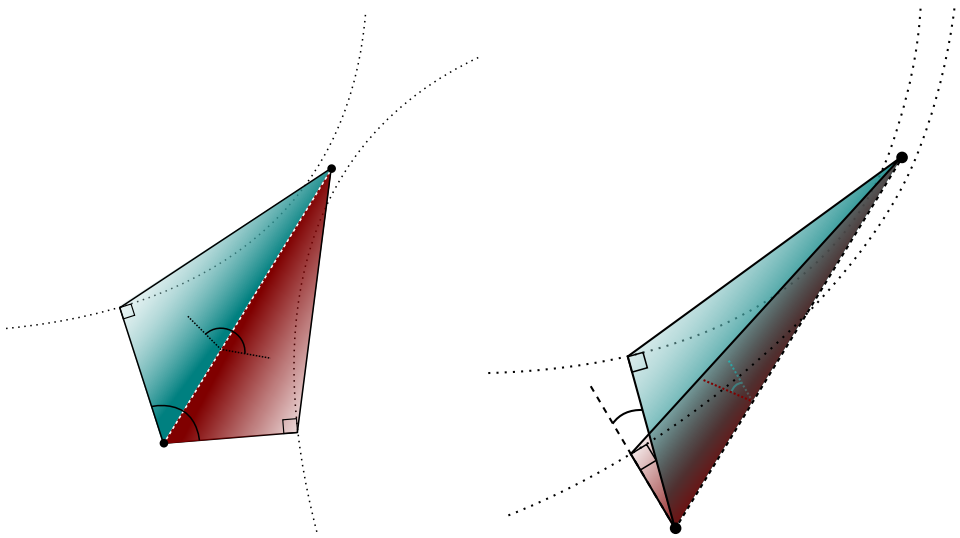

Figure 4.5: Geometry of the pair of particles that can come form the decay (on the left) and a pair that cannot form a decay vertex (on the right).

While the purpose of most of those variables is obvious, the DCA product requires an additional description. As it is shown on the fig. 4.5, the points of closest approach, primary vertex and the decay point forms triangles in the 3-dimensional space, one for each daughter particle. If the studied tracks originated from the decay of the same particle the angle between the plains formed by those triangles should be close to 180° (fig. 4.5 left), while for two randomly selected tracks there is no such constrain (fig. 4.5 right). That angle is strongly correlated with the angle between the vectors describing DCA to the Primary Vertex, namely it is expected to have more than 90° for the pair to be accepted as formed in a potential decay. Thus, the dot product for those vectors should take negative value.

In order to test that statement as well as to find the optimal cut value for every of the decay geometry parameters a simulation was carried out. A sample of 300k single $D^0 \to K^- + \pi^+$ decays was generated with the GEANT simulation toolkit in the detector environment from the year 2011. It used a flat distribution of transverse momentum for the parent particle and a Gaussian distribution for the primary vertex z coordinate. The complete set of the parameters used for this simulation is presented in tab. 4.2.

Parameter	Value
Vertex Z σ	$\sigma = 30$ [cm]
Vertex Z range	VtxZ $\in (-40, 40)$ [cm]
D^0 transverse momentum	$p_T \in (0.0, 8.0)$ [GeV/c]
D^0 pseudorapidity	$\eta \in (-1.0, 1.0)$

Table 4.2: Parameters used to simulate the D^0 decays with the GEANT framework.

In the next step, each decay was reconstructed as a separate event. Since the daughter particles does not always get reconstructed properly, as it can for example be emitted in the direction out of the detector acceptance, and the reconstruction software have troubles to find the vertex position with only two tracks emerging from it, the output dataset has been reduced to 192k events. Those have been then processed through the same analysis chain as the real data. As an outcome the D^0 peak was obtained with the mean $= 1.864 GeV/c^2$ and width $= 0.022 [GeV/c^2]$ as shown on the figure 4.7. The pure D^0 dataset was also used to generate the distributions of parameters mentioned above for comparison with the collected real data events. As can be seen on the fig 4.9, the DCA Product exhibited the described behavior for the vast majority of the reconstructed pairs. However, the pointing angle distribution, which one would expect to have it's maximum in the region of low angles, had a significant peak around the angle of 90°.

To eliminate the possibility of malfunction in the secondary vertex finder a test on an easily identifiable particle,Λ, was done, in the decay channel $\Lambda \to p + \pi$. Since Λ in RHIC is produced in a grate abundance it can be detected without any additional techniques. Nevertheless vertex finding procedure allows to reduce the background significantly. As the $c\tau$ of this particle is 7.89 cm the secondary

vertex can be easily distinguished form the main vertex of the event.

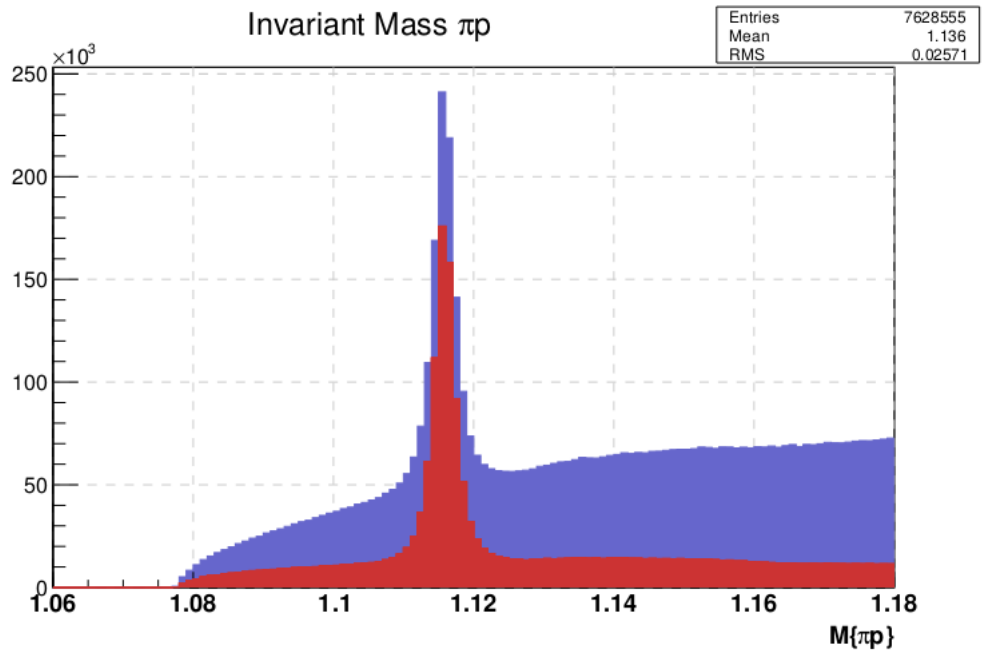

Figure 4.6: Invariant Mass of $p^{\pm}\pi^{\mp}$ pairs in the region of Λ peak with momentum recalculation to the point of closest approach (blue), and with additional cuts on Decay Length $>$ 3 cm, DCA btwn. Tracks $<$ 1 cm, opening angle $<$ 0.3 rad (red).

As can be seen on the fig. 4.6 the secondary vertex finder developed for charm worked well and reduced the background as expected, while the momentum recalculation at the point of closest approach made this peak more narrow and Gaussian shaped. This is not the case with the charm mesons. Studies performed on the pp data showed that the peak of D^* has decreased it's significance when the momentum recalculation procedure was applied. Cutting on the reconstructed decay parameters has only strengthen this effect up to the complete disappearance of the signal for demand on the DCA Product $<$ 0.

This results suggests that the secondary vertex finder works well. However, STAR currently does not provide sufficient resolution to isolate the vertices from charm decay. Thus the decision was made to abandon the secondary vertex finder in this analysis.

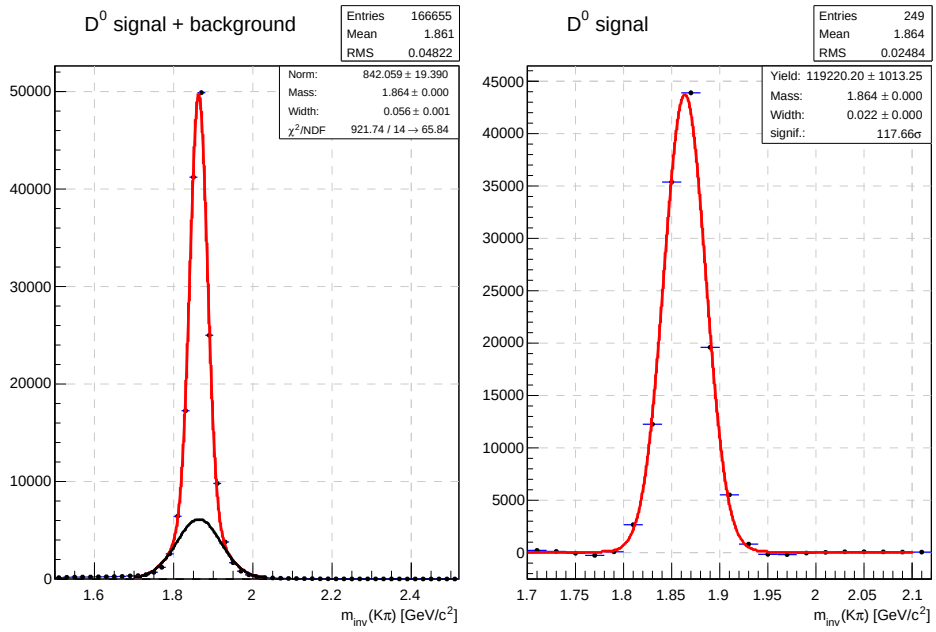

Figure 4.7: Invariant mass of the simulated D^0 sample. The background on the left plot (black line) comes form the wrongly identified D^0 daughters. The right plot shows the distribution after the subtraction of that background.

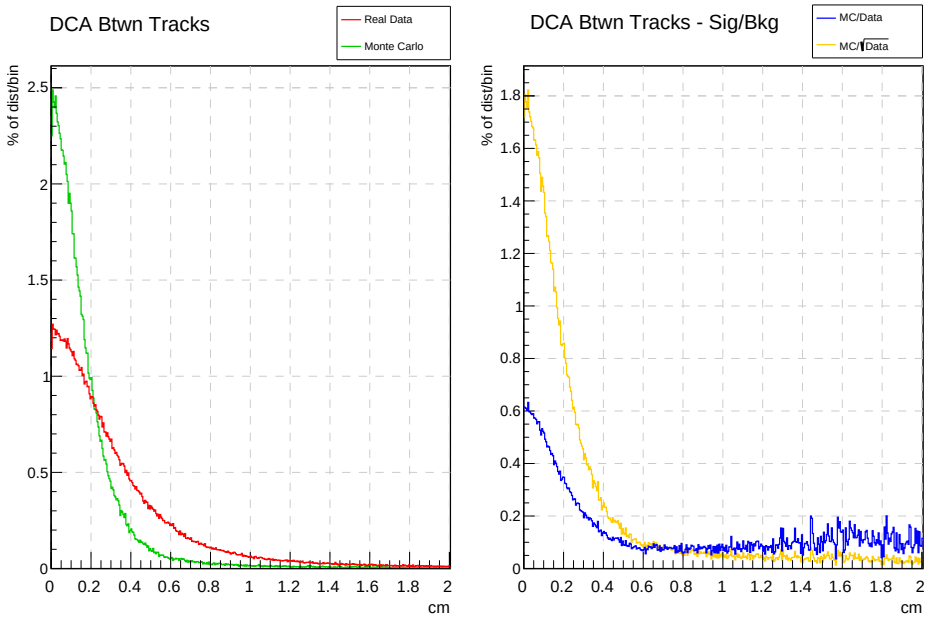

Figure 4.8: DCA between a pair of tracks from the real data (red) and simulated D^0 decays (green) along with the signal to background ratio (blue and yellow) calculated with an assumption that the data can be considered as the nearly pure background.

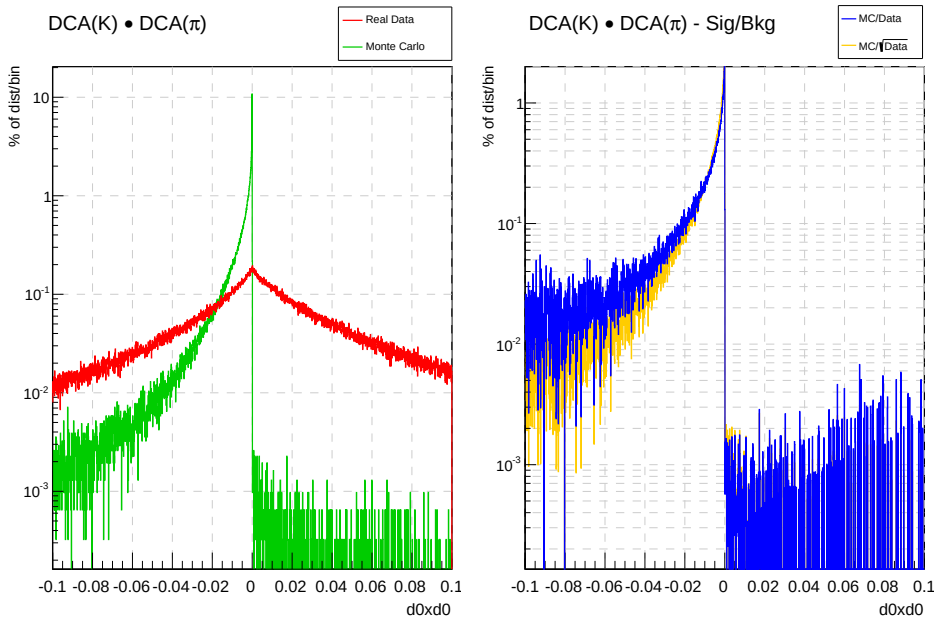

Figure 4.9: DCA product from the real data (red) and simulated D^0 decays (green) along with the signal to background ratio (blue and yellow) calculated with an assumption that the data can be considered as the nearly pure background.

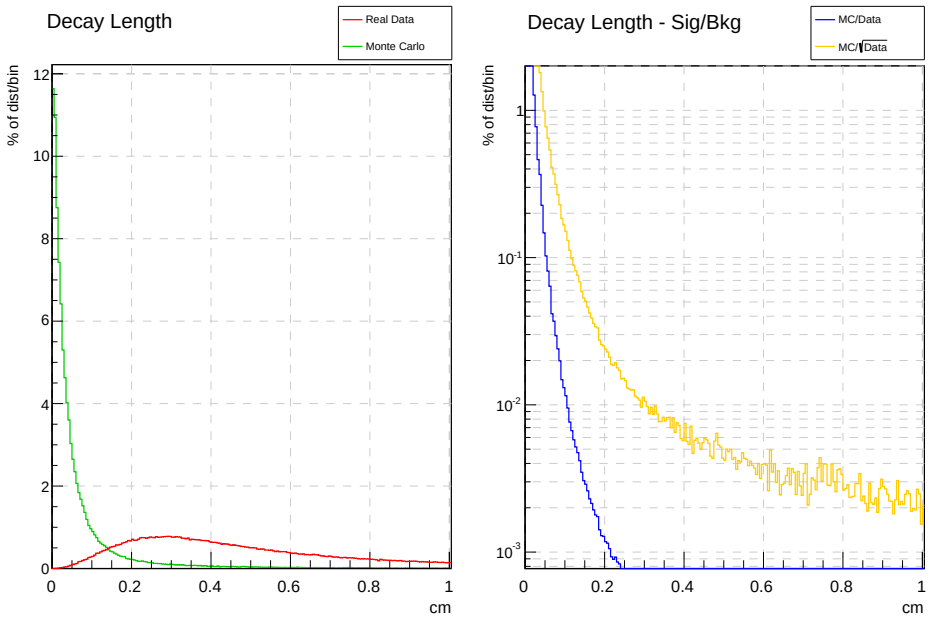

Figure 4.10: Decay length from the real data (red) and simulated D^0 decays (green) along with the signal to background ratio (blue and yellow) calculated with an assumption that the data can be considered as the nearly pure background.

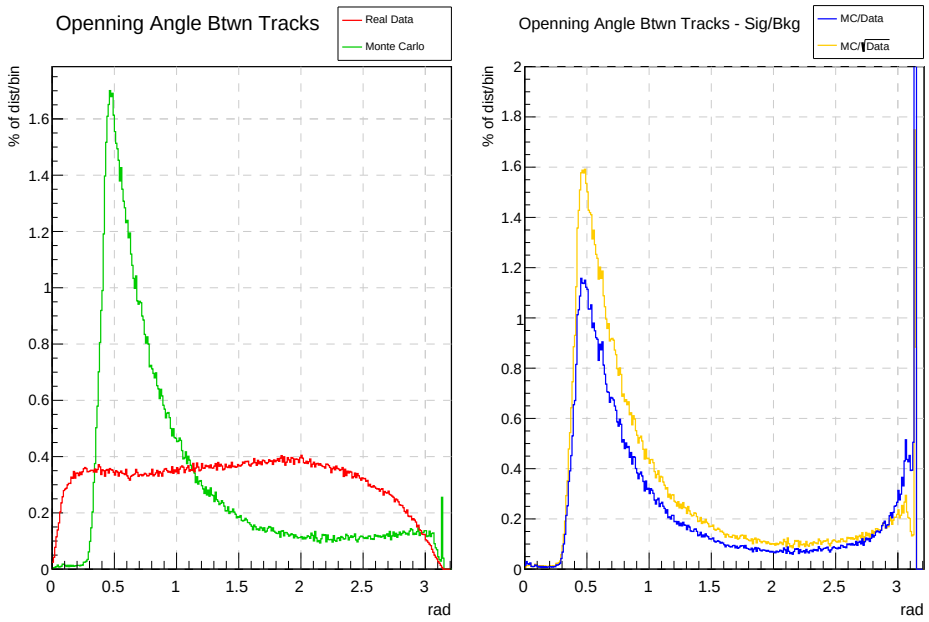

Figure 4.11: Opening angle from the real data (red) and simulated D^0 decays (green) along with the signal to background ratio (blue and yellow) calculated with an assumption that the data can be considered as the nearly pure background.

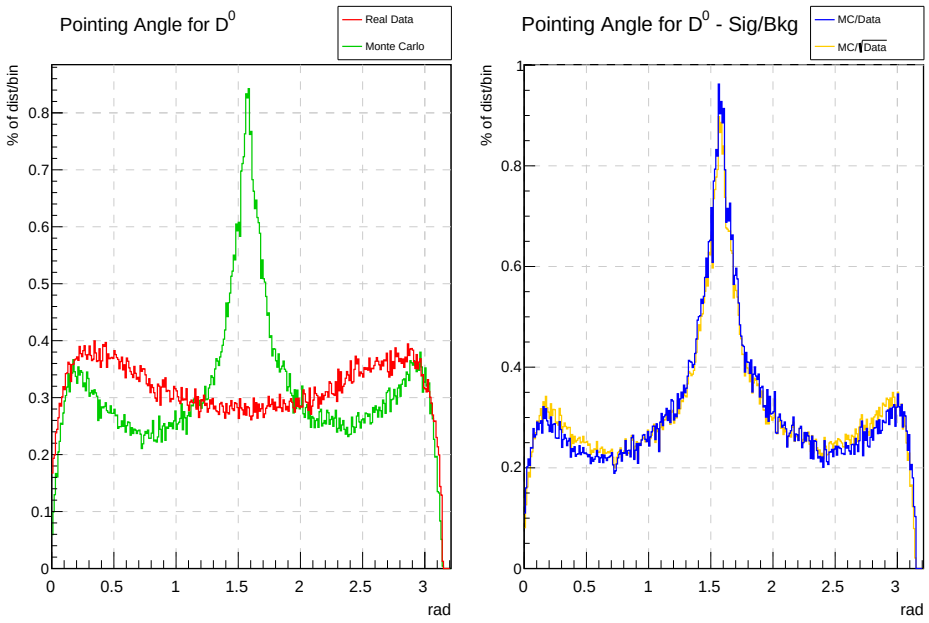

Figure 4.12: Pointing angle from the real data (red) and simulated D^0 decays (green) along with the signal to background ratio (blue and yellow) calculated with an assumption that the data can be considered as the nearly pure background.

4.3 Electron identification

4.3.1 Matching to BEMC

An additional procedure was applied to every track in order to find which of them are electrons. As the used method relies on the data provided by the BEMC all the particles with $p < 1.5 GeV/c$ had to be rejected. For the remaining tracks the calorimeter information was used to separate the electrons form hadrons. However, as the data collected by the BEMC is not being associated with the particles during the reconstruction. Thus this process, called matching, had to be done first.

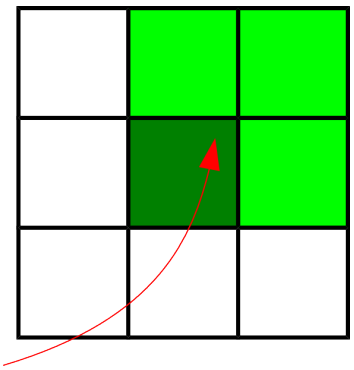

Figure 4.13: Picture presenting in the the schematic which towers are taken into account for each track projected to the calorimeter.

Matching was performed independently for every subsystem of the calorimeter. First the procedure was done for the BEMC towers. Each track was projected to the inner surface of the calorimeter in order to find the tower closest to that projection. That tower was then associated with the studied particle and will be called onwards as the closest tower. Apart from that, three neighbor towers, which were closest to the expected track position (fig. 4.13), were also considered. Among those four (three neighbors and the closest tower) the tower with the greatest amount of energy deposited in it was selected, it will be onward called as the highest tower. Finding the highest tower was crucial for this study as each electron, in order to be accepted for the further analysis had to have the tower that satisfies the high tower trigger criteria. For that reason, to increase the statistics, highest tower was used in the analysis.

To find the SMD clusters an other procedure had to be applied. Each track was projected to the surface of SMD in the same manner, but the closest cluster was obtained by the iterative comparison of the distances between each cluster and the expected track position. While the cluster selected in that manner was indeed the closest one, it didn't had to by the one to which the track really matches to. Thus, to ensure the proper accuracy, the distance cuts had to be applied. As STAR didn't have the well developed code for simulating electrons in the calorimeter, a sample of photonic electrons (which come form photon conversions and Dalitz decays) was

used.

The cuts were defined in two steps. Each of the SMD provides good measurement resolution only in one direction, while in the other it is defined by the physical size of the module. First the cut was performed in the direction (called onwards the wrong direction) where both SMDs have weaker resolution, thus ϕ for SMDη and Z for SMDϕ. It was done based one the visual interpretation of the distance distributions (fig. 4.14) and has been set to match the calorimeter submodule boundaries, $\phi \in (-0.051; 0.051)$[rad] for SMDη and z $\in (-16, 16)$[cm] for SMDϕ. While these boundary is well visible in ϕ direction as a gap in the distribution, the one for Z is smeared due to the differences in the submodule sizes along this axis.

In the next step the search for the closest cluster was redone with the wrong direction cuts set. This time to study the distance distribution in the other direction, in which both SMDs have higher resolution (the right direction). This was performed by fitting a Gaussian to the obtained plots (4.15). The accepted range was set to mean $\pm\, 3\sigma$ from the fitted distributions that was z $\in [-2.15932; 2.69345)$[cm] for the SMDη and $\phi \in [-0.01035; 0.01021)$[rad] for the SMD$\phi$. This study has been performed for every dataset. However the values acquired during the analysis of AuAu10 were used since the deferences between them were negligible.

In summary, a track approved for further analysis had to have:

- $p > 1.5[GeV/c]$
- a highest of four closest towers that satisfies the high tower trigger criteria
- an SMDη cluster within the distance of $\phi \in (-0.051; 0.051)[rad]$ and $z \in [-2.15932; 2.69345)$
- an SMDϕ cluster within the distance of $\phi \in [-0.01035; 0.01021)[rad]$ and $z \in (-16, 16)[cm]$

The study on the accepted particles had shown that those of them for which the highest tower was not the closest one are an insignificant part of the whole subset.

4.3.2 Identification cuts

The information obtained from the BEMC was used to select particles which potentially were electrons. First the data from the SMD has been taken for a study. As the simulations show (fig. 4.16), the electromagnetic shower developed by electrons is much wider than the one generated by hadrons. Thus by cutting on the shower shape one can greatly reduce the hadron contamination of the sample. The optimal value was defined to be at least 2 stripes in every SMD plains. In this analysis the distribution of SMD hits per cluster maximizes already for the value above the specified limit, as can bee seen on the fig. 4.17. This is due to the requirement, that each tower associated with the track has to pass the high tower trigger criteria. This also decreases the number of hadrons since they rarely develop showers strong enough to pass the trigger threshold.

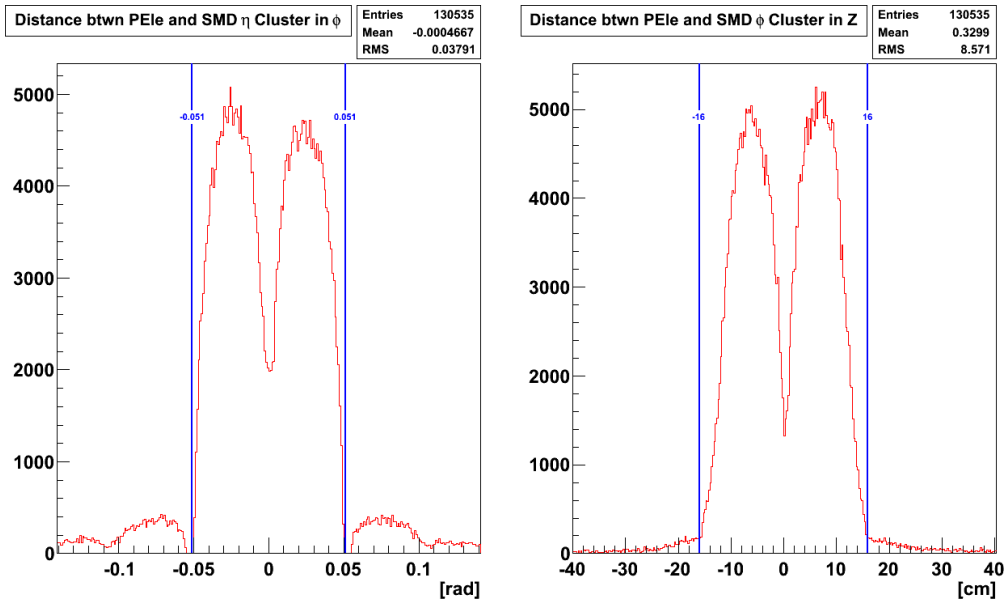

Figure 4.14: Distance between the estimated position of the photonic electron (PEle) on the SMD surface and the center of the nearest SMD cluster for each plain measured in the "wrong direction". The blue lines marks the range of accepted values.

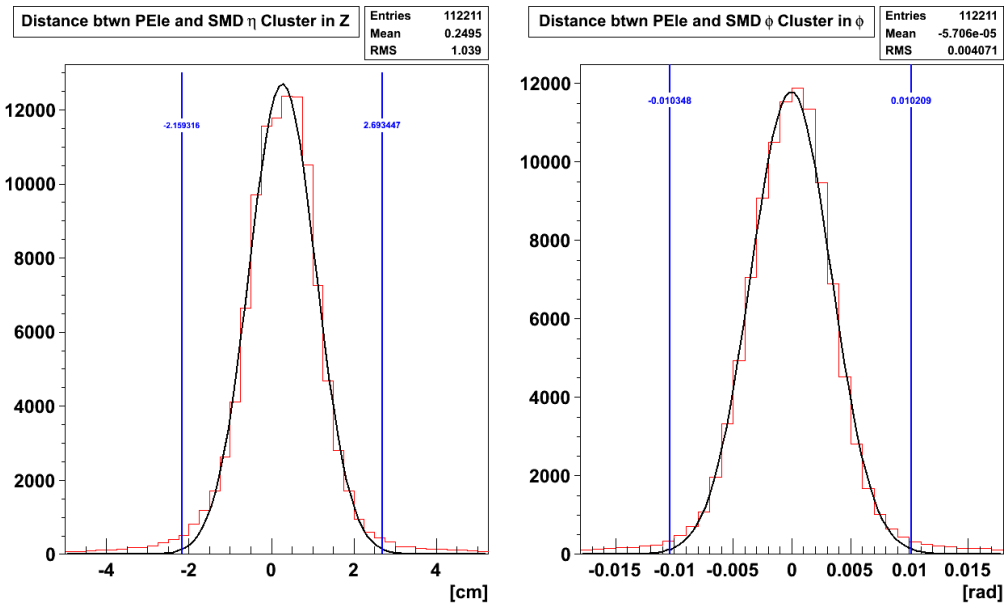

Figure 4.15: Distance between the estimated position of the photonic electron (PEle) on the SMD surface and the center of the nearest SMD cluster for each plain measured in the "right direction". The blue lines marks the range of $\pm 3\sigma$ from the mean of the Gaussian fitted to the data. This range is the cut used in analysis.

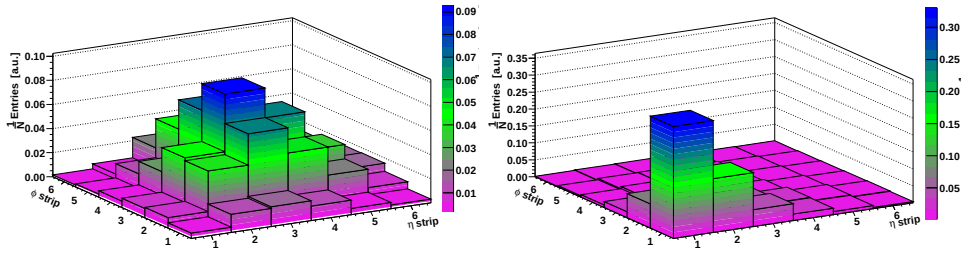

Figure 4.16: Simulation of the shower shape in the SMD produced by electron (left) and hadron (right).

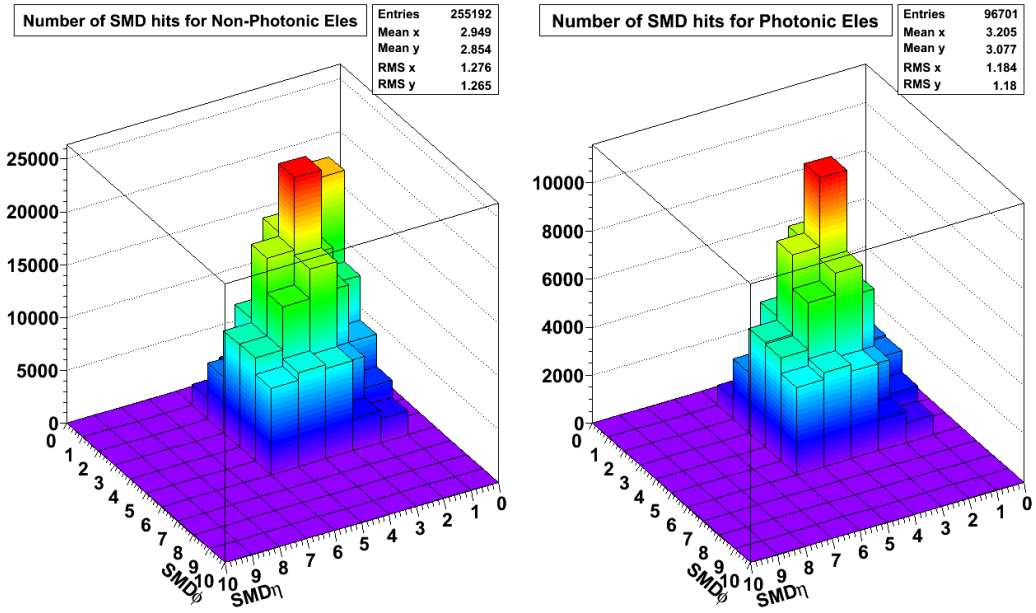

Figure 4.17: Number of activated SMD hits for the electron candidates.

As the BEMC is designed to store most of the electron energy it is expected that the ratio between the energy deposited by those particles to their momentum (p/E) would give a value close to unity while for the hadrons it would go to much higher numbers. This has been supported by the GEANT simulation which has provided the Gaussian shape signal distribution. Base on this study cut for the parameter was defined as $p/E \in (0.0, 2.0)$.

To complete the identification process a cut on ionization losses was applied. This has been set to the standard values used by the experiment in this type of analysis: $\sigma_d E/dx(e) \in (-1.0, 3.0)$. The asymmetric cut around the mean value comes form the fact that while for the stronger ionization there are very few contamination sources, for the weaker there are many hadrons which can affect the final set.

To summarize, track considered onward as an electron had to:

- satisfy all the BEMC matching criteria mentioned previously
- have SMDη hits > 2
- have SMDϕ hits > 2
- have $p/E \in (0.0, 2.0)$
- have $\sigma_{dE/dx}(e) \in (-1.0, 3.0)$

4.3.3 Electron purity

Prior to the dE/dx cut, a purity study has been performed in order to quantify the potential hadron contamination. For that, a distribution of $\sigma_d E/dx(e)$ has been divided into 8 bins, based on the momentum of the electrons. Each bin was then used to fit the Gaussian distributions for different particle species, electrons, pions, kaons, and in first two bins also deuterons. In the first bin one combined distribution was used for both pions and kaons, as they were too close to handle them separately. The mean of every Gaussian was allowed to variate between the values of mean ionization loss calculated from the Bichsel function (ionization loss parametrization used by STAR **??**) for the boundaries of the given momentum bin and the initial number was set to one that corresponds to the center of the bin. The standard deviation for all the particle types was initially set to $\sigma = 1.0$ and the limits were defined in the way that in non of the cases any of the values reached the boundary.

The fitting procedure has been done in steps by:

- fixing standard deviation for electrons at $\sigma = 1.0$
- fitting the distributions
- calculating the average of the mean value from all of the bins
- fitting again only with the mean value fixed to the one obtained in the previous step

- calculating the average of standard deviation from all of the bins
- redoing the procedure from point 2 onwards with the standard deviation fixed on the value from the previous step

This process was repeated until the average values for the mean and for the standard deviation of the electron Gaussians converged to the numbers which were stable from iteration to iteration. The final result of this fit is presented on the fig. 4.19.

Next all of the fitted Gaussians were integrated in the range of the dE/dx cut used for electron identification. The values obtained for hadrons were then subtracted from the one which corresponded to electrons. The result was divided by the sum of those integrals. This was performed for each momentum bin separately and showed that the method of electron identification gives a sample with less then 25% contamination for the particles below $p = 6[GeV/c]$ (fig. 4.18).

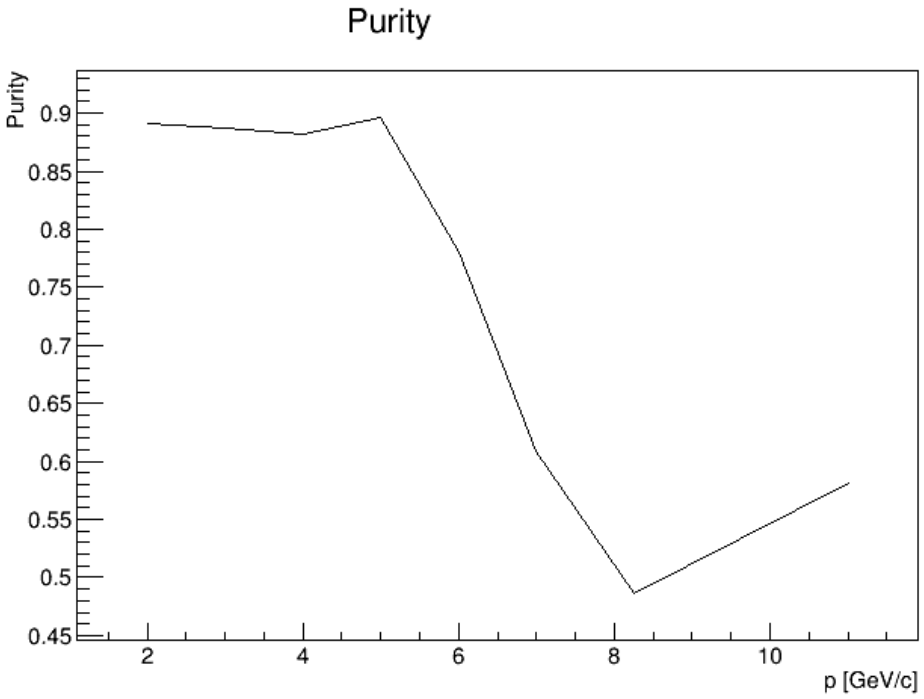

Figure 4.18: Electron purity

4.3.4 Non-photonic electron selection

Apart form the heavy flavor semi-leptonic decay there are two other sources which significantly contribute to the electron spectrum, the scalar meson (mainly π^0) Dalitz decays and the photon conversions:
$\gamma \rightarrow e^+ + e^-$

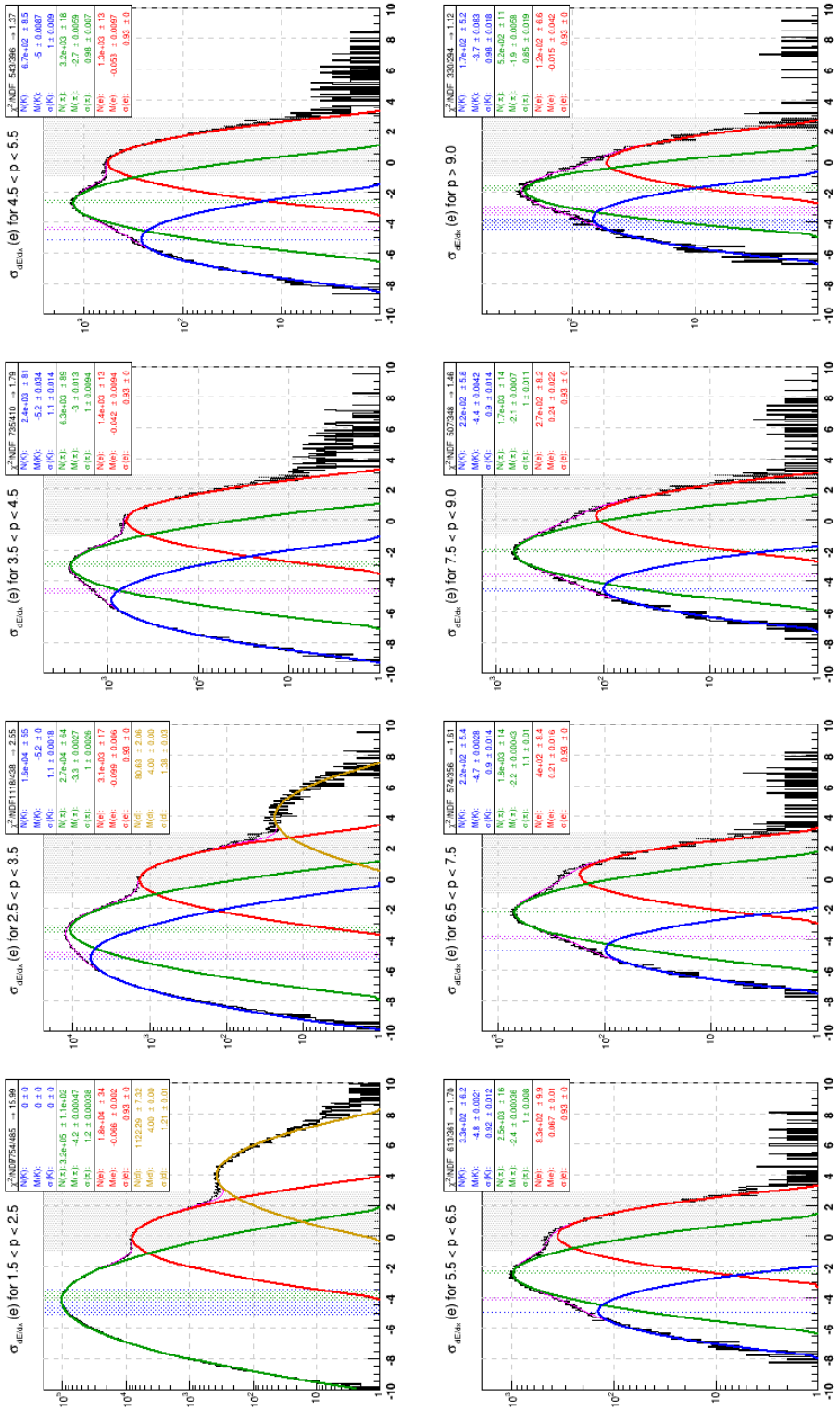

Figure 4.19: Distribution of $\sigma_{dE/dx}(e)$ in the different momentum beans with the Gaussians fitted to each of particle species: blue - protons, green - pions, red - electrons, olive - deuteron. The color bands marks the ranges in which the mean of each Gaussian was allowed to vary during the fit. The gray region is where the electron purity was calculated.

$\pi^0 \rightarrow e^+ + e^- + \gamma$
Those effects form the so called photonic background that had to be suppressed before the further analysis.

Since the γ conversions can happen anywhere in the detector, some part of the electrons originated from this process were already rejected during the initial track selection, when the demand on existence of the corresponding primary track had been applied. The rest had to be recognized through the particle correlation techniques. In order to do that, each of the electrons was paired with all other global tracks that passed the quality cuts and for which the ionization loss was within $\sigma_d E/dx(e) \in (-3.0, 3.0)$. Next the study on the geometry of the potential decay was carried out. This subject has been covered in detail in the section 4.2.2, here the cuts were limited to [Sak10]:

- DCA between tracks < 1.0 [cm]
- opening angle < 0.15 [rad]
- opening angle in $\phi < 0.1$ [rad]
- opening angle in $\theta < 0.05$ [rad]

The momentum calculated at the point of closest approach was then used to compute the invariant mass for every pair. As this work used electrons with momentum significantly higher than their masses, the paths formed by the tracks in the detector could be considered as tangential. However, due to limited resolution of the TPC the reconstructed helices were usually shifted towards or away of each other. While the second case still provided correct results on the geometry study the first one caused an error, as the point of closest approach was calculated as one of the crossing point of two curves. This was affecting the obtained momentum value, which can be seen on the invariant mass plot as a broadening of the photon peak (fig. 4.20 left). This effect can be eliminated by rotating the momenta of the tracks to the same ϕ. The mass calculated in that situation (2D invariant mass) didn't exhibit that kind of broadening (fig. 4.20 right) [Don06].

This method identifies only those of the photonic electrons, for which a partner track was properly registered by the detector.

Regardless of the type the events with at least one electron were stored for the further analysis.

4.4 Angular correlations

To separate the beauty and charm contributions to the D mesons spectra the azimutal angular ($\Delta\phi$) correlations between the non-photonic electron and the reconstructed particle was performed for both D^0 and D^*. The $\Delta\phi$ distribution was divided into two regions interesting for further study: $|\Delta\phi| < 1.2[rad]$, so called near side correlation, and $|\pi - \Delta\phi| < 1.2[rad]$, the away side correlation. In addition, a division was made based on the charge of the electron and the kaon from

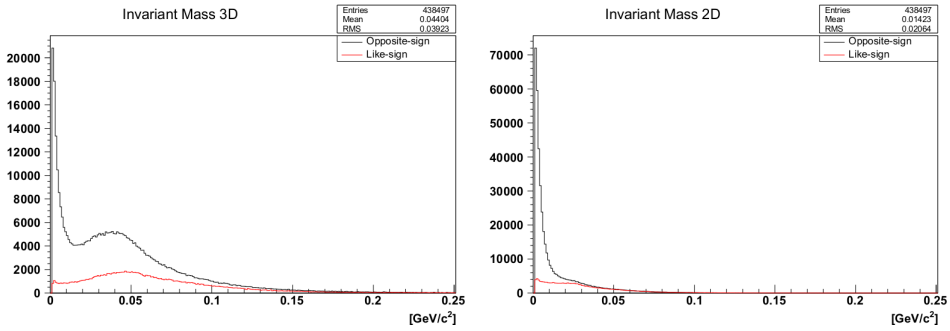

Figure 4.20: Invariant Mass distribution of electron pairs with opposite sign (black) and like-sign (red). The left picture shows the standard M_{inv} while the right two dimensional version.

the D^0 candidate. Cases where the sign of those particles differed were considered separately form the like-sign correlations. Finally this led to 4 possible options:

- like-sign - near side $\rightarrow$ charm mesons that comes from beauty semi-leptonic decay, called onwards the b case;
- like-sign - away-side $\rightarrow$ mesons formed form prompt charm with a small contribution form beauty, the c dominant case;
- opposite-sign - near side $\rightarrow$ not suppose to give signal, the non-applicable (n/a) case;
- opposite-sign - away side $\rightarrow$ charm from the beauty decay with some char contribution, the b dominant case;

Chapter 5

Results

Contents

5.1 Gold-gold collisions at 200 GeV 45
5.2 Proton-proton collisions at 500 GeV 48
5.2.1 Overall charm production in the high tower dataset 48
5.2.2 Measurement of high-p_T D* in the hadron-triggered events . 55
5.2.3 Charm production in electron-triggered events 68
5.2.4 Electron-D azimuthal angular correlations 70

The bottom and charm contributions to the non-photonic electron spectra has been up till now measured by STAR only in the p+p system at the energy of $\sqrt{s} = 200\text{GeV/c}$. However, to understand the R_{AA} of the non-photonic electrons, the same study had to be perform for the heavy ion collisions. For that reason this work concentrated mainly on the analysis of $e - D^0$ and $e - D^*$ correlations in the Au+Au interaction at $\sqrt{s_{NN}} = 200\text{GeV/c}$. In addition such a study was performed for the p+p at $\sqrt{s} = 500\text{GeV/c}$. This system was also used to perform the analysis of inclusive spectra of D^*.

5.1 Gold-gold collisions at 200 GeV

Initially the study of the Au+Au collisions was performed on the events collected in 2007, while the old vertex detector, Silicon Vertex Tracker (SVT), was still installed in STAR. However, due to the poor statistics available for the analysis (1.5M high-tower events), this results were disregarded. The data collected in the year 2010 (59.5 M events) and 2011 (94.3 M events), without the silicon detector, was used instead. As the detector setup was the same in both years, those dataset were combined in order to increase the available statistics.

Apart from the cuts on daughter tracks of the D meson candidates another criteria was used as a possible to reduce the background in the D^0 mass region, the cut on $\cos(\theta^*_K)$. This is the angle between the momentum of a kaon measured in the rest frame of the D^0 candidate and the path that of the parent particle. The goal of this cut was to remove the cases when the kaon is emitted in the direction opposite to the direction of the D meson. Such particles have lower reconstruction efficiency.

As shown on the fig. 5.1-5.3, the currently available statistics and the detector resolution didn't allow to detect any charm mesons. Starting from the year 2014

the new vertex detector (Heavy Flavor Tracker - HFT) will be operating as a part of STAR system. It will provide a resolution sufficient, to measure the open charm production in the Au+Au collision at the high p_T, and to separate the charm and bottom production directly, without a need for e-D angular correlations.

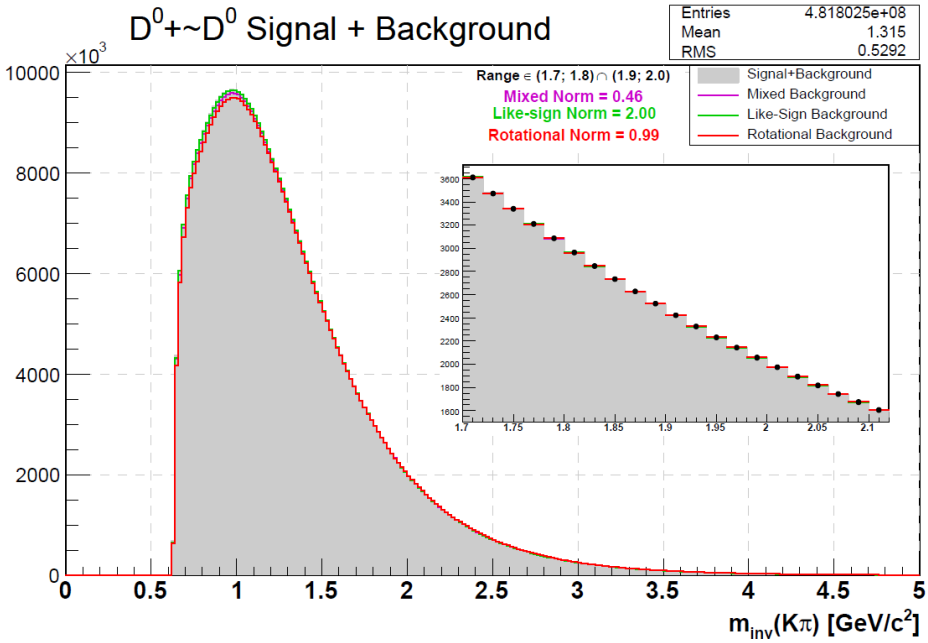

Figure 5.1: The invariant mass distribution of $M_{inv}(K\pi)$ with a zoomed in region of D^0 for the analysis performed on the Au+Au collisions at 200 GeV/c. The combined statistics from data collected in 2010 and 2011 were used.

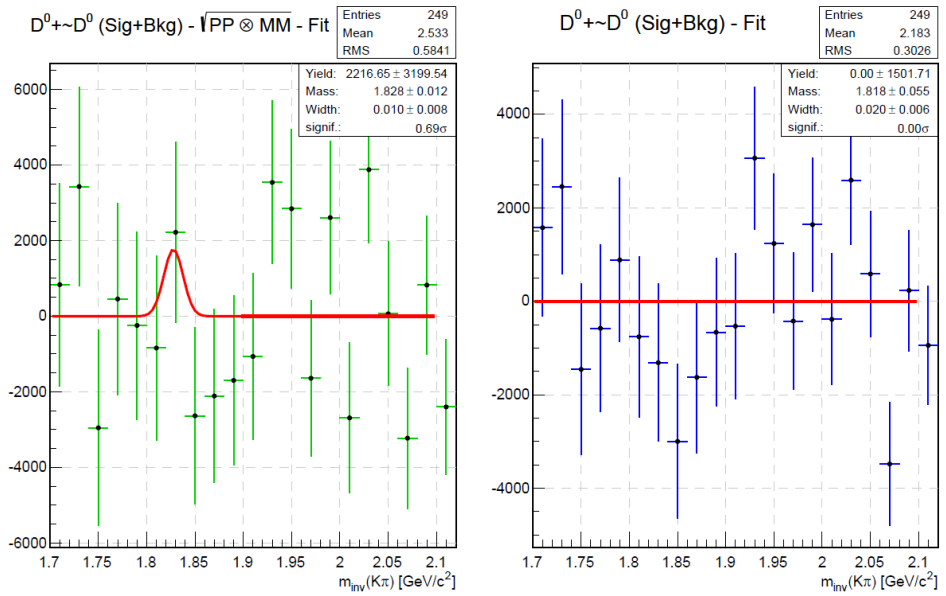

Figure 5.2: The invariant mass distribution of $M_{inv}(K\pi)$ in the D^0 region after the subtraction of like-sign background (left) and directly fitted polynomial (right) for the analysis performed on the Au+Au collisions at 200 GeV/c. The combined statistics from data collected in 2010 and 2011 were used.

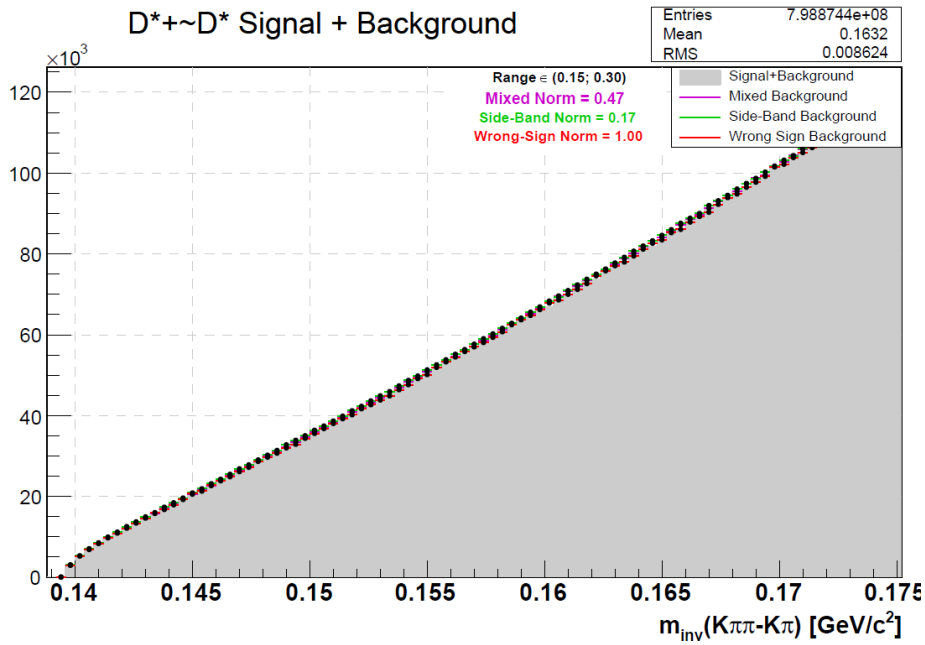

Figure 5.3: The invariant mass distribution of $M_{inv}(K\pi\pi) - M_{inv}(K\pi)$ for the analysis performed on the Au+Au collisions at 200 GeV/c. The combined statistics from data collected in 2010 and 2011 were used.

5.2 Proton-proton collisions at 500 GeV

The high-tower dataset in pp has been analyzed in three different ways. First all the accepted events were used to estimate the amount of charm mesons available for the analysis, later the same procedure was repeated for the events triggered by the particles which could possibly originate from the charm decay, finally the study was cared out on the events triggered by electron, in this case charm particles production was measured also in the correlation with the electrons.

5.2.1 Overall charm production in the high tower dataset

This study was performed to estimate the amount of charm particles (D^0 and D^*) available for analysis in the high tower dataset. It used the events preselected in the same way as those for the e-D correlations, except the demand for a high-tower electron which fired the trigger to be present in every collision. Thus the input statistic available for this analysis was 39 M events. The analysis was performed for three different $\cos(\theta^*_K)$, cuts, $\cos(\theta^*_K) < 0.85$ (fig. 5.4 5.5), $\cos(\theta^*_K) < 0.77$ (fig. 5.6 5.7) and $\cos(\theta^*_K) < 0.6$ (fig. 5.8, 5.9). As can be seen the yields are greatest for the case with the most open cut, $\cos(\theta^*_K) < 0.85$, however the significance grows with more strict cuts. This happens most probably due to the fact that the cut removes contribution from jet particles.

In order to calculate the spectrum of charm particles this result would require a measurement of trigger bias. Such analysis were not covered by this work.

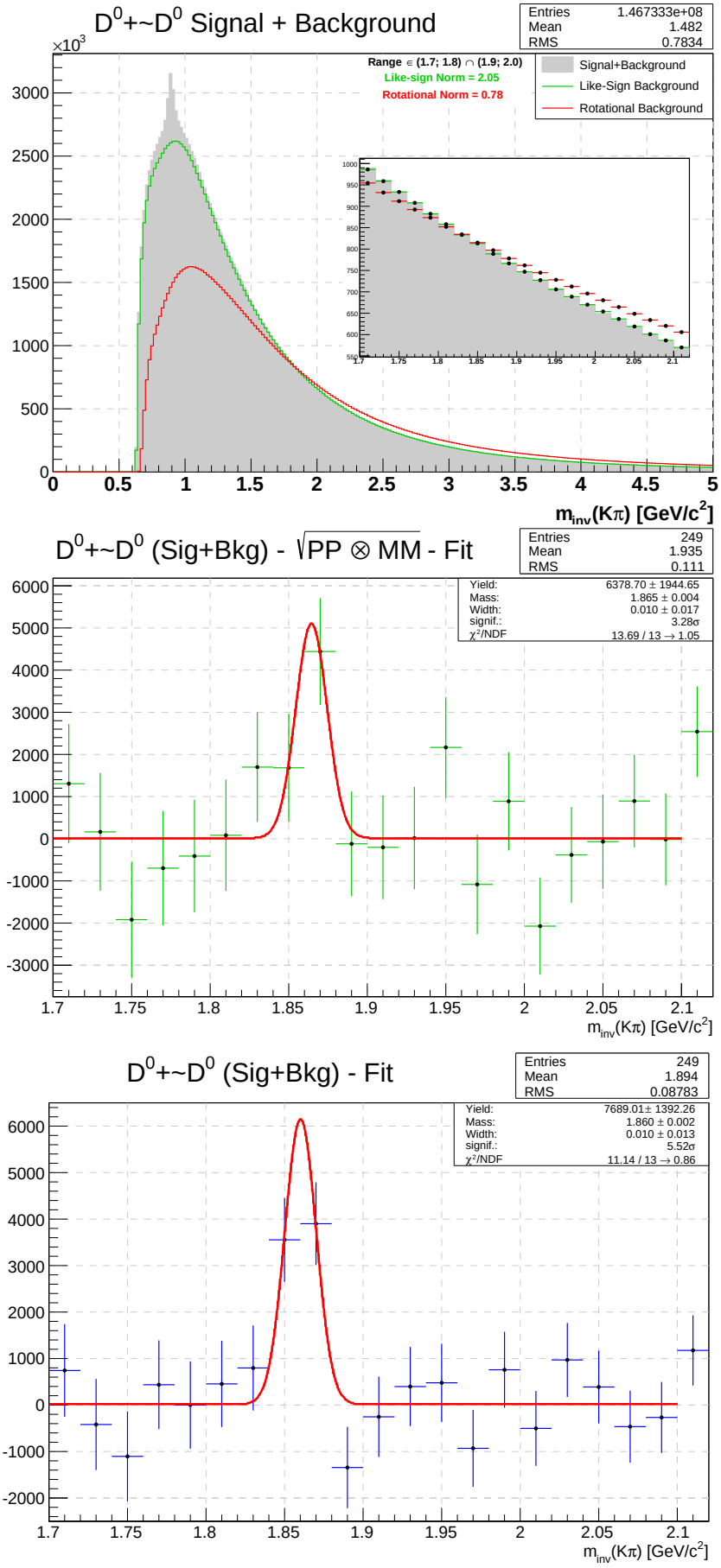

Figure 5.4: D^0 results for all events for $\cos(\theta^*_K) < 0.85$

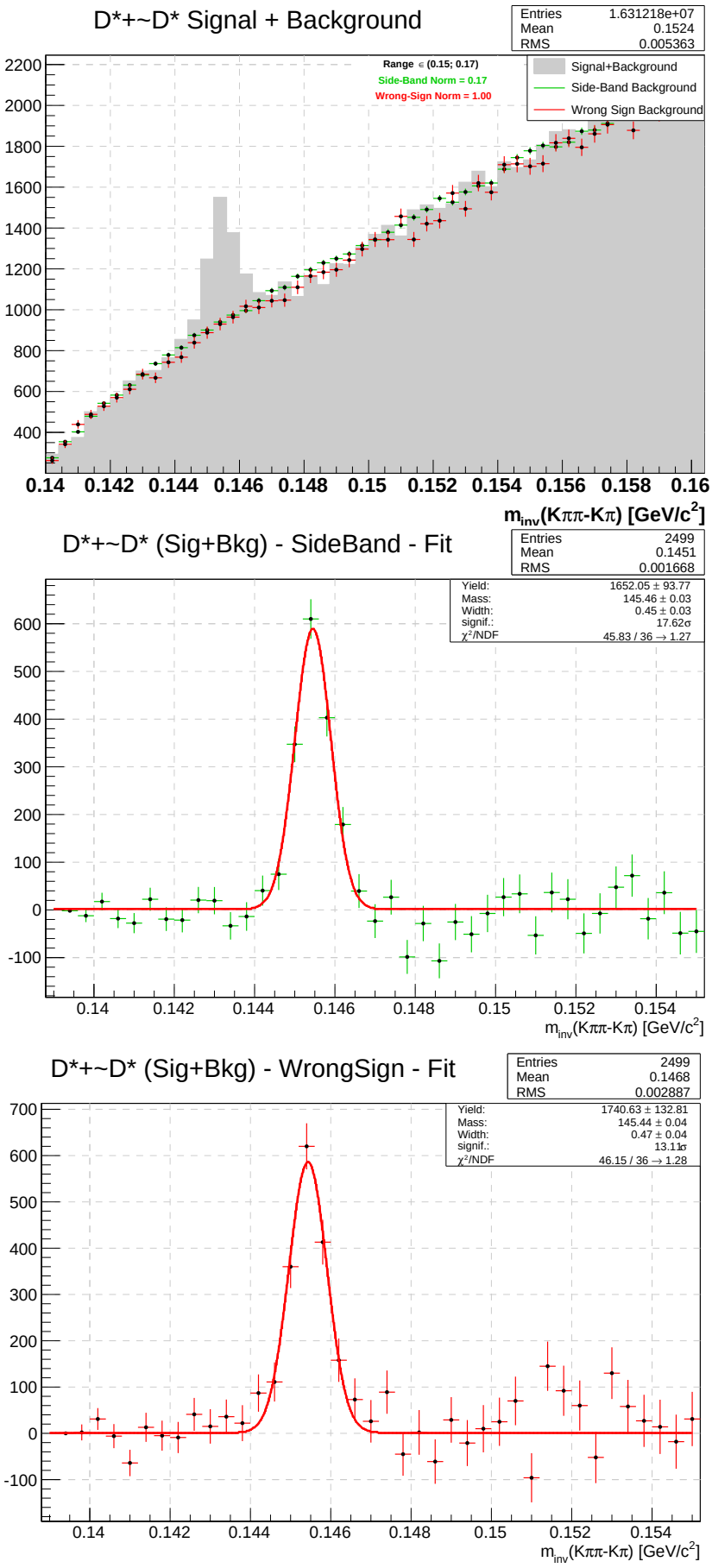

Figure 5.5: D* results for all events for $\cos(\theta^*_K) < 0.85$

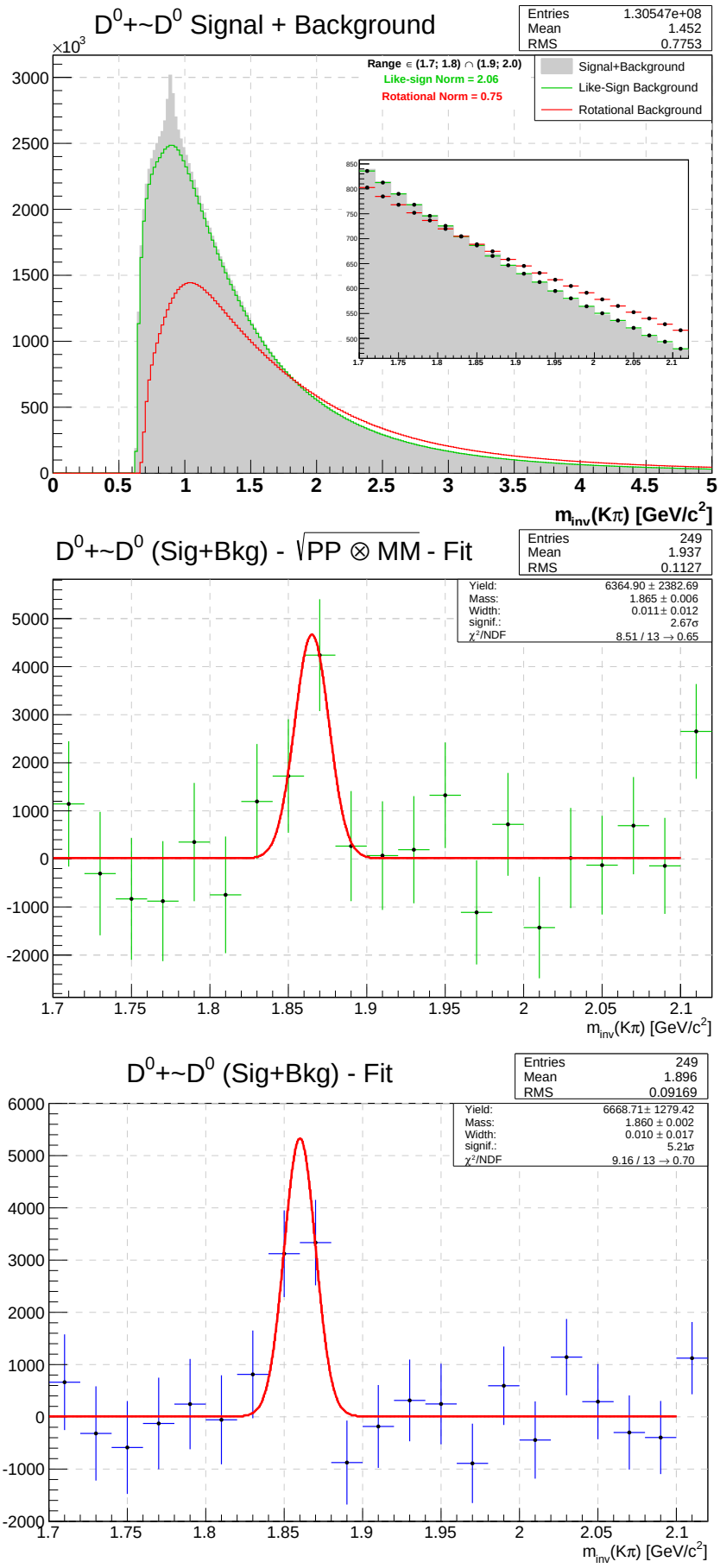

Figure 5.6: D^0 results for all events for $\cos(\theta^*_K) < 0.77$

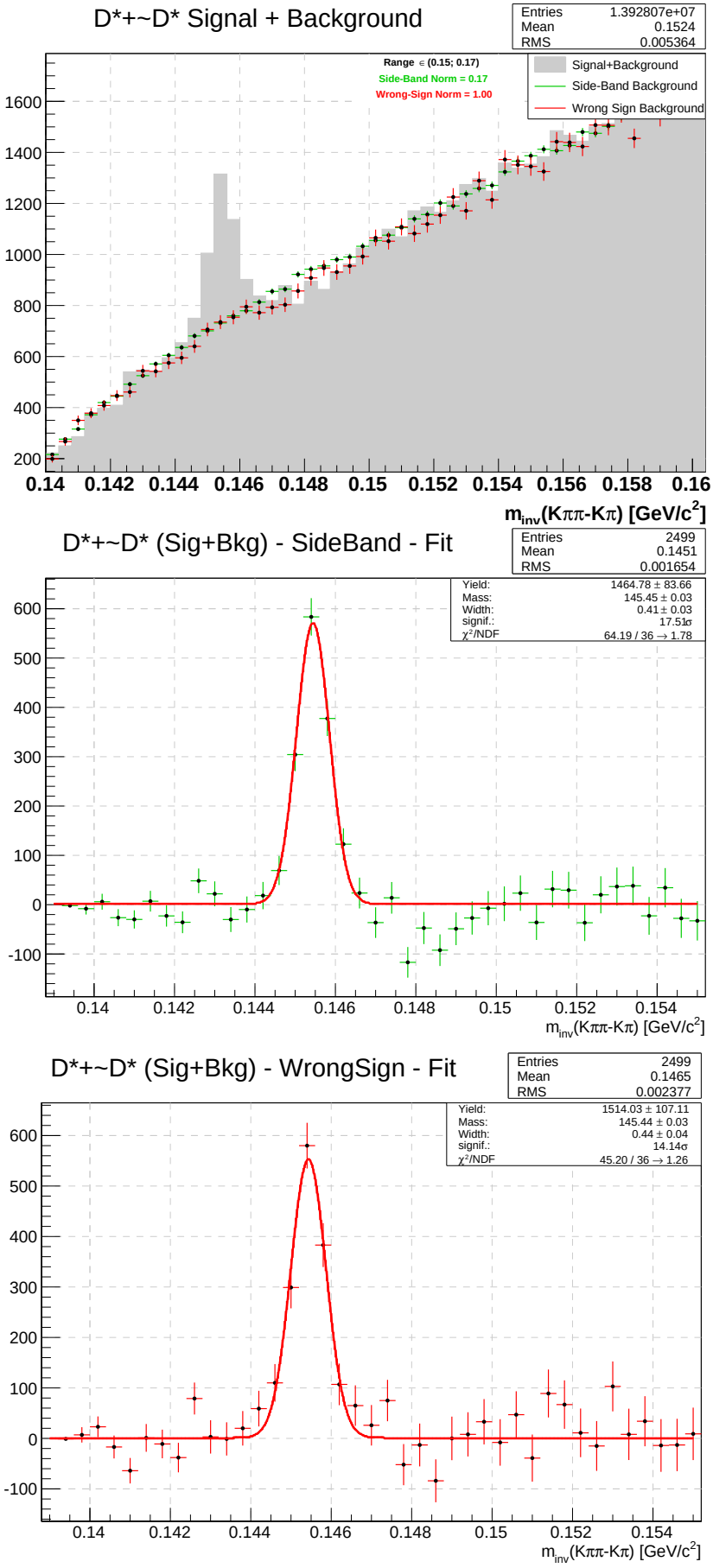

Figure 5.7: D* results for all events for $\cos(\theta^*_K) < 0.77$

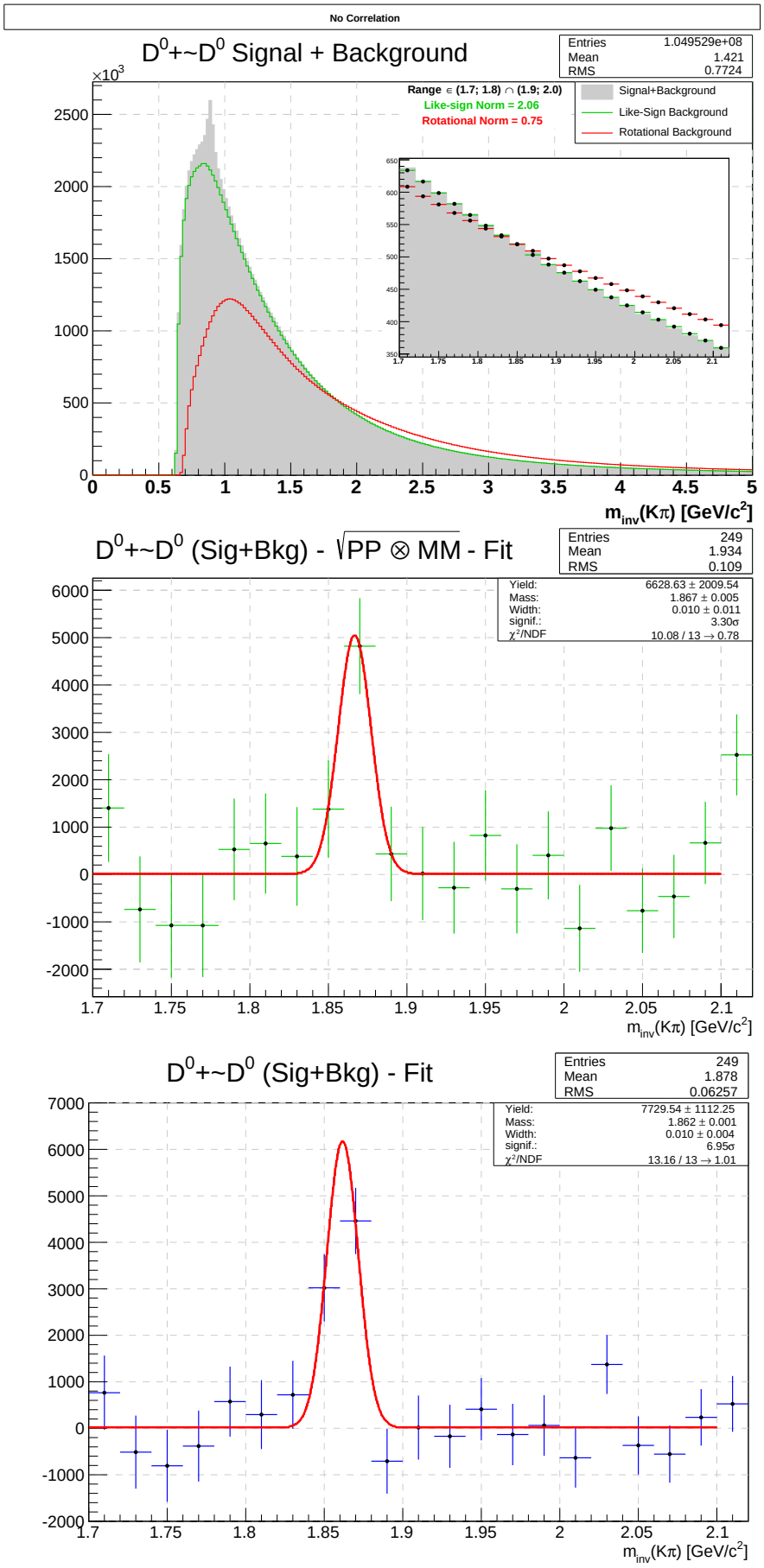

Figure 5.8: D^0 results for all events for $\cos(\theta^*_K) < 0.6$

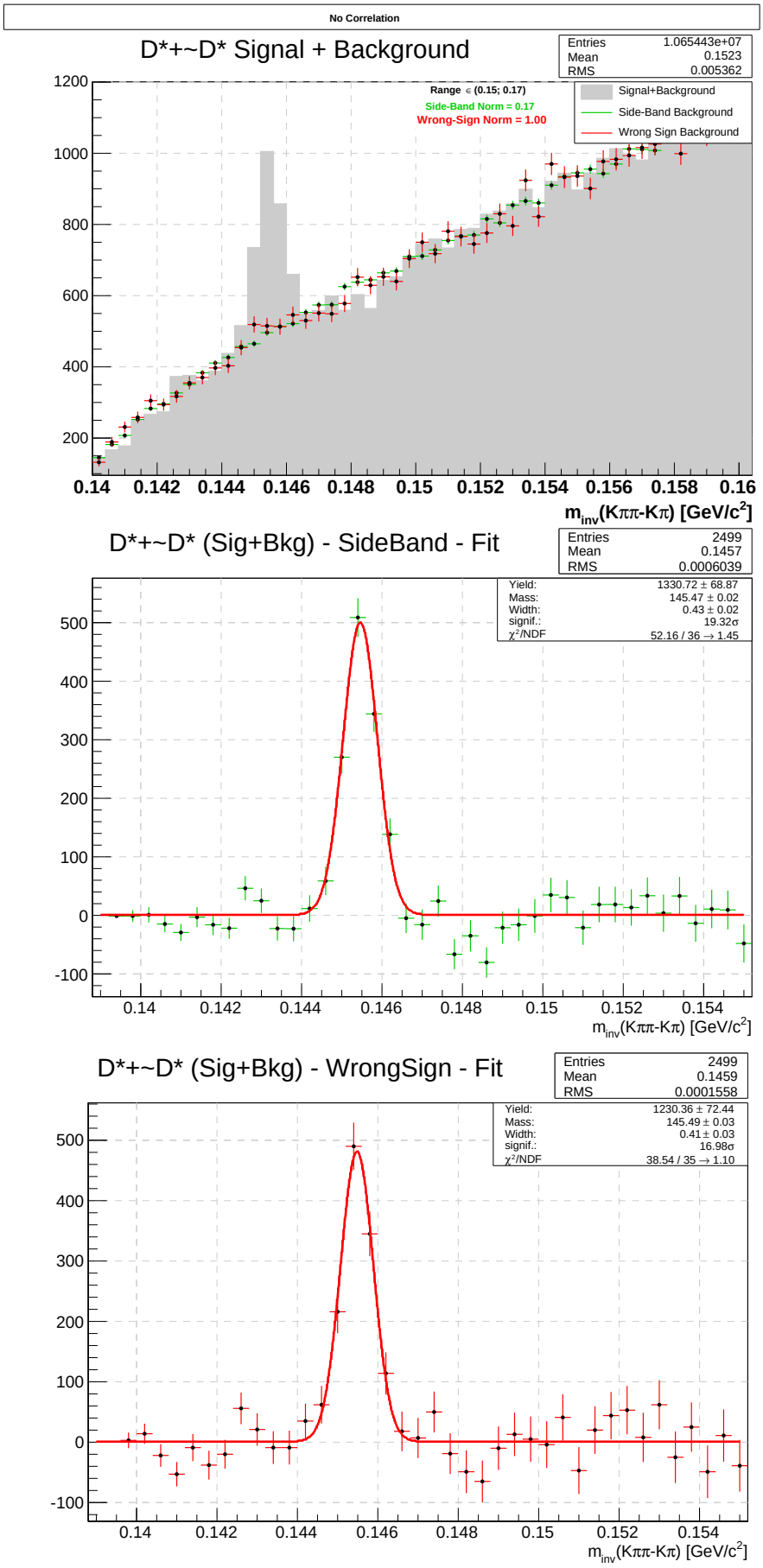

Figure 5.9: D* results for all events for $\cos(\theta^*_K) < 0.6$

5.2.2 Measurement of high-p_T D* in the hadron-triggered events

As shown in [Xu09] it is possible to estimate the trigger bias on K^0_s spectra in the high-tower dataset. In order to do this the particle mass has to be reconstructed with an assumption that at least one of the daughter tracks has fired the high-tower trigger. This approach was taken to extend the measurement of D* spectrum towards higher transverse momentum. The research was done in the collaboration with David Tlusty from Technical University of Prague, Czech Republic.

For this analysis the HT data was reanalyzed without the demand on SMD to be present in every event. This has boosted the statistics up to the 51 M events. Later, to select the D mesons masses were reconstructed from the Kπ pairs and K$\pi\pi$ trinities in which at least one of the tracks has matched to the BEMC tower which fired the trigger. As it is possible that the hadron can hit the tower activated by other particle, like electron or photon, it was necessary to apply an additional cut on the energy and track momentum. That cases were rejected by accepting only triggering tracks which had the energy greater than the doubled transverse momentum value of the given track, $E/p > 2$. The relation between the momentum of the track and the energy of the tower that it matches to is presented on the fig. 5.10, the black line represents the described cut.

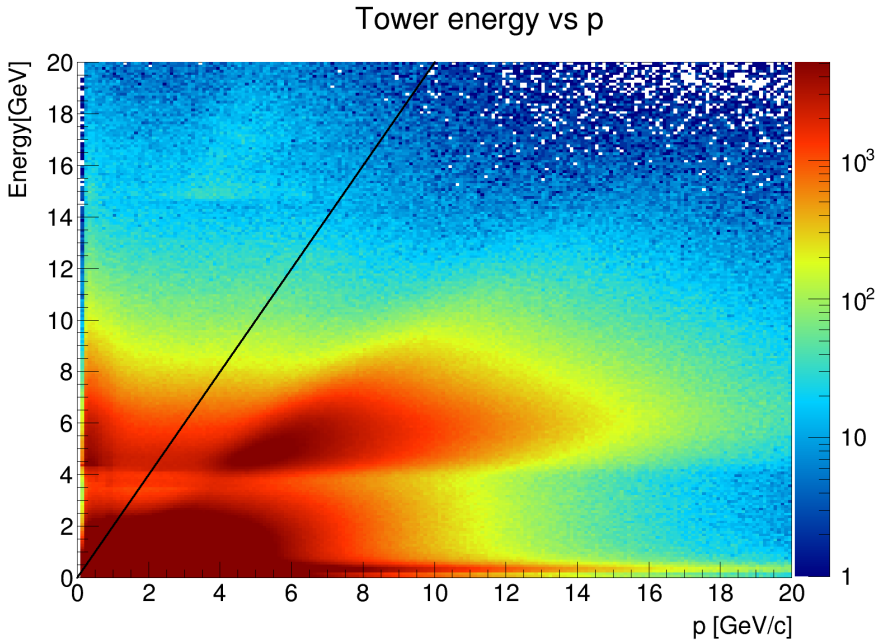

Figure 5.10: The energy of the tower associated with the track versus its momentum for all the particles in high tower dataset from p+p collision at 500 GeV. The black line marks the cut on $E/p > 2$.

For such pairs the D^0 and D^* signals were calculated in the same way as in the other analysis. The available statistics were not sufficient to measure the production

of D^0. However, as can be seen on the fig. 5.11, the obtained D^* signal was strong which allowed to perform a study in transverse momentum bins. The available statistics provided a good signal in the wide range of p_T up to $p_T = 20$ GeV/c (fig. 5.12 - 5.19). The signal parameters are stable on the bin by bin bases (fig. 5.20 and 5.21).

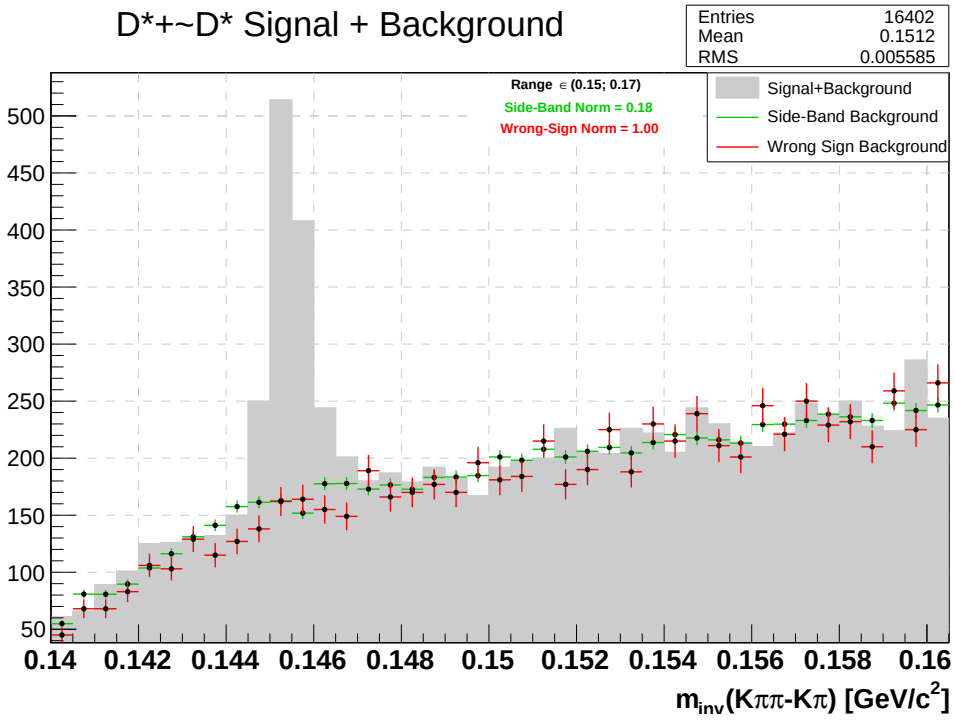

Figure 5.11: Invariant mass distribution for the D^* for the hadron triggered events in the p+p colisions at 500 GeV/c.

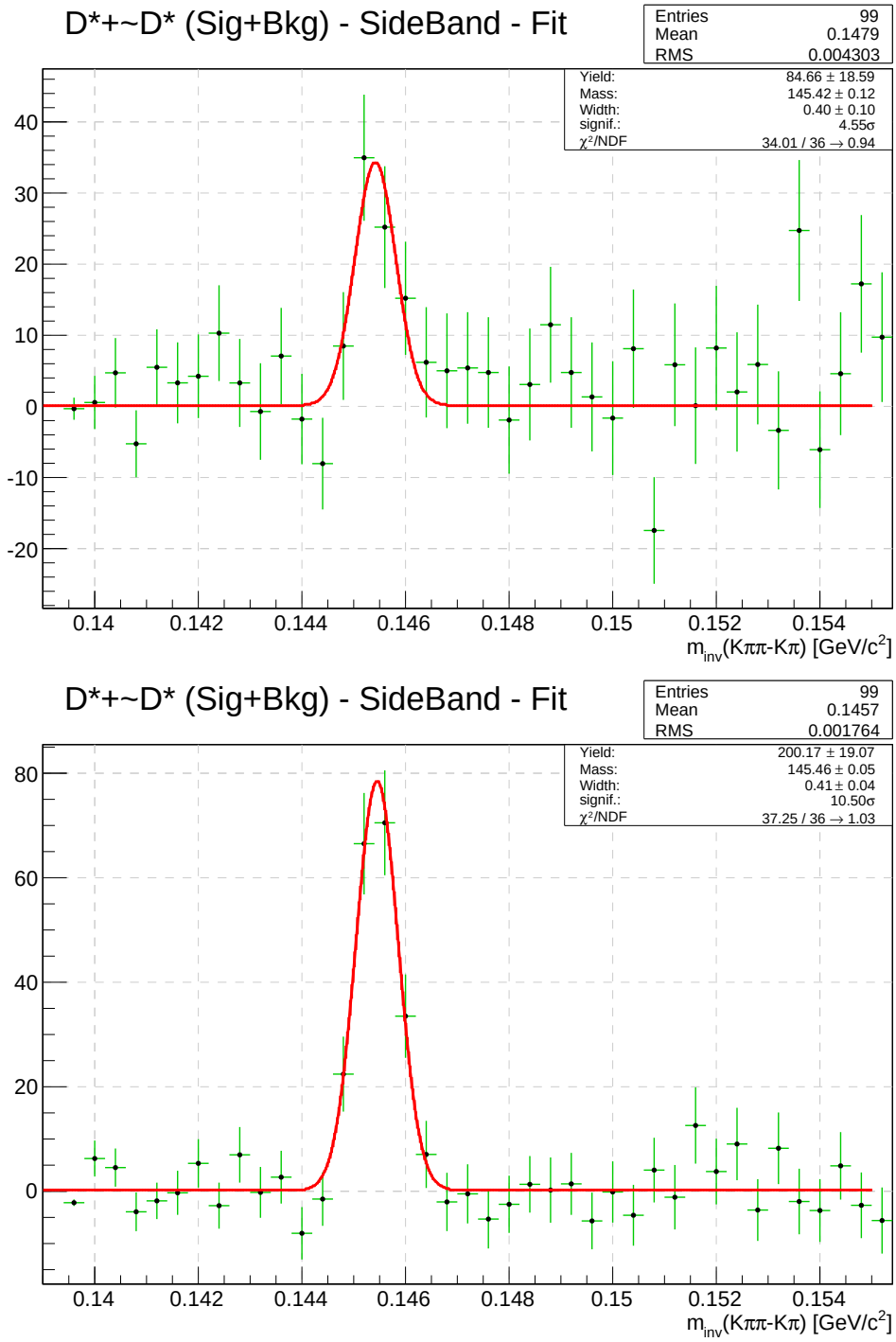

Figure 5.12: D* signal after side-band background subtraction in p_T bins: 4-6 (top) and 6-8 (bottom) GeV/c for the hadron triggered events in the p+p collisions at 500 GeV/c.

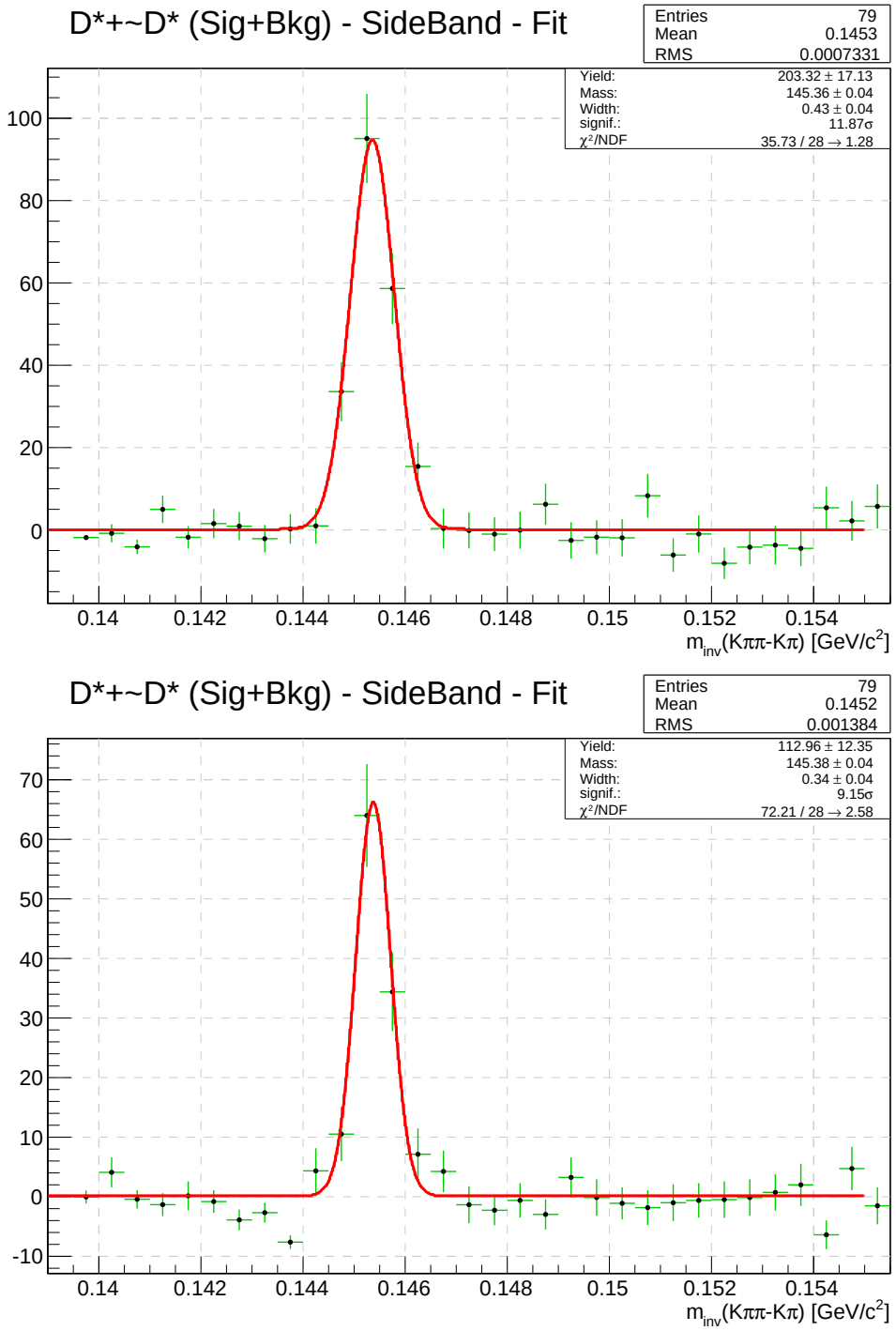

Figure 5.13: D* signal after side-band background subtraction in p_T bins: 8-10 (top) and 10-12 (bottom) GeV/c for the hadron triggered events in the p+p collisions at 500 GeV/c.

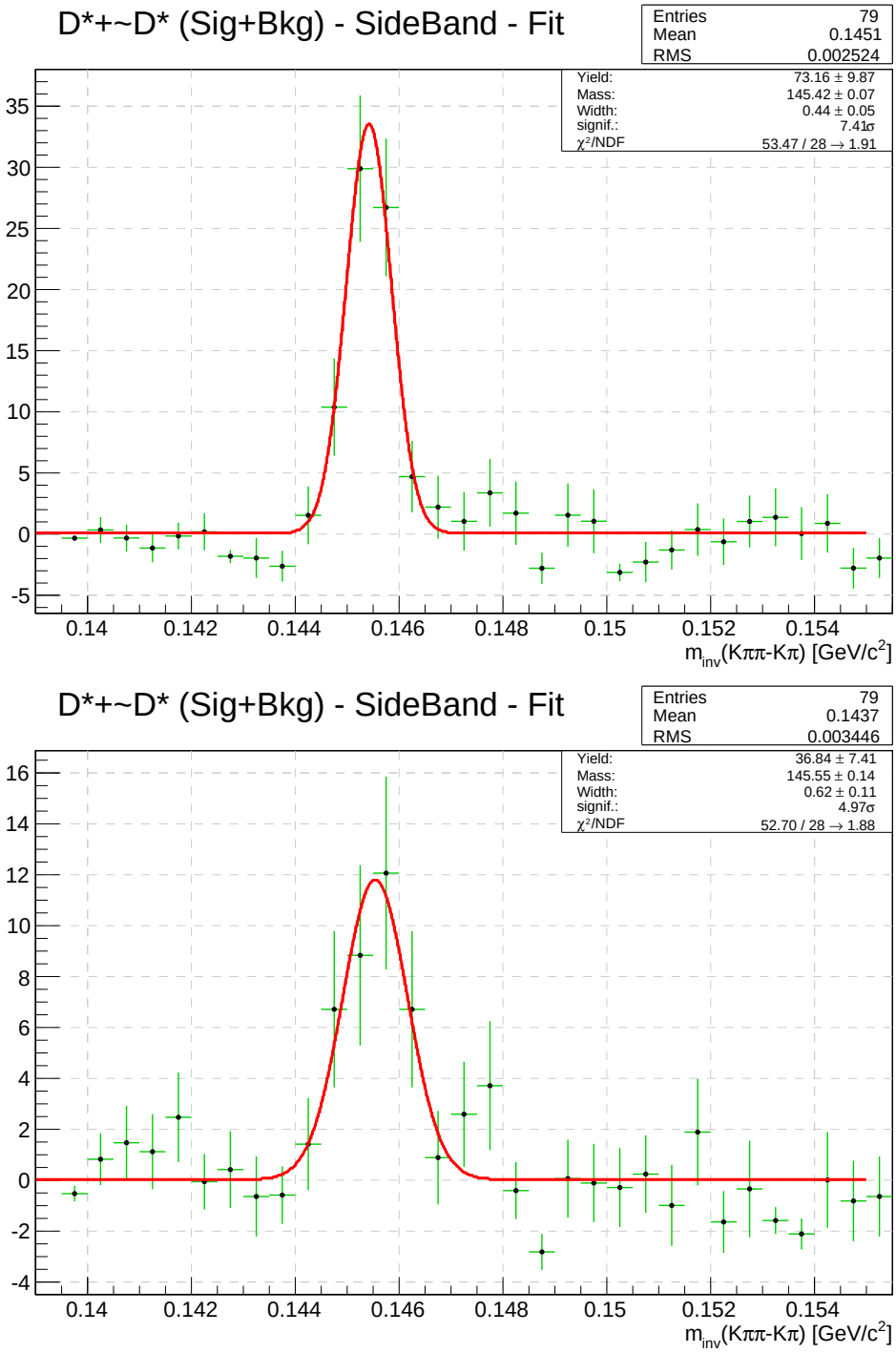

Figure 5.14: D* signal after side-band background subtraction in p_T bins: 12-14 (top) and 14-16 (bottom) GeV/c for the hadron triggered events in the p+p collisions at 500 GeV/c.

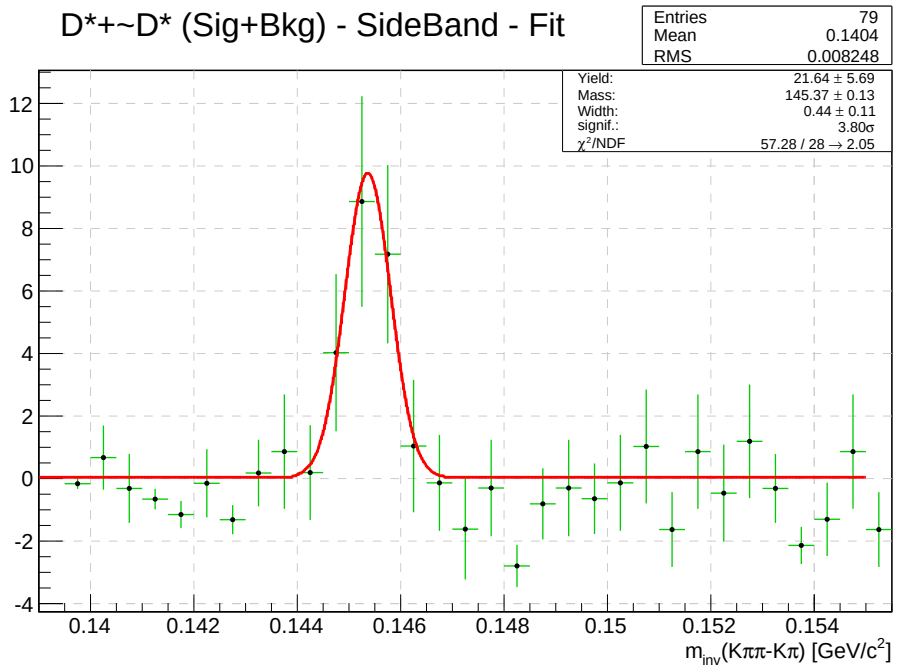

Figure 5.15: D* signal after side-band background subtraction in 16-20 GeV/c p_T bin for the hadron triggered events in the p+p collisions at 500 GeV/c.

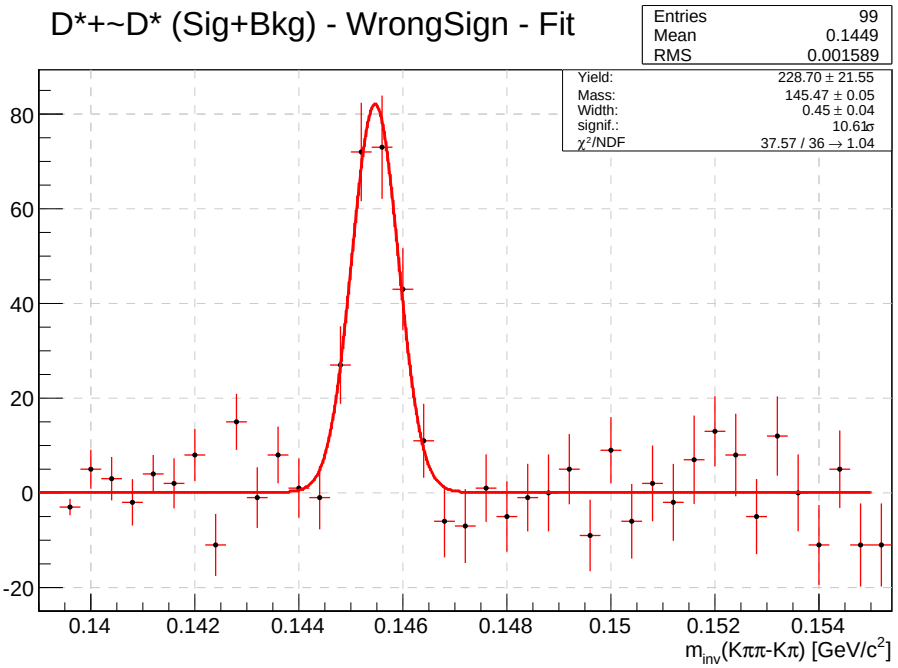

Figure 5.16: D* signal after wrong-sign background subtraction in 6-8 GeV/c p_T bin for the hadron triggered events in the p+p collisions at 500 GeV/c.

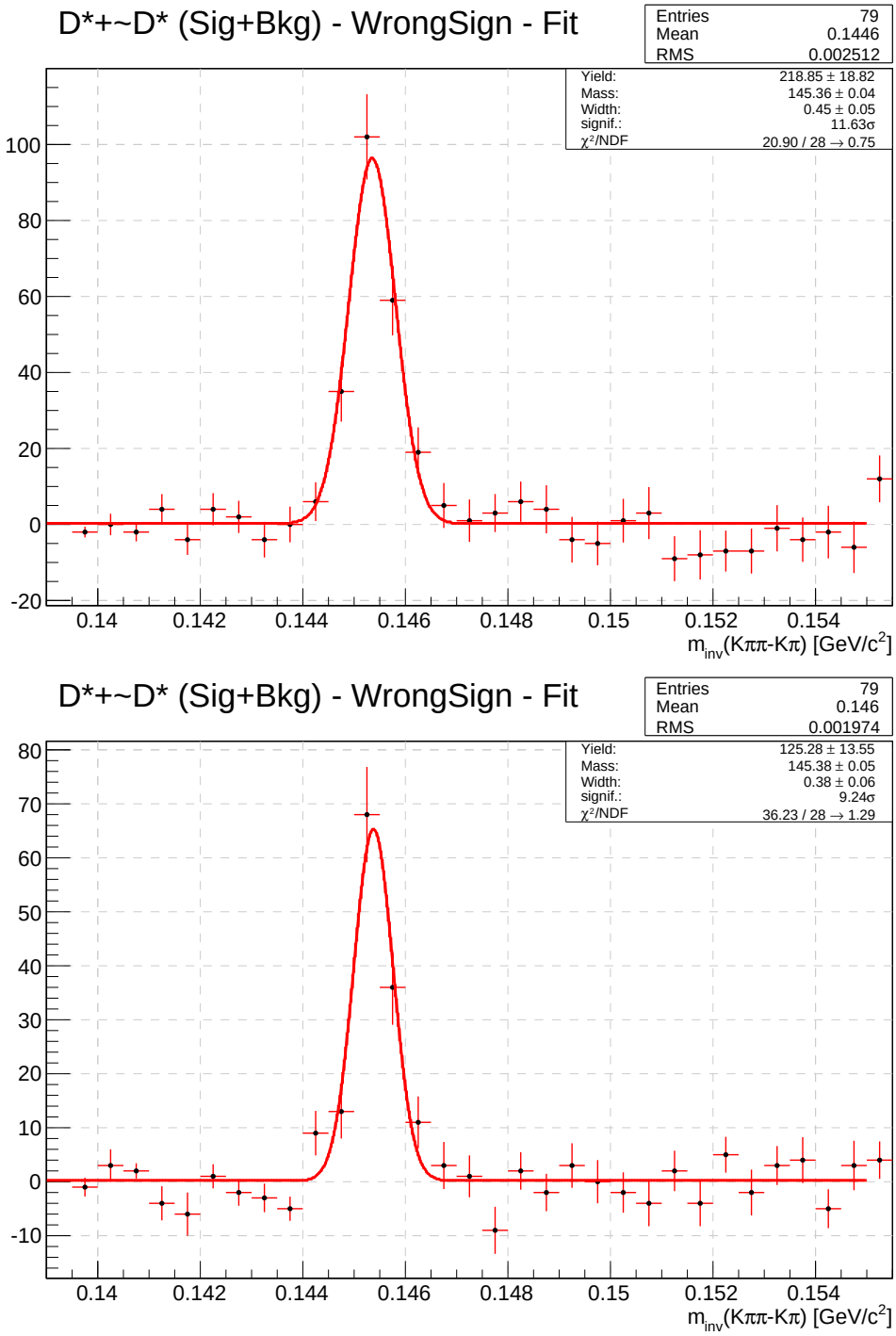

Figure 5.17: D* signal after wrong-sign background subtraction in p_T bins: 8-10 (top) and 10-12 (bottom) GeV/c for the hadron triggered events in the p+p collisions at 500 GeV/c.

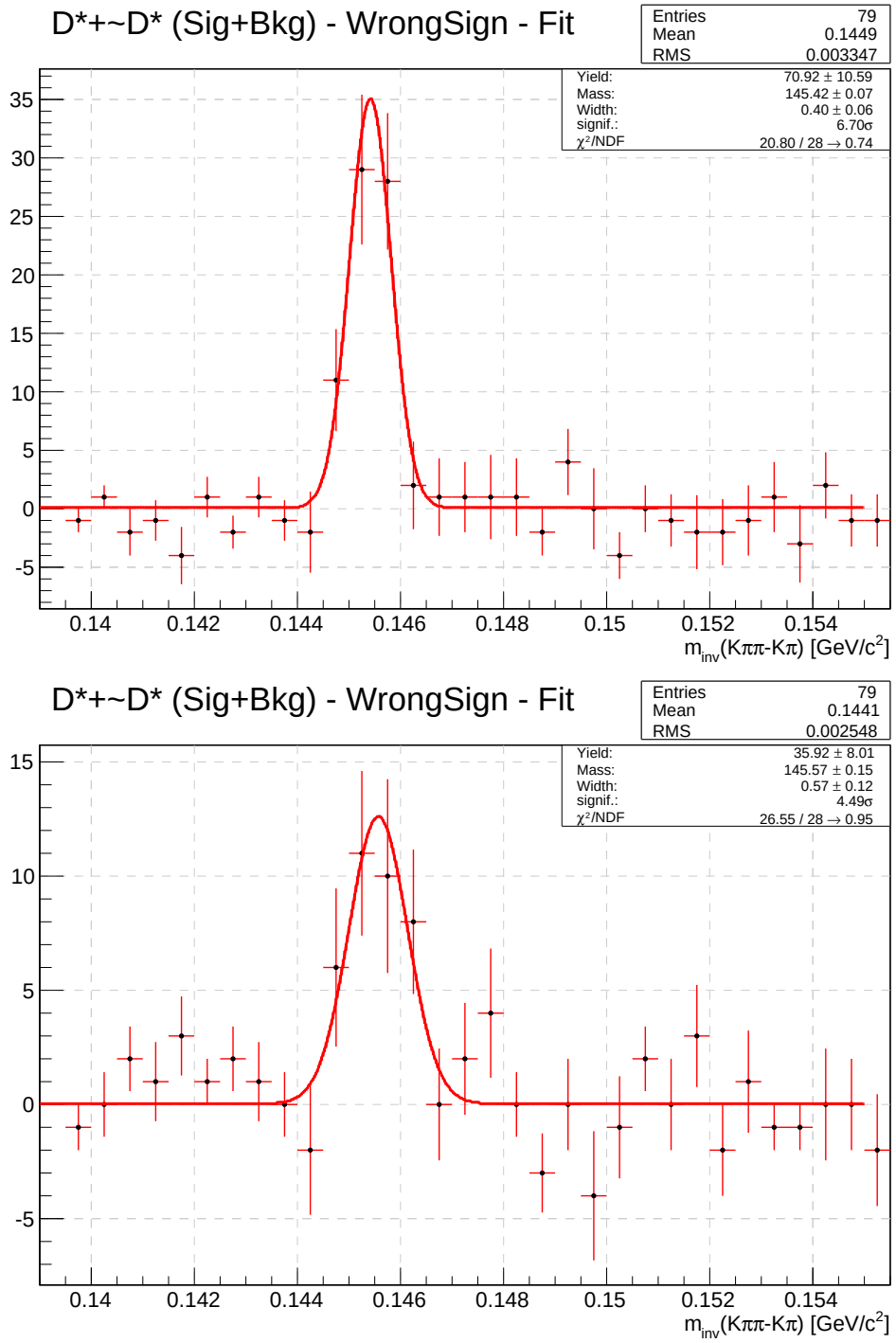

Figure 5.18: D* signal after wrong-sign background subtraction in p_T bins: 12-14 (top) and 14-16 (bottom) GeV/c for the hadron triggered events in the p+p collisions at 500 GeV/c.

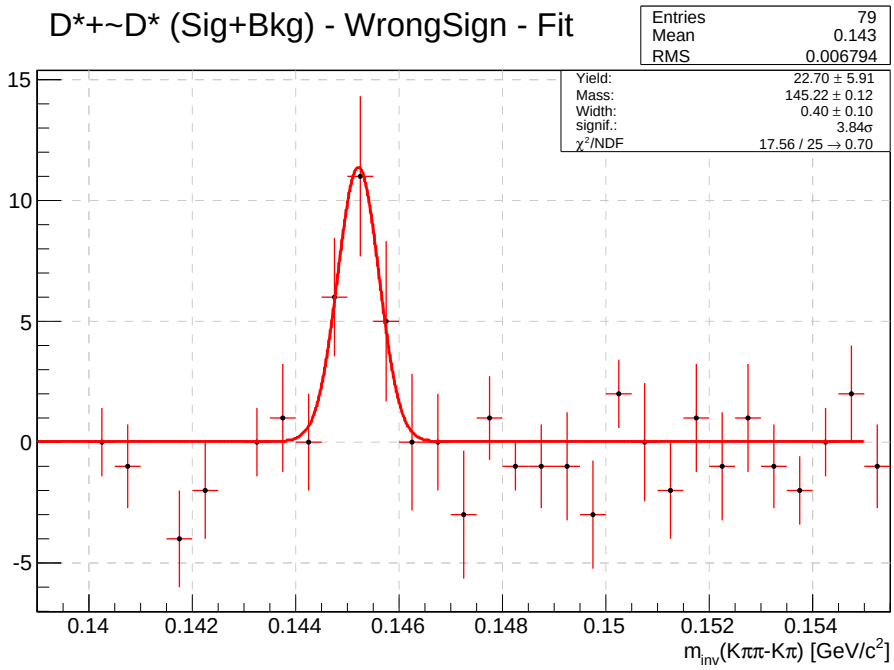

Figure 5.19: D* signal after wrong-sign background subtraction in 16-20 GeV/c p_T bin GeV/c for the hadron triggered events in the p+p collisions at 500 GeV/c.

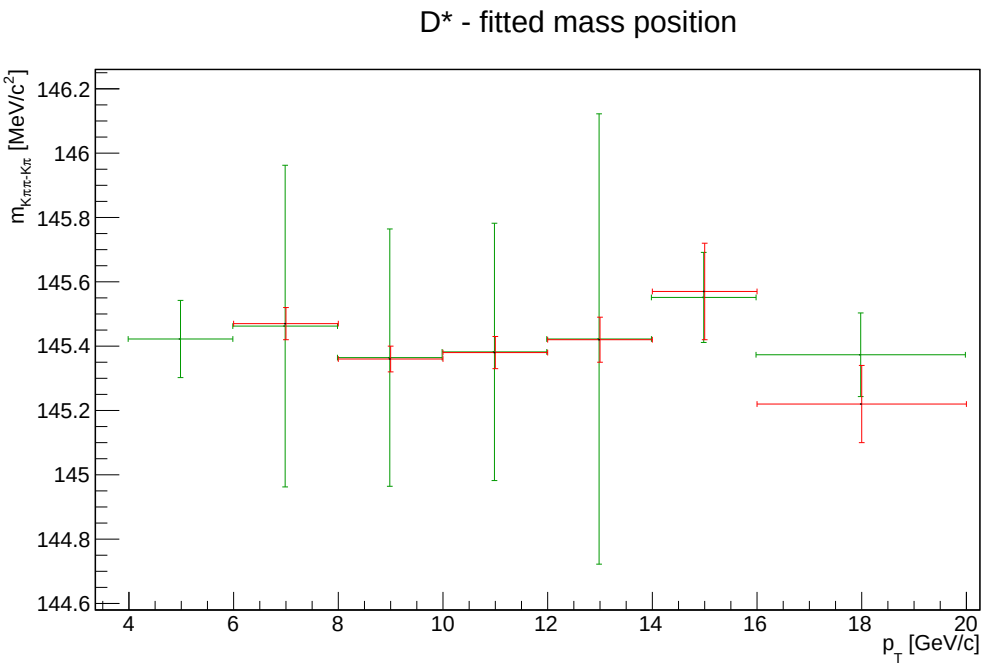

Figure 5.20: D* peak position in the function of p_T for the hadron triggered events in the p+p collisions at 500 GeV/c.

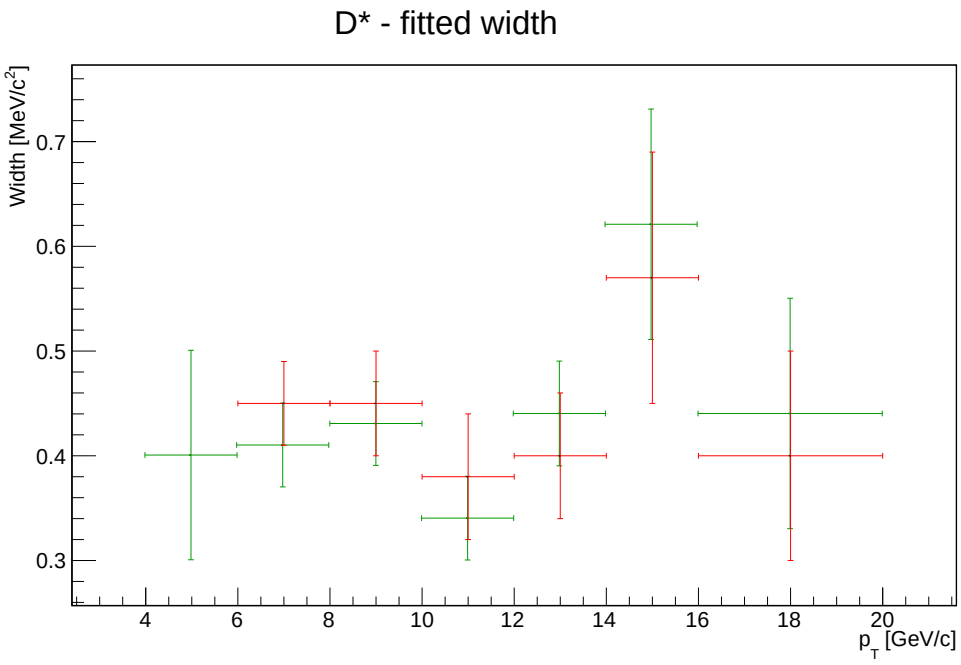

Figure 5.21: D* width in the function of p_T for the hadron triggered events in the p+p collisions at 500 GeV/c.

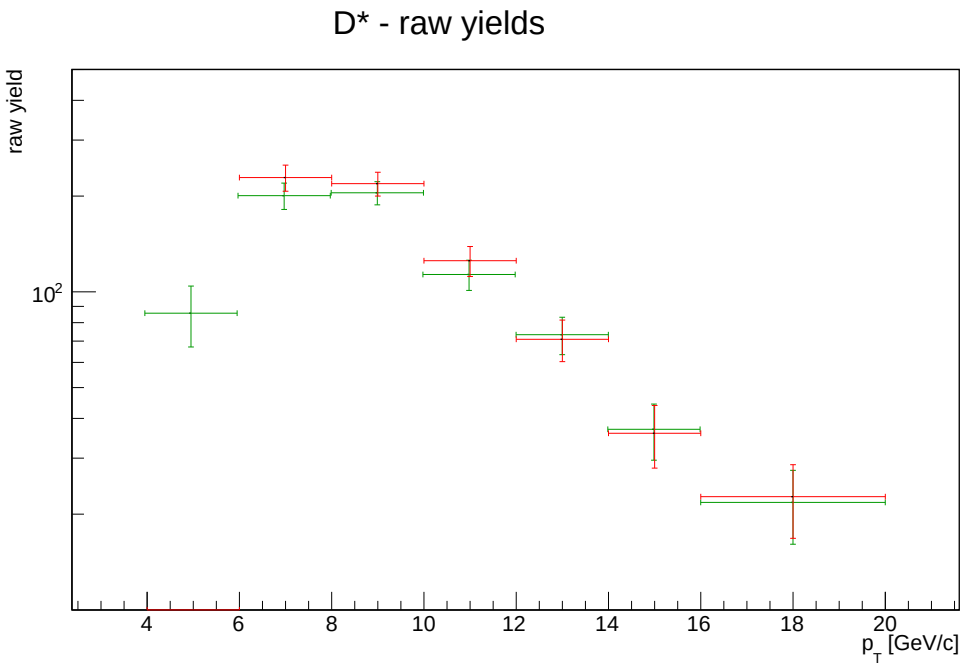

Figure 5.22: Raw yield of D* in the function of p_T for the hadron-triggered events in the p+p collisions at 500 GeV/c.

The obtained result required a correction on various effects related to the registration of the experimental data. The considered factor were:

- track reconstruction efficiency
- BEMC/ToF matching efficiency
- high tower trigger bias

Each of those condition was applied to the daughter particles (pions and kaons) spectra, which then where used to obtain the correction factor for D* distribution.

The track reconstruction efficiency combines both TPC tracking resolution effect and the accuracy with which the reconstruction software can reproduce the trajectories of charged particles emitted in the collision. It was estimated by embedding the simulated tracks into the real events and processing the through the standard reconstruction procedure. The final value was defined as a ratio between the quantity of the reconstructed MC tracks over the number of all embedded particles, the result in a function of p_T is presented on fig. 5.23.

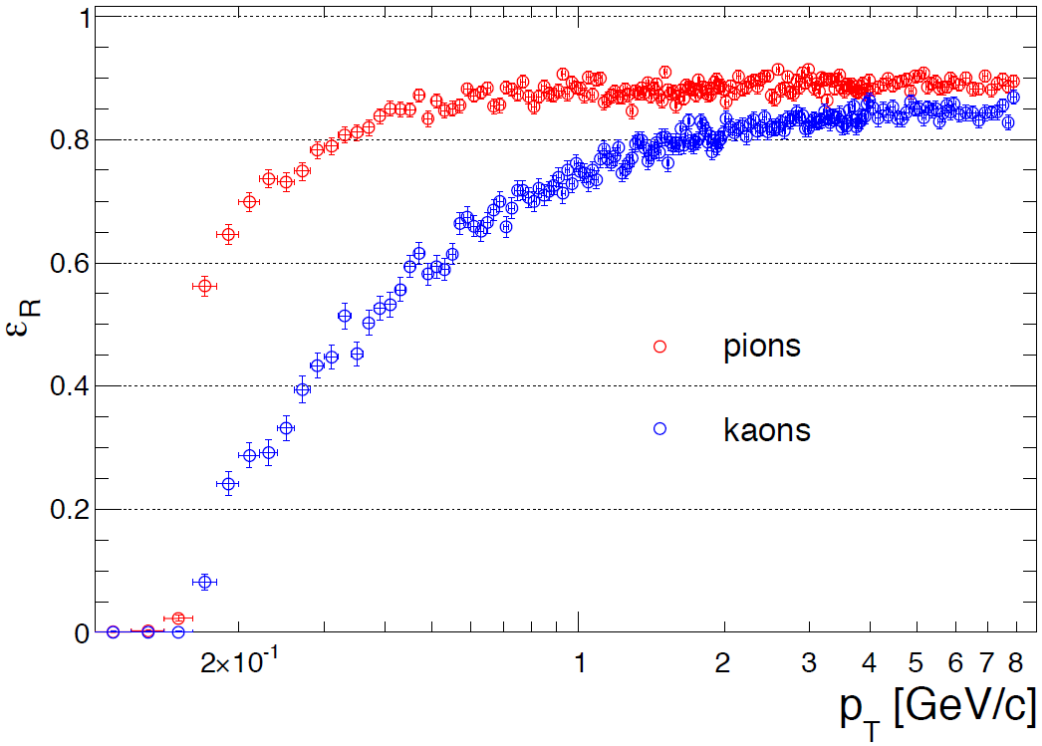

Figure 5.23: The efficiency of pion an kaon reconstruction in the TPC calculated for the p+p collisions at 500 GeV.

As each track was required to have a corresponding information from any of the fast detectors (BEMC or ToF),the efficiency of those had to be taken in account as well. To measure them the assumption was made that the probabilities of having a proper matching to BEMC and ToF are independent values. In such situation the efficiency of BEMC could be described as a ratio between number of tracks with a signal in both detectors over the number of tracks with only to ToF information. The final distribution were calculated as described in the equation 5.1 and 5.2.

$$\varepsilon_{BEMC}(\pi/K) = \frac{|\sigma_{ToF}(\pi/K)| < 2.0 \wedge ToF \wedge BEMC}{|\sigma_{ToF}(\pi/K)| < 2.0 \wedge ToF} \tag{5.1}$$

$$\varepsilon_{ToF}(\pi/K) = \frac{|\sigma_{ToF}(\pi/K)| < 2.0 \wedge ToF \wedge BEMC}{|\sigma_{ToF}(\pi/K)| < 2.0 \wedge BEMC} \tag{5.2}$$

The spectra corrected for both reconstruction efficiency and matching efficiency were then used to estimate the trigger bias. This was done by calculating the ration between the spectra for minimum bias events with those for high tower trigger dataset. As the minimum bias data were not available in the statistics sufficient for performing the measurement in the high p_T region a Pythia simulation fitted to the data was used instead. The comparison of the spectra in different datasets is presented in the fig. 5.24.

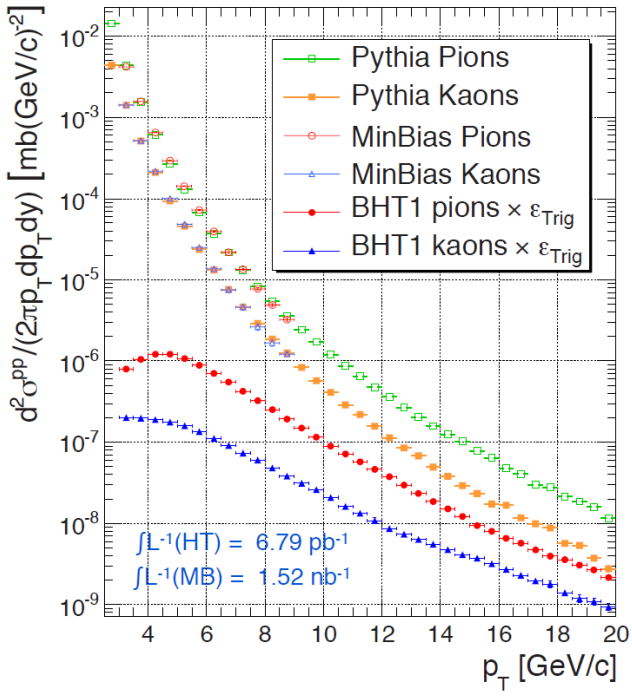

Figure 5.24: The spectra of pions and kaons for minimum bias and high tower datasets of p+p collisions at 500 GeV.

The trigger bias factor for kaons and pions were then averaged and applied to the distribution of D*. The obtained result was aligned with the D* measurement from minimum bias dataset and FONLL (Fixed Order Next To Leading Logarithm) calculations. As shown in the fig. 5.25 it agrees with both of them, which indicates that the trigger bias was estimated properly.

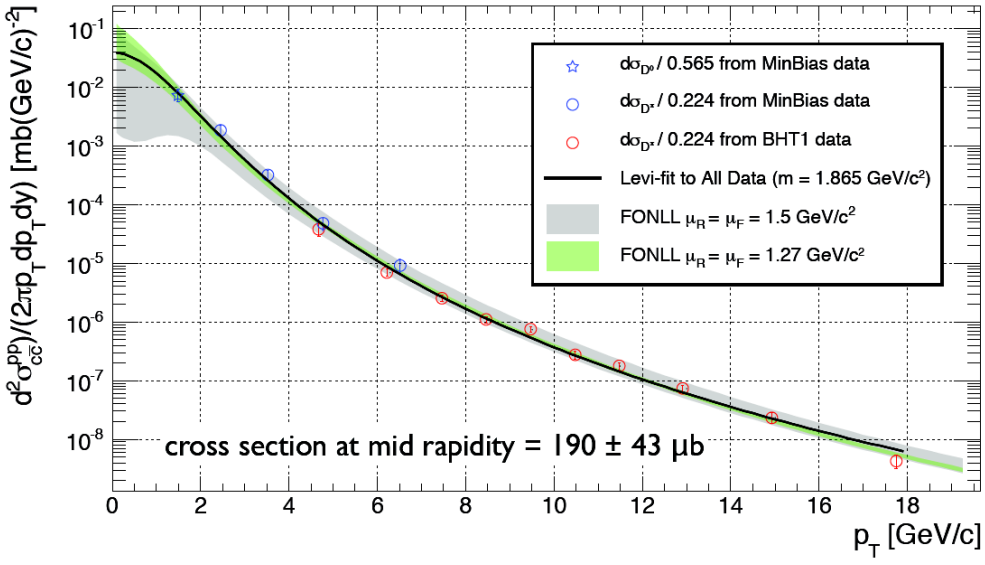

Figure 5.25: The spectrum of D* in p+p collisions at 500 GeV obtained from the high tower dataset (blue circles) in comparison with the D* spectrum from minimum bias events (red circles) together with FONLL predictions.

5.2.3 Charm production in electron-triggered events

The same analysis was repeated for the events triggered by electron (fig. 5.26). However, as the statistics were much more limited this time it was not possible to study the charm production above $p_T > 6GeV/c$ (fig. 5.27). This result it doesn't allow to increase the p_T spectrum available in minimum bias analysis of p+p 500 GeV/c [Ada12].

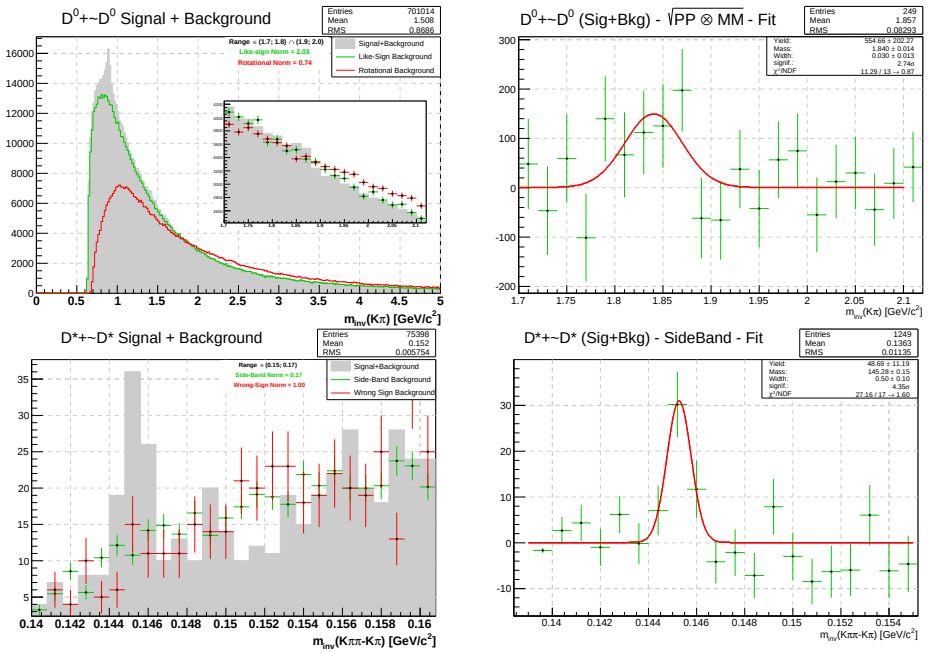

Figure 5.26: D^0 (top) and D^* (bottom) signal in the electron triggered high-tower events. Analysis was done with the cut $cos(\theta^*_K) < 0.6$.

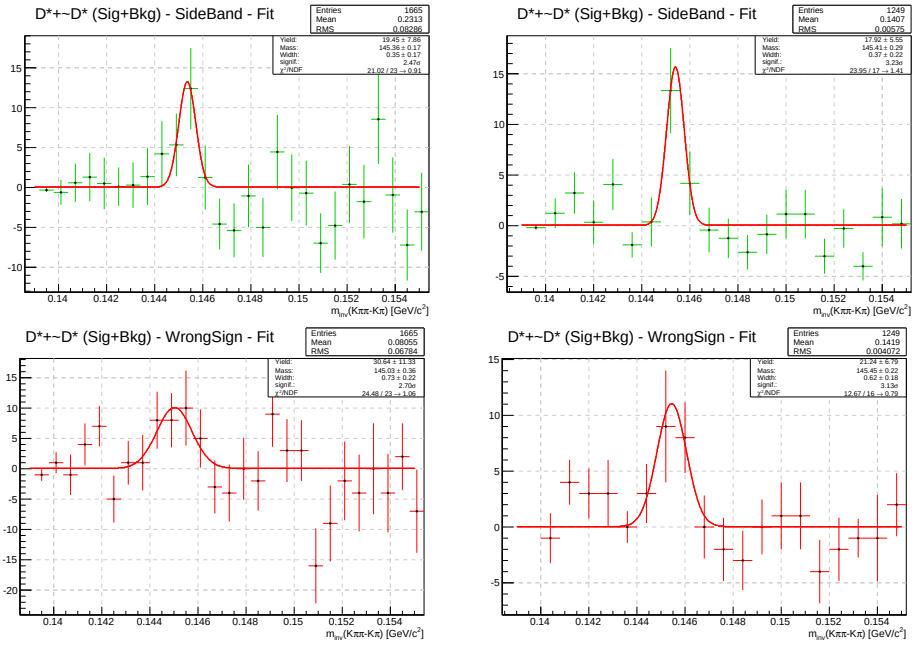

Figure 5.27: D^* signal for $p_T \in (0;4) GeV/c$ (left) and $p_T \in (4;6) GeV/c$ (right) for the side-band (top) and wrong-sign (bottom) background. Analysis was done with the cut $cos(\theta^*_K) < 0.6$.

5.2.4 Electron-D azimuthal angular correlations

The dataset with electron triggered events was finally used to study the e-D azimuthal angular correlations. As the D^0 signal was weak in this dataset only D^* was used for the analysis. As can be seen on the fig. 5.28 the majority of the charm mesons, with the significance of 3.99σ appeared in the near-side like-sign case. At the same time the signal measured in the away-side provides a result with the significance of 2.92σ. The yields obtained from those two cases were then used to estimate the bottom to charm production ratio (b/c+b).

The b/c+b value was calculated as the ratio of the like-sign correlation cases, near-side (top-left on the fig. 5.28) to the away-side (top-right on the fig. 5.28). Based on the Pythia simulations for p+p at 200 GeV it has been estimated that the near-side corresponds mainly to the bottom while the away-side to the charm production (75%) with a smaller contribution of bottom (25%) [Agg10b]. Therefore the bottom contribution was determined by dividing the near-side yield of the D* by the sum of the near-side and 75% of the away-side yield. This has given the result of $\frac{\mathrm{b}}{\mathrm{c+b}} = 0.68 \pm 0.22$, which was then used to compare with the measurements from the $\mathrm{e} - \mathrm{D}^0$ in p+p 200 GeV as well as with the electron-hadron (e-h) correlations in both p+p 200 GeV and 500 GeV systems. For that study the mean $\mathrm{p_T}$ of the non-photonic electrons of the value $\mathrm{p_T} = 5.374\mathrm{GeV/c}$ was used. The comparison of those four measurement is presented on the fig. 5.29.

The $\mathrm{e} - \mathrm{D}^0$ measurement of b/c+b for p+p 200 GeV published in [Agg10b] was in agreement with the results from the electron-hadron (e-h) correlation method. That $\mathrm{e} - \mathrm{D}^0$ point was important as it confirmed the latter results from the e-h correlations. The p+p 500 GeV result within the errors still agrees with the results for the collisions at 200 GeV. Furthermore it extends to the lower $\mathrm{p_T}$ the results from e-h correlations, which are currently available for the $\mathrm{p_T} > 7\mathrm{GeV/c}$.

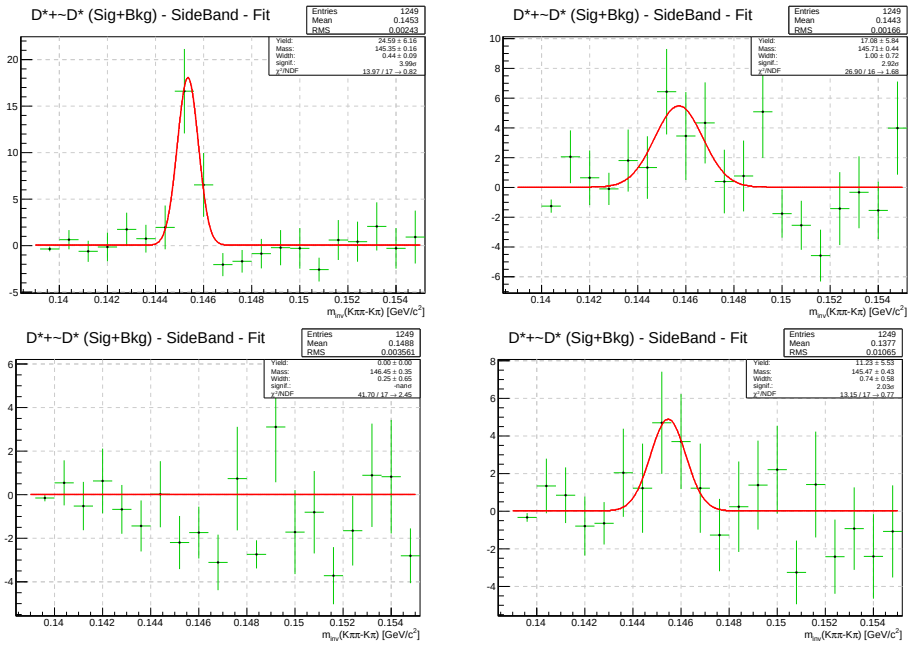

Figure 5.28: D^* signal for the side-band background in different e-D correlation cases: near-side on the left, away side on the right, like-sign on the top, opposite-sign at the bottom. Analysis was done with the cut $cos(\theta^*_K) < 0.6$.

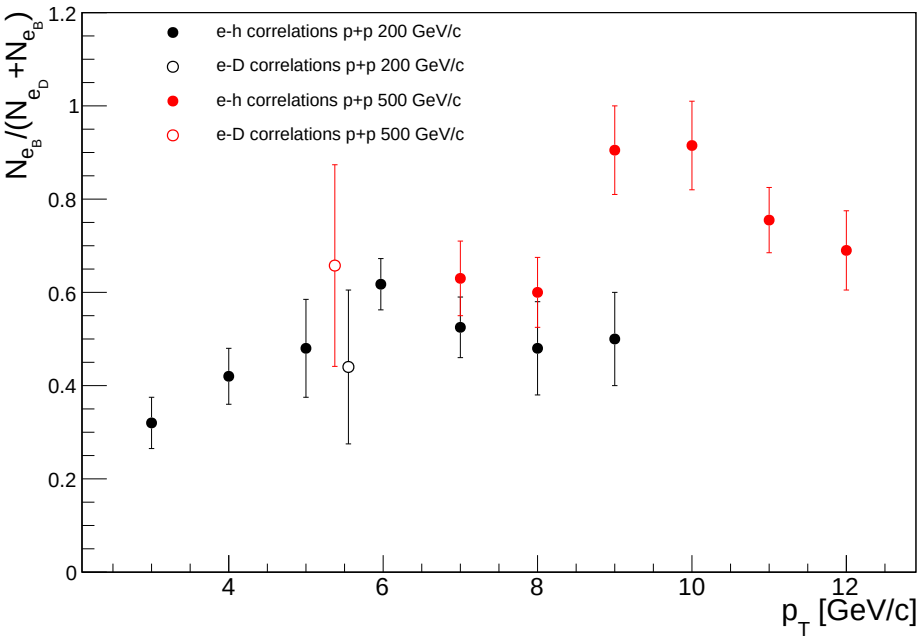

Figure 5.29: A comparison of electron-hadron and electron-D correlations from p+p collisions a 200 GeV and 500 GeV. The results fro 200 GeV system were taken from [Agg10b] while the electron-hadron correlations for 500 GeV are the preliminary results presented [Li12].

Chapter 6

Summary

The measurement of the nuclear modification factor of non-photonic electrons that originate from heavy quarks decays has shown that it exhibits a suppression for the large values of transverse momentum, which is similar to the one measured for the light flavor hadrons. This contradicts the theoretical prediction, thus in this study an attempt was made to separate the beauty and charm contributions in the non-photonic electron spectrum, by measuring the charm meson production in the function of azimuthal angular correlations between the D^0 or D^* and the electron that presumably comes form the heavy flavor semileptonic decay.

The results shows that the capabilities of the current setup of the STAR detector do not allow to perform this kind of measurement in the Gold-Gold collisions at 200 GeV, as the system does not provide the resolution necessary to separate the charm decays from the combinatorial background. Starting form 2014 STAR will be equipped with a new vertex detector, Heavy Flavor Tracker, which is designed to improve the resolution to 30 μm which will allow to identify the origin of non-photonic electrons as well as reconstruct the heavy flavor meson decay vertices.

The outcome from the $e - D^*$ angular correlations in p+p collisions at 500 GeV has allowed to estimate, for the first time with this method, the contribution of beauty to the total open heavy flavor production in this system. The obtained value is within the errors in agreement with the beauty to open heavy flavor ratio measured for the p+p collisions at 200 GeV. Furthermore it extends the measurement of beauty to open heavy flavor from the electron-hadron correlations to the lower p_T.

The inclusive spectra of the charm particles (D0 and D*) has been measured by STAR in proton-proton minimum bias collisions in the range of $p_T \leq 7$GeV/c. The new study of D* performed on the high tower dataset allowed to extend the spectra up to $p_T = 18$ GeV/c for the proton-proton system at 500 GeV. That range of the pT has never been reached before for D* meson analysis on any system measured in STAR.

Bibliography

[Abe07] B.I. Abelev *et al.* *Erratum: Transverse momentum and centrality dependence of high-p_T non-photonic electron suppression in Au+Au collisions at $\sqrt{s_{NN}} = 200\ GeV$.* Phys.Rev.Lett., vol. 98, page 192301, 2007. (Cited on page 10.)

[Ada03] J. Adams *et al.* *Evidence from d + Au measurements for final state suppression of high p(T) hadrons in Au+Au collisions at RHIC.* Phys.Rev.Lett., vol. 91, page 072304, 2003. (Cited on pages 9 and 10.)

[Ada05] John Adams *et al.* *Experimental and theoretical challenges in the search for the quark gluon plasma: The STAR Collaboration's critical assessment of the evidence from RHIC collisions.* Nucl.Phys., vol. A757, pages 102–183, 2005. (Cited on page 9.)

[Ada11] A. Adare *et al.* *Heavy Quark Production in $p+p$ and Energy Loss and Flow of Heavy Quarks in Au+Au Collisions at $\sqrt{s_{NN}} = 200\ GeV$.* Phys.Rev., vol. C84, page 044905, 2011. (Cited on pages 10, 11 and 12.)

[Ada12] L. Adamczyk *et al.* *Measurements of D^0 and D^* Production in $p + p$ Collisions at $\sqrt{s} = 200\ GeV$.* Phys.Rev., vol. D86, page 072013, 2012. (Cited on page 68.)

[Ada13a] L. Adamczyk *et al.* *Single Spin Asymmetry A_N in Polarized Proton-Proton Elastic Scattering at $\sqrt{s} = 200\ GeV$.* Phys.Lett., vol. B719, pages 62–69, 2013. (Cited on page 2.)

[Ada13b] A. Adare *et al.* *Inclusive cross section and single-transverse-spin asymmetry for very forward neutron production in polarized $p + p$ collisions at $\sqrt{s} = 200\ GeV$.* Phys.Rev., vol. D88, page 032006, 2013. (Cited on page 2.)

[Adc05] K. Adcox, S.S. Adler, S. Afanasiev, C. Aidala, N.N. Ajitanand, Y. Akiba, A. Al-Jamel, J. Alexander, R. Amirikas, K. Aoki, L. Aphecetche, Y. Arai, R. Armendariz, S.H. Aronson, R. Averbeck, T.C. Awes, R. Azmoun, V. Babintsev, A. Baldisseri, K.N. Barish, P.D. Barnes, J. Barrette, B. Bassalleck, S. Bathe, S. Batsouli, V. Baublis, F. Bauer, A. Bazilevsky, S. Belikov, F.G. Bellaiche, S.T. Belyaev, M.J. Bennett, Y. Berdnikov, S. Bhagavatula, M.T. Bjorndal, J.G. Boissevain, H. Borel, S. Borenstein, S. Botelho, M.L. Brooks, D.S. Brown, N. Bruner, D. Bucher, H. Buesching, V. Bumazhnov, G. Bunce, J.M. Burward-Hoy, S. Butsyk, X. Camard, T.A. Carey, J.-S. Chai, P. Chand, J. Chang, W.C. Chang, L.L. Chavez, S. Chernichenko, C.Y. Chi, J. Chiba, M. Chiu, I.J. Choi, J. Choi, R.K. Choudhury, T. Christ, T. Chujo, M.S. Chung, P. Chung, V. Cianciolo, C.R. Cleven, Y. Cobigo,

B.A. Cole, M.P. Comets, P. Constantin, M. Csanád, T. Csörgő, J.P. Cussonneau, D. d'Enterria, T. Dahms, K. Das, G. David, F. Deák, H. Delagrange, A. Denisov, A. Deshpande, E.J. Desmond, A. Devismes, O. Dietzsch, B.V. Dinesh, J.L. Drachenberg, O. Drapier, A. Drees, A.K. Dubey, R. du Rietz, A. Durum, D. Dutta, V. Dzhordzhadze, K. Ebisu, Y.V. Efremenko, J. Egdemir, K. El Chenawi, A. Enokizono, H. En'yo, B. Espagnon, S. Esumi, L. Ewell, T. Ferdousi, D.E. Fields, C. Finck, F. Fleuret, S.L. Fokin, B. Forestier, B.D. Fox, Z. Fraenkel, J.E. Frantz, A. Franz, A.D. Frawley, Y. Fukao, S.-Y. Fung, S. Gadrat, S. Garpman, F. Gastineau, M. Germain, T.K. Ghosh, A. Glenn, A.L. Godoi, G. Gogiberidze, M. Gonin, J. Gosset, Y. Goto, R. Granier de Cassagnac, N. Grau, S.V. Greene, M. Grosse Perdekamp, T. Gunji, S.K. Gupta, W. Guryn, H.-Å. Gustafsson, T. Hachiya, A. Hadjhenni, J.S. Haggerty, M.N. Hagiwara, H. Hamagaki, A.G. Hansen, H. Hara, H. Harada, E.P. Hartouni, K. Haruna, M. Harvey, E. Haslum, K. Hasuko, R. Hayano, N. Hayashi, X. He, M. Heffner, T.K. Hemmick, J.M. Heuser, M. Hibino, P. Hidas, H. Hiejima, J.C. Hill, D.S. Ho, R. Hobbs, M. Holmes, W. Holzmann, K. Homma, B. Hong, A. Hoover, T. Horaguchi, H.M. Hur, T. Ichihara, V.V. Ikonnikov, K. Imai, M. Inaba, M. Inuzuka, M.S. Ippolitov, D. Isenhower, L. Isenhower, M. Ishihara, T. Isobe, M. Issah, A. Isupov, B.V. Jacak, W.Y. Jang, Y. Jeong, J. Jia, J. Jin, O. Jinnouchi, B.M. Johnson, S.C. Johnson, K.S. Joo, D. Jouan, F. Kajihara, S. Kametani, N. Kamihara, M. Kaneta, J.H. Kang, M. Kann, S.S. Kapoor, K. Katou, T. Kawabata, T. Kawagishi, A.V. Kazantsev, S. Kelly, B. Khachaturov, A. Khanzadeev, J. Kikuchi, D.H. Kim, D.J. Kim, D.W. Kim, E. Kim, G.-B. Kim, H.J. Kim, S.Y. Kim, Y.-S. Kim, Y.G. Kim, E. Kinney, W.W. Kinnison, A. Kiss, E. Kistenev, A. Kiyomichi, K. Kiyoyama, C. Klein-Boesing, S. Klinksiek, H. Kobayashi, L. Kochenda, V. Kochetkov, D. Koehler, T. Kohama, R. Kohara, B. Komkov, M. Konno, M. Kopytine, D. Kotchetkov, A. Kozlov, P.J. Kroon, C.H. Kuberg, G.J. Kunde, N. Kurihara, K. Kurita, Y. Kuroki, M.J. Kweon, Y. Kwon, G.S. Kyle, R. Lacey, V. Ladygin, J.G. Lajoie, J. Lauret, Y. Le Bornec, A. Lebedev, S. Leckey, D.M. Lee, M.K. Lee, S. Lee, M.J. Leitch, M.A.L. Leite, X.H. Li, Z. Li, D.J. Lim, H. Lim, A. Litvinenko, M.X. Liu, X. Liu, Y. Liu, Z. Liu, C.F. Maguire, J. Mahon, Y.I. Makdisi, A. Malakhov, M.D. Malik, V.I. Manko, Y. Mao, S.K. Mark, S. Markacs, G. Martinez, M.D. Marx, A. Masaike, H. Masui, F. Matathias, T. Matsumoto, M.C. McCain, P.L. McGaughey, E. Melnikov, M. Merschmeyer, F. Messer, M. Messer, Y. Miake, J. Milan, T.E. Miller, A. Milov, S. Mioduszewski, R.E. Mischke, G.C. Mishra, J.T. Mitchell, A.K. Mohanty, D.P. Morrison, J.M. Moss, T.V. Moukhanova, F. Mühlbacher, D. Mukhopadhyay, M. Muniruzzaman, J. Murata, S. Nagamiya, Y. Nagasaka, Y. Nagata, J.L. Nagle, M. Naglis, Y. Nakada, T. Nakamura, B.K. Nandi, M. Nara, J. Newby, M. Nguyen, L. Nikkinen, P. Nilsson, S. Nishimura, B. Norman, A.S. Nyanin, J. Nystrand, E. O'Brien, C.A. Ogilvie, H. Ohnishi, I.D. Ojha, H. Okada, K. Okada, O.O. Omiwade, M. Ono, V. Onuchin, A. Oskarsson,

L. Österman, I. Otterlund, K. Oyama, K. Ozawa, L. Paffrath, D. Pal, A.P.T. Palounek, V. Pantuev, V. Papavassiliou, J. Park, W.J. Park, A. Parmar, S.F. Pate, H. Pei, T. Peitzmann, V. Penev, J.-C. Peng, H. Pereira, V. Peresedov, D.Yu. Peressounko, A.N. Petridis, A. Pierson, C. Pinkenburg, R.P. Pisani, P. Pitukhin, F. Plasil, M. Pollack, K. Pope, M.L. Purschke, A.K. Purwar, H. Qu, J.M. Qualls, J. Rak, I. Ravinovich, K.F. Read, M. Reuter, K. Reygers, V. Riabov, Y. Riabov, G. Roche, A. Romana, M. Rosati, A.A. Rose, S.S.E. Rosendahl, P. Rosnet, P. Rukoyatkin, V.L. Rykov, S.S. Ryu, M.E. Sadler, B. Sahlmueller, N. Saito, A. Sakaguchi, T. Sakaguchi, M. Sakai, S. Sakai, H. Sako, T. Sakuma, V. Samsonov, L. Sanfratello, T.C. Sangster, R. Santo, H.D. Sato, S. Sato, S. Sawada, B.R. Schlei, Y. Schutz, V. Semenov, R. Seto, D. Sharma, M.R. Shaw, T.K. Shea, I. Shein, T.-A. Shibata, K. Shigaki, T. Shiina, M. Shimomura, Y.H. Shin, T. Shohjoh, K. Shoji, I.G. Sibiriak, A. Sickles, C.L. Silva, D. Silvermyr, K.S. Sim, J. Si. *Formation of dense partonic matter in relativistic nucleus–nucleus collisions at RHIC: Experimental evaluation by the {PHENIX} Collaboration.* Nuclear Physics A, vol. 757, no. 1–2, pages 184 – 283, 2005. <ce:title>First Three Years of Operation of RHIC</ce:title>. (Cited on page 9.)

[Adi07] Azfar Adil and Ivan Vitev. *Collisional dissociation of heavy mesons in dense {QCD} matter.* Physics Letters B, vol. 649, no. 2–3, pages 139 – 146, 2007. (Cited on page 11.)

[Ady13] T. Adye. Measurements of higgs boson properties in atlas. Rencontres de Moriond, 2013. (Cited on page 2.)

[Agg10a] M.M. Aggarwal *et al.* *Measurement of the Bottom contribution to non-photonic electron production in $p + p$ collisions at $\sqrt{s}$=200 GeV.* Phys.Rev.Lett., vol. 105, page 202301, 2010. (Cited on pages 11, 14 and 16.)

[Agg10b] M.M. Aggarwal *et al.* *Measurement of the Bottom contribution to non-photonic electron production in $p + p$ collisions at $\sqrt{s}$=200 GeV.* Phys.Rev.Lett., vol. 105, page 202301, 2010. (Cited on pages 70 and 72.)

[Alf08] Mark G. Alford, Andreas Schmitt, Krishna Rajagopal and Thomas Schäfer. *Color superconductivity in dense quark matter.* Rev.Mod.Phys., vol. 80, pages 1455–1515, 2008. (Cited on page 4.)

[All02] J. Allday. Quarks, leptons and the big bang. Institute of Physics Publishing, second edition édition, 2002. (Cited on page 6.)

[And03] M. Anderson, J. Berkovitz, W. Betts, R. Bossingham, F. Bieser *et al.* *The Star time projection chamber: A Unique tool for studying high multiplicity events at RHIC.* Nucl.Instrum.Meth., vol. A499, pages 659–678, 2003. (Cited on page 19.)

[Arm06] Nestor Armesto, Matteo Cacciari, Andrea Dainese, Carlos A. Salgado and Urs Achim Wiedemann. *How sensitive are high-p(T) electron spectra at RHIC to heavy quark energy loss?* Phys.Lett., vol. B637, pages 362–366, 2006. (Cited on page 10.)

[Ars05] I. Arsene, I.G. Bearden, D. Beavis, C. Besliu, B. Budick, H. Bøggild, C. Chasman, C.H. Christensen, P. Christiansen, J. Cibor, R. Debbe, E. Enger, J.J. Gaardhøje, M. Germinario, O. Hansen, A. Holm, A.K. Holme, K. Hagel, H. Ito, E. Jakobsen, A. Jipa, F. Jundt, J.I. Jørdre, C.E. Jørgensen, R. Karabowicz, E.J. Kim, T. Kozik, T.M. Larsen, J.H. Lee, Y.K. Lee, S. Lindahl, G. Løvhøiden, Z. Majka, A. Makeev, M. Mikelsen, M.J. Murray, J. Natowitz, B. Neumann, B.S. Nielsen, D. Ouerdane, R. Płaneta, F. Rami, C. Ristea, O. Ristea, D. Röhrich, B.H. Samset, D. Sandberg, S.J. Sanders, R.A. Scheetz, P. Staszel, T.S. Tveter, F. Videbæk, R. Wada, Z. Yin and I.S. Zgura. *Quark–gluon plasma and color glass condensate at RHIC? The perspective from the {BRAHMS} experiment.* Nuclear Physics A, vol. 757, no. 1–2, pages 1 – 27, 2005. <ce:title>First Three Years of Operation of RHIC</ce:title>. (Cited on page 9.)

[Bac05] B.B. Back, M.D. Baker, M. Ballintijn, D.S. Barton, B. Becker, R.R. Betts, A.A. Bickley, R. Bindel, A. Budzanowski, W. Busza, A. Carroll, Z. Chai, M.P. Decowski, E. García, T. Gburek, N.K. George, K. Gulbrandsen, S. Gushue, C. Halliwell, J. Hamblen, A.S. Harrington, M. Hauer, G.A. Heintzelman, C. Henderson, D.J. Hofman, R.S. Hollis, R. Hołyński, B. Holzman, A. Iordanova, E. Johnson, J.L. Kane, J. Katzy, N. Khan, W. Kucewicz, P. Kulinich, C.M. Kuo, J.W. Lee, W.T. Lin, S. Manly, D. McLeod, A.C. Mignerey, R. Nouicer, A. Olszewski, R. Pak, I.C. Park, H. Pernegger, C. Reed, L.P. Remsberg, M. Reuter, C. Roland, G. Roland, L. Rosenberg, J. Sagerer, P. Sarin, P. Sawicki, H. Seals, I. Sedykh, W. Skulski, C.E. Smith, M.A. Stankiewicz, P. Steinberg, G.S.F. Stephans, A. Sukhanov, J.-L. Tang, M.B. Tonjes, A. Trzupek, C.M. Vale, G.J. van Nieuwenhuizen, S.S. Vaurynovich, R. Verdier, G.I. Veres, E. Wenger, F.L.H. Wolfs, B. Wosiek, K. Woźniak, A.H. Wuosmaa, B. Wysłouch and J. Zhang. *The {PHOBOS} perspective on discoveries at {RHIC}.* Nuclear Physics A, vol. 757, no. 1–2, pages 28 – 101, 2005. <ce:title>First Three Years of Operation of RHIC</ce:title>. (Cited on page 9.)

[Bai97] R. Baier, Yuri L. Dokshitzer, Alfred H. Mueller, S. Peigne and D. Schiff. *Radiative energy loss of high-energy quarks and gluons in a finite volume quark - gluon plasma.* Nucl.Phys., vol. B483, pages 291–320, 1997. (Cited on page 9.)

[Bed03] M. Beddo *et al.* *The STAR barrel electromagnetic calorimeter.* Nucl.Instrum.Meth., vol. A499, pages 725–739, 2003. (Cited on page 20.)

[Ber12] J. Beringer *et al. Review of Particle Physics.* Phys. Rev. D, vol. 86, page 010001, Jul 2012. (Cited on page 26.)

[bnl] *Homepage of Brookhaven National Laboratory.* (Cited on page 17.)

[Bon03] B Bonner, H Chen, G Eppley, F Geurts, J Lamas-Valverde, Ch Li, W.J Llope, T Nussbaum, E Platner and J Roberts. *A single Time-of-Flight tray based on multigap resistive plate chambers for the {STAR} experiment at {RHIC}.* Nuclear Instruments and Methods in Physics Research Section A: Accelerators, Spectrometers, Detectors and Associated Equipment, vol. 508, no. 1–2, pages 181 – 184, 2003. <ce:title>Proceedings of the Sixth International Workshop on Resistive Plate Chambers and Related Detectors</ce:title>. (Cited on page 19.)

[Clo83] F.E. Close. The Cosmic Onion: Quarks and the Nature of the Universe. Heinemann Educational, 1983. (Cited on pages 1 and 6.)

[Col75] J.C. Collins and M. J. Perry. *Superdense Matter: Nuetrons or Asymptotically Free Quarks?* Phys. Rev. Lett., vol. 34, page 1353, 1975. (Cited on page 4.)

[Cro75] J. W. Cronin, H. J. Frisch, M. J. Shochet, J. P. Boymond, P. A. Piroué and R. L. Sumner. *Production of hadrons at large transverse momentum at 200, 300, and 400 GeV.* Phys. Rev. D, vol. 11, pages 3105–3123, Jun 1975. (Cited on page 9.)

[Dok01] Yuri L. Dokshitzer and D.E. Kharzeev. *Heavy quark colorimetry of QCD matter.* Phys.Lett., vol. B519, pages 199–206, 2001. (Cited on page 10.)

[Don06] W. Dong. *Measurement of non-photonic electron azimuthal anisotropy v2 from Au+Au collisions at* $\sqrt{s_{NN}} = 200GeV$. PhD thesis, University of California, 2006. (Cited on page 42.)

[fer] *Homepage of Fermilab.* http://www.fnal.gov. (Cited on page 3.)

[Gos08] P. B. Gossiaux and J. Aichelin. *Toward an understanding of the single electron data measured at the BNL Relativistic Heavy Ion Collider (RHIC).* Phys. Rev. C, vol. 78, page 014904, Jul 2008. (Cited on page 11.)

[Gos09a] P.B. Gossiaux and J. Aichelin. *Tomography of the Quark Gluon Plasma by Heavy Quarks.* J.Phys., vol. G36, page 064028, 2009. (Cited on page 11.)

[Gos09b] P.B. Gossiaux, R. Bierkandt and J. Aichelin. *Tomography of a quark gluon plasma at RHIC and LHC energies.* Phys.Rev., vol. C79, page 044906, 2009. (Cited on page 11.)

[gsi] *Homepage of GSI Helmholtzzentrum für Schwerionenforschung GmbH.* http://www.gsi.de. (Cited on page 5.)

[Hal08] F. Halzen and A.D. Martin. Quark & leptons: An introductory course in modern particle physics. Wiley India Pvt. Limited, 2008. (Cited on page 1.)

[Hwa04] Rudolph C. Hwa and C. B. Yang. *Final-State Interaction as the Origin of the Cronin Effect.* Phys. Rev. Lett., vol. 93, page 082302, Aug 2004. (Cited on page 9.)

[lbl] *Homepage of Lawrence Berkeley National Labolatory.* http://www.lbl.gov. (Cited on page 8.)

[Li12] Wei Li. *Non-photonic electron and charged hadron azimuthal correlation in p + p collisions at s**(1/2) = 500-GeV in STAR.* Acta Phys.Polon.Supp., vol. 5, pages 413–418, 2012. (Cited on page 72.)

[Luo12] Xiao-Feng Luo, Bedangadas Mohanty, Hans Georg Ritter and Nu Xu. *Search for the QCD Critical Point: Higher Moments of Net-proton Multiplicity Distributions.* Phys.Atom.Nucl., vol. 75, page 676, 2012. (Cited on page 5.)

[Mis09] André Mischke. *A new correlation method to identify and separate charm and bottom production processes at {RHIC}.* Physics Letters B, vol. 671, no. 3, pages 361 – 365, 2009. (Cited on page 13.)

[na4] *Homepage of NA49 experiment.* (Cited on page 6.)

[Per00] D.H. Perkins. Introduction to high energy physics. Cambridge University Press, 2000. (Cited on pages 1, 4, 6 and 28.)

[Sak10] S. Sakai, G. Wang, H.Z. Huang and X. Lin. Azimuthal correlation between nonphotonic electrons and hadrons from p+p collisions at $\sqrt{s_{NN}} = 200GeV$. 2010. (Cited on page 42.)

[Sat12] H. Satz. Extreme states of matter in strong interaction physics: An introduction. Lecture Notes in Physics. Springer, 2012. (Cited on page 4.)

[Sjo01] Torbjorn Sjostrand, Patrik Eden, Christer Friberg, Leif Lonnblad, Gabriela Miu *et al. High-energy physics event generation with PYTHIA 6.1.* Comput.Phys.Commun., vol. 135, pages 238–259, 2001. (Cited on page 11.)

[sta] *Homepage of STAR experiment.* (Cited on page 18.)

[Wan95] Xin-Nian Wang, Miklos Gyulassy and Michael Plümer. *Landau-Pomeranchuk-Migdal effect in QCD and radiative energy loss in a quark-gluon plasma.* Phys. Rev. D, vol. 51, pages 3436–3446, Apr 1995. (Cited on page 9.)

[Whi13] A. J. Whitbeck. Measurements of higgs boson properties in cms. Rencontres de Moriond, 2013. (Cited on page 2.)

[Wic07] Simon Wicks, William Horowitz, Magdalena Djordjevic and Miklos Gyulassy. *Elastic, inelastic, and path length fluctuations in jet tomography.* Nucl.Phys., vol. A784, pages 426–442, 2007. (Cited on page 10.)

[Xu09] Y. Xu. *Measurements of high-p_T identified hadron spectra in p+p and Au+Au collisions at RHIC.* PhD thesis, University of Science and Technology of China, Hefei, 2009. (Cited on page 55.)